# Gravitational lensing in a clumpy universe

Doctoral Thesis

Víctor David Boscá Navarro

# Gravitational lensing in a clumpy universe

Memoria de tesis doctoral realizada por
**Víctor David Boscá Navarro**
presentada ante el Departamento de Física Teórica
de la Universidad Autónoma de Madrid
para optar al título de doctor en Física Teórica.

Tesis doctoral dirigida por el Dr. **Pierre Fleury**, Chargé de recherches
en el CNRS - Centre National de la Recherche Scientifique, y
el Dr. **Juan García-Bellido Capdevila**, catedrático de Física Teórica
de la Universidad Autónoma de Madrid.

Departamento de Física Teórica
Universidad Autónoma de Madrid
Instituto de Física Teórica UAM-CSIC




Marzo de 2023

*A mis padres, a mi hermana y a Nacho*

"Young people, especially young women, often ask me for advice. Here it is, valeat quantum. Do not undertake a scientific career in quest of fame or money. There are easier and better ways to reach them. Undertake it only if nothing else will satisfy you; for nothing else is probably what you will receive. Your reward will be the widening of the horizon as you climb. And if you achieve that reward you will ask no other."

---

Cecilia Payne

# AGRADECIMIENTOS

Estos 3 años y medio de doctorado han supuesto, sin ninguna duda, un importante salto de madurez en mi vida. No sé muy bien cuando empezó mi interés por la ciencia y en particular, por la física; supongo que desde que era un niño, cuando jugaba con cajas de cartón imaginando que eran máquinas del tiempo. Sin embargo, la primera idea para estudiar física llegó cuando empecé a ver una serie en la que un tal Sheldon me mostró como acabaría yo si seguía ese camino, o cuando un profesor de matemáticas me contagió su pasión por los números y entonces me dije a mí mismo: "yo tengo que hacer una carrera científica". El conocer el motivo por el que suceden las cosas, pensar que todo tiene una explicación y que además se pueda expresar con un lenguaje objetivo y universal, que son las matemáticas, fue lo que me hizo emprender este camino. Por este motivo quiero empezar agradeciendo a todas las personas que, desde el principio, me influyeron y motivaron para llegar hasta aquí.

Bueno, centrándome en el doctorado, no puedo sino empezar agradeciendo a mis directores de tesis. Pierre, has sido un apoyo constante durante toda esta etapa, incluso en lo personal, donde me has dado valiosos consejos y me has ayudado a tomar decisiones muy importantes. Por el lado científico, me llevo conmigo tu rigor, organización y ética. Juan, al igual que Pierre, he tenido tu apoyo desde el principio, incluso cuando no me conociás y me has ayudado a cumplir uno de los sueños que tenía desde pequeño, vivir en Estados Unidos. De ti me llevo la pasión que tienes por la ciencia —bueno, por todos los campos en realidad— la cual, no ves como un trabajo. Aspiro a mantener esa pasión siempre. Quiero agradecer también a la persona que me acogió en mi estancia en Chicago, Jose María. Gracias por tener siempre la puerta abierta para lo que necesitara y por tu apoyo. Estas 3 personas tienen mi total admiración.

Quiero agradecer también a mis amigos de Gandía, mis amigos de toda la vida, los cuales me han acompañado en todas las etapas. Su lealtad está al nivel de sus rarezas. Gracias también a mis amigos de la universidad Luís, Jorge y Oleg. Cada uno, hijo de su padre y de su madre, pero que comparten esa alegría natural que los hace imprescindibles para mí. Nos vamos para Alemania. Gracias Carlos, mi "hermano mayor" del Erasmus. Me enseñaste a ver la vida de una forma diferente y que las cosas no son ni para tanto ni para siempre. Viajando a Italia, no me puedo olvidar de Gianni,

quien me enseñó a ver la física de otra manera fuera de la academia. Gracias también a mis amigos y amigas de Heidelberg, una de las etapas más felices de mi vida. ¡Gracias Pablo! Gracias por todos esos concursos de tortilla redundante, por esas conversaciones filosóficas y por haber estado ahí siempre en una época de constantes cambios. ¡Pau! Cuando me he reído contigo. Heidelberg no hubiera sido lo mismo, ni de lejos, sin ti. Gracias también a Jose y mis amigos mexicanos. Vuestras historias, imposibles de olvidar, me acompañarán siempre. Y como no, gracias a mis amigos italianos y griegos.

Ya en Madrid, no puedo olvidarme de Joan. Echaré de menos nuestras intensas conversaciones en el despacho. Lo tendríamos que haber compartido más tiempo. Santi, espero que estés disfrutando de Japón. A ver si algún día volvemos a compartir despacho. Gracias también a mis fellows, a la caixa de papel. Guille, Víctor, Marina..., y como no... ¡el gran Arnau Pilots!. Igual ahora me ganas a tenis, que esta tesis me ha dejado en un estado de forma mejorable. Mira que me lo he pasado bien y he reído con vosotros. Gracias a Tobías, mi bonachón amigo argentino y tenista. Espero muchos más partidos contigo. Gracias también a Vicente, vecino y compañero de piso.

Viajando a la otra parte del mundo, quiero dar las gracias a mis amigos murcianos del Pacífico, José Ángel y Rosa. Os cocozco desde hace poco tiempo, pero sois de las personas más buenas con las que me he cruzado. No voy a olvidar nuestros viajes por California y Arizona. Gracias también a la alegría de Silvia cuando llegaba a casa. Cambiando de campo totalmente, no puedo olvidarme de mis amistades más recientes. Gracias a Teresa, Marta, Maitane, Rubén y Susana por hacer que este "año ICEX" sea mucho más llevadero. No puedo imaginarme una mejor compañía en esta transición que la vuestra.

En el plano más personal quiero agradecer infinitamente a Mica, quizás la única persona que me entiende completamente ahora mismo. Dudo mucho que hubiera podido sacar este año tan bien sin tu ayuda. Gracias por soportarme cada día y por haberlo compartido todo conmigo en estos dos años. Tengo muchas ganas del futuro que se nos asoma.

No obstante, no hubiera llegado hasta aquí si no hubiera sido por mis padres, mi hermana y Nacho, a quienes dedico esta tesis. Su apoyo totalmente incondicional y su ayuda a todos los niveles han hecho posible cumplir todo lo que me he propuesto. Cuando uno posee una base familiar tan sólida, todo se hace mucho más fácil. Siempre van a estar ahí.

Finalmente, quiero agradecer a la madre de todas las ciencias, el pilar fundamental de la naturaleza, capaz de explicar desde las interacciones fundamentales de la materia hasta el destino de nuestro universo: la física. La física me ha dado la oportunidad de viajar por el mundo, de conocer a gente increíble de todos los campos, de emocionarme con sus leyes y de asegurarme un futuro ilusionante. Siga el camino que siga, siempre me sentiré orgulloso de ser físico y de formar parte de esta gran familia de científicos. Tomo la responsabilidad y el rigor que esto implica y siempre defenderé la pureza de la ciencia.


The author of this thesis received funding from a fellowship from “la Caixa” Foundation (ID 100010434). The fellowship code is LCF/BQ/DI19/11730063.

# PREFACE

In the last century, cosmology has unveiled one of the greatest mysteries of fundamental physics. There exist an hypothetical form of matter that makes up approximately 83% of matter in our universe. It is invisible, i.e., it does not interact with light or other forms of electromagnetic radiation, so it cannot be directly observed. We only know its effect through its gravitational pull. Despite the overwhelming evidence of its existence, the nature of dark matter remains a mystery, and there are various theories about what it could be made of. One of most promising, due to the first detection of a gravitational-wave signal reported by the LIGO/Virgo Collaboration in 2015, got back under spotlight, namely primordial black holes, an old dark matter candidate.

The theoretical understanding of the clumpy structure of the matter distribution in our universe is therefore crucial for cosmology. One of the most efficient ways to learn about it, is by using gravitational lensing, which is the bending of a wave due to the presence of a gravitational field and has the virtue of being directly sensitive to the presence of clumps. The theoretical understanding of gravitational lensing in a clumpy universe is the motivation of this thesis.

This thesis is divided in two parts, where we study the two types of waves than can experience gravitational lensing, electromagnetic and gravitational waves. In Part I, we study the propagation of light in a universe filled with compact objects and improve the previous analysis about the amplification probabilities. In Part II, we perform a similar analysis with gravitational waves and make a forecast of the rate of lensed events in current and future detectors.

Light consists of electromagnetic waves, which are oscillations of electric and magnetic fields. Electromagnetic radiation is emitted by accelerated and electrically charged particles. On the other hand, gravitational waves describe the propagation of the spacetime as waves of energy. Both waves follow null geodesics and one propagates at the speed of the other. This implies that the theory of light can also be applied to gravitational waves. However, they present some differences. Gravitational waves do not follow a dipole radiation pattern like light but a quadrupole. Gravity is a weak force with only one sign of charge while electromagnetism is much stronger and with two opposing signs of charge. As a result, gravitational waves are extraordinarily

difficult to detect. On the other hand, while electromagnetic waves can be easily detected due to their strong interaction with normal matter, they can be absorbed or scattered by intervening matter. Gravitational waves however, can travel unobstructed through matter of any density or composition, making them a unique tool for observing objects and events in the universe.

Despite their numerous differences, we show in this thesis that they are both powerful probes to study and constrain the clumpiness of our universe.

# PREFACIO

En el último siglo, la cosmología ha revelado uno de los mayores misterios de la física fundamental. Existe una forma hipotética de materia que constituye aproximadamente el 83% de la materia en nuestro universo. Es invisible, es decir, no interactúa con la luz ni con otras formas de radiación electromagnética, por lo que no puede ser observada directamente. Solo conocemos su efecto a través de su atracción gravitacional. A pesar de la abrumadora evidencia de su existencia, la naturaleza de la materia oscura sigue siendo un misterio, y existen diversas teorías sobre de qué podría estar hecha. Una de las más prometedoras, debido a la primera detección de ondas gravitacionales por la colaboración LIGO/Virgo en 2015, volvió a estar en primer plano, los agujeros negros primordiales, un antiguo candidato a materia oscura.

La comprensión teórica de la estructura grumosa de la distribución de materia en nuestro universo es, por lo tanto, crucial para la cosmología. Una de las formas más eficientes de estudiarla es mediante lentes gravitacionales, las cuales desvían la trayectoria de una onda debido a la presencia de un campo gravitacional y tiene la virtud de ser directamente dependiente de la presencia de cúmulos de masa. La comprensión teórica de la lente gravitacional en un universo grumoso es la motivación de esta tesis.

Esta tesis se divide en dos partes, donde estudiamos los dos tipos de ondas que pueden experimentar un desvío en su trayectoria debido a las lentes gravitacionales, las ondas electromagnéticas y las ondas gravitacionales. En la Parte I, estudiamos la propagación de la luz en un universo lleno de objetos compactos y mejoramos el análisis previo sobre las probabilidades de amplificación. En la Parte II, realizamos un análisis similar con las ondas gravitacionales y hacemos una predicción de la tasa de eventos que han experimentado lensing en detectores actuales y futuros.

La luz consiste en ondas electromagnéticas, las cuales son oscilaciones de campos eléctricos y magnéticos. La radiación electromagnética es emitida por partículas cargadas eléctricamente y aceleradas. Por otro lado, las ondas gravitacionales describen la propagación del espacio-tiempo como ondas de energía. Ambas ondas siguen geodésicas nulas y una se propaga a la velocidad de la otra. Esto implica que la teoría de la luz también se puede aplicar a las ondas gravitacionales. Sin embargo, presentan

algunas diferencias. Las ondas gravitacionales no siguen un patrón de radiación dipolo como la luz, sino un cuadrupolo. La gravedad es una fuerza débil con solo un signo de la carga, mientras que la fuerza electromagnética es mucho más fuerte y tiene dos cargas opuestas. Como resultado, las ondas gravitacionales son extraordinariamente difíciles de detectar. Por otro lado, mientras que las ondas electromagnéticas se pueden detectar fácilmente debido a su fuerte interacción con la materia normal, pueden ser también absorbidas o dispersadas por ésta. Las ondas gravitacionales, sin embargo, pueden viajar sin obstáculos a través de materia de cualquier densidad y composición, lo que las convierte en una herramienta única para observar objetos y eventos en el universo.

A pesar de sus numerosas diferencias, en esta tesis mostramos que el efecto de lente gravitacional en ambas ondas es una poderosa herramienta para estudiar el universo grumoso.

# CONTENTS


**I Light propagation in a clumpy universe** **5**

**Abstract** **7**

**1 Introduction** **9**
1.1 The theory of light . . . . . 9
1.2 The *Gedankenexperiment* . . . . . 11
1.3 The eclipse . . . . . 12
1.4 The amplification of light . . . . . 14
1.5 The theoretical research and the first observation . . . . . 16
1.6 Microlensing and current status . . . . . 19
1.7 Modelling of the microlensing statistics . . . . . 21

**2 Optical depth and extragalactic microlensing** **23**
2.1 Intuition and definitions . . . . . 23
2.2 Amplification probability at very low optical depth . . . . . 26
2.3 Distribution of optical depth in a realistic universe . . . . . 27
2.4 Relevant optical depths are not that low . . . . . 29

**3 Point lens with environment and line-of-sight perturbations** **33**
3.1 Description of the set-up . . . . . 33
3.2 Lens equation and equivalent lens . . . . . 34
3.2.1 Lens equation with tidal perturbations . . . . . 35
3.2.2 Physical origin of the convergence and shear . . . . . 36
3.2.3 Equivalent lens . . . . . 37
3.3 Amplification cross section . . . . . 38
3.3.1 For the equivalent lens . . . . . 38
3.3.2 Back to the original problem . . . . . 40

**4 Amplification probabilities** **41**
4.1 Amplification probability for a single lens . . . . . 41
4.1.1 Approximations . . . . . 42
4.1.2 Distribution of the microshear . . . . . 43
4.1.3 The macroshear is negligible . . . . . 44

4.1.4 Final expression of $p_1(A)$ . . . 45
4.2 From one lens to many: the strongest-perturbed-lens prescription . . 46
4.3 Marginalising over the line-of-sight convergence . . . 48
4.4 Comparison with Zumalacárregui & Seljak . . . 50

**5 Extended sources** **53**
5.1 Extended-source corrections on an isolated point lens . . . 53
5.2 Amplification cross section of an isolated lens . . . 54
5.3 Amplification probabilities with extended sources . . . 55

**6 Conclusion** **59**

**II Gravitational wave propagation in a clumpy universe 61**

**Abstract** **63**

**7 Introduction** **65**
7.1 A gravitational and electromagnetic analogy . . . 65
7.2 Einstein's approximations . . . 66
7.3 The first detector . . . 67
7.4 The laser interferometers: LIGO and Virgo . . . 70
7.5 GW150914: The first detection . . . 73
7.6 Other gravitational wave observatories . . . 76
7.7 Lensing of gravitational waves . . . 77

**8 Scales of lensing of gravitational waves** **79**
8.1 Diffraction integral and wave optics . . . 81
8.2 Point lens . . . 83
8.3 Singular isothermal sphere . . . 84
8.4 Geometric optics approximation . . . 85
8.5 Strong lensing, microlensing and interference . . . 87

**9 Detecting lensing of gravitational waves** **89**
9.1 Template-based searches . . . 89
9.2 Relevant scales for lensing detection . . . 90
9.3 Relevant scales for wave optics detection . . . 91

**10 The probability of lensing of gravitational waves** **95**
10.1 Microlensing . . . 96
10.2 Strong lensing . . . 97
10.3 Strong lensing with microlensing corrections . . . 98

**11 Forecasts** **103**

**12 Conclusion** **107**

**Appendices**

**A Weak-lensing statistics with RayGalGroupSims** **115**
A.1 Convergence . . . . . 115
A.2 Macroshear . . . . . 117

**B Derivation of the microshear distribution** **119**
B.1 PDF of a sum of complex shears . . . . . 119
B.2 Large-$N$ limit . . . . . 120
B.3 Application to the effective reduced microshear due to point lenses . . 121

**Bibliography** **136**

# Part I

# Light propagation in a clumpy universe

# ABSTRACT

Microlensing of extragalactic sources, in particular the probability of significant amplifications, is a potentially powerful probe of the abundance of compact objects outside the halo of the Milky Way. Accurate experimental constraints require an equally accurate theoretical model for the amplification statistics produced by such a population. In this part, we argue that the simplest (strongest-lens) model does not meet this demanding requirement. We thus propose an elaborate practical modelling scheme for extragalactic microlensing. We derive from first principles an expression for the amplification probability that consistently allows for: (i) the coupling between microlenses; (ii) realistic perturbations from the cosmic large-scale structure; (iii) extended-source corrections. An important conclusion is that the external shear applied on the dominant microlens, both by the other lenses and by the large-scale structure, is practically negligible. Yet, the predictions of our approach can still differ by a factor of a few with respect to existing models of the literature. Updated constraints on the abundance of compact objects accounting for such discrepancies may be required.

CHAPTER

# ONE

# INTRODUCTION

This chapter highlights the major events in the history of light deflection and the previous works that have motivated the first part of this thesis.

## 1.1 The theory of light

The eighteenth century gave rise to an intense debate about the nature of light. The Dutch polymath Christiaan Huygens stated in this book *Traité de la Lumière* that a light source emits a wavefront in all directions in a continuous and homogeneous medium called aether and each point of the wavefront is, at the same time, the source of a secondary spherical wave [1]. This is called the Huygens-Fresnel principle. This theory manages to explain most of the properties of light such as the effect of reflection and refraction. It also explains the phenomenon of wave diffraction around edges. The wave theory of Huygens, however, had to compete with the most influential "natural philosopher" of that time, sir Isaac Newton. In 1704, the English physicist published his work *Opticks* where he formulated the corpuscular theory of light. This theory states that the geometric nature of reflection and refraction of light could only be explained if light were made of small particles named "corpuscles" emitted by a luminous body and propagated through the space along straight lines following the laws of classical mechanics [2]. Consequently, the speed of light changes according on the medium's density through which it travels. Due to the success of the prism experiment and the fact that the wave theory of Huygens was never experimentally corroborated, Newton's theory prevailed until 1802 when Thomas Young, through the famous double-slit experiment, settled the debate in favour of the wave theory [3]. However, the wave theory was reinforced in 1861 by James Clerk Maxwell, who proposed that light is an electromagnetic phenomenon that can propagate through vacuum without the need of a medium [4]. Furthermore, a few years later, Einstein described the photoelectric effect, in which light can actually be treated as a real particle that accounts for a few reasons and unexplained experiments [5]. He called this particle a photon. Finally, in 1924, with the basis of quantum mechanics already set, the wave–particle duality was born [6].

However, the corpuscular theory of light was the inception of a bigger idea. Based on this hypothesis Newton suggested, in a note at the end of his treaty *Opticks*, that, if these particles were massive, they could be affected by gravity and therefore their rectilinear trajectories could be deviated. Newton's idea that light could be affected by gravity drew the attention of a clergyman and natural philosopher named John Michell in 1784. He thought that the speed of light could accelerate when passing near a star like the Sun due to its gravity. By measuring this acceleration, it might be possible to measure the mass of the star itself [7]. Michell explained this idea in a letter sent to the English chemist and physicist Henry Cavendish who, motivated by Michell's suggestion, calculated the deviation that light should suffer in its encounter with the star. Following the laws of classical mechanics and Newton's idea that light behaves like fast moving particles, it would be deviated at a distance $R$ by a star of mass $M$ by an angle

$$\alpha(R) = \frac{2GM}{c^2 R} \tag{1.1}$$

where $G = 6.67428 \times 10^{-11}$ Nm$^{-2}$kg$^{-2}$ is the gravitational constant and $c = 299792$ km s$^{-1}$ is the speed of light. The quantity derived by Cavendish in his notes is called the *deflection angle* (Fig. 1.1). Although he was the first to calculate the deviation of light, his notes were never published and remained unknown until 1988 [8]. 20 years later, the German physicist and astronomer Johann Georg von Soldner published, with small variations, the same result [9]. Using eq. (1.1) he estimated the deflection angle of a light ray that is deviated due to the gravitational field of the Sun. For $M = 1.989 \times 10^{30}$kg and $R = 6.957 \times 10^{8}$ m, the result yields $\alpha = 0.875$ arcsec.

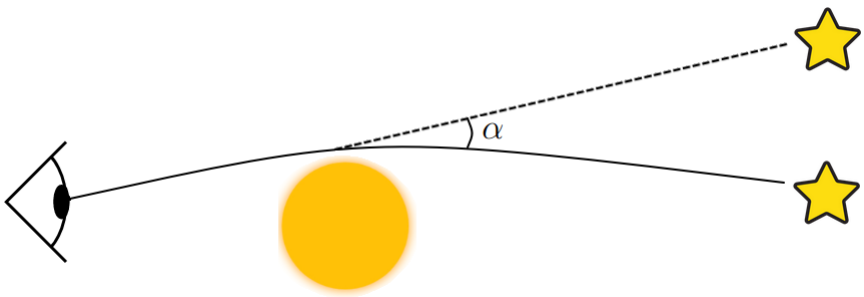


Figure 1.1: Sketch of a light ray deflected by an angle $\alpha$ due to the gravitational field of the Sun. The dotted line indicates the position of the star if the light would not have been deflected.

The idea on how the speed of light would accelerate due to the gravity of a star was also developed independently by the French polymath Pierre Simon Laplace in 1796 [10]. Using this, Michell argued in a paper in 1783, that a star with a sufficiently strong gravitational pull could trap light, making it invisible. He referred to such object as a "dark star" and thought that the universe was filled with them [7]. Michell is therefore the first person known to have proposed the existence of black holes.

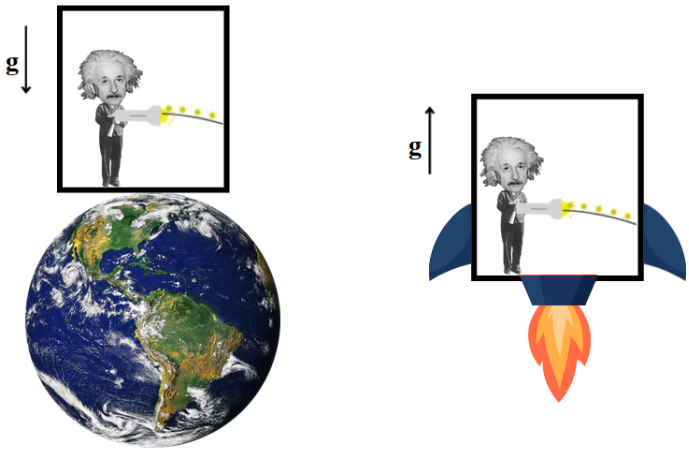


Figure 1.2: Imagine an observer with a flashlight in a spaceship that points to the other side of the elevator (right). Due to the relative motion between the light beam and the elevator, the trajectory would bend downwards. Due to the equivalence principle, this effect should also be noticeable on Earth (left).

The idea of light deflection is based on Newton's corpuscle theory of light. As previously mentioned, in 1802 Thomas Young settled the debate about the nature of light in favour of the wave theory. For this reason, the idea was abandon and it was not revisited for over a century. It was not until 1907 that a young German physicist at the patent office had the "happiest idea of his life" and revived the idea of light deflection.

## 1.2 The *Gedankenexperiment*

In a regular day at work at the patent office in 1907 in Bern (Switzerland), young Albert Einstein was sitting at his desk thinking about his reviewed article about the theory of relativity when he carried out a mental experiment (*Gedankenexperiment*) that summarizes, in Einstein's own words, as follows: "If a person falls freely, he does not feel his own weight". This reflection amazed Einstein so much that years later called it "the happiest idea of his life" [11, 12]. From this happy thought, Einstein built the equivalence principle [13], which sets the basis of the first version of the General Theory of Relativity.

One of the main consequences of the equivalence principle applies directly to light. To illustrate this effect let us consider an observer in a windowless elevator. Imagine what would happen if we took a flashlight and pointed it from one side of the elevator to to the wall of the spaceship. Since the floor of the elevator would be rushing upwards the light beam would appear to curve downward (Fig. 1.2). Relative to an inertial frame (at rest in a gravity-free region) light still propagates in a straight line. On the other hand, according to the equivalence principle, the accelerated frame is indistinguishable from a homogeneous gravitational field. This means that light must

bend in a gravitational field. Gravity attracts light! As a result, since light always takes the shortest path between two points, Einstein realized that its trajectory should correspond to a curved line. Consequently, in the presence of mass and energy, space becomes curved. This was the key insight that Einstein had about gravity. The curved geometry forms the basis of General Relativity, in which gravity is entirely geometrical by nature.

When Einstein studied this gravitational bending effect of light in 1907 he thought that it was too small to be observed and did not give it much thought. In Prague, however, he corrected this last consideration, noting that a beam of light that passes grazing through the solar disk, would be deflected by a small but measurable angle. Therefore, a star that is very close to the Sun would appear slightly deviated from the position we attribute to it when the Sun is far away. In 1911, based on his Theory of Special Relativity, he published the calculation of the deflection angle [14] whose result was precisely the same as that previously derived by Cavendish (Eq. 1.1). Einstein showed that this phenomenon would in principle be observable during a solar eclipse, because when direct sunlight is covered we would be able to see the star close to the Sun and measure its deviation. However, in 1915 he formulated his theory of general relativity and, using the equivalence principle, repeated the calculation of the deflection angle and obtained an unexpected result [15]. The purely Newtonian deviation appeared, due to the "weight" of light, as expected, but also another of equal magnitude and purely relativistic (or post-Newtonian) due to the curvature of space induced by the presence of the Sun [11]. As a result, the deviation of light turns out to be twice that of its previous versions, i.e.,

$$\alpha(R) = \frac{4GM}{c^2 R}. \tag{1.2}$$

The deviation angle of light due to the gravitational field of the Sun predicted by the General Theory of Relativity is therefore 1.75 arcsec. Einstein then insisted on the possibility of verifying his theory in an upcoming solar eclipse. Europe was at war and it was not possible to carry out this task soon, but even so, the Royal Astronomical Society of London organized a couple of expeditions to take advantage of the solar eclipse of May 29, 1919. The result of that eclipse changed completely the history of light deflection and it was precisely that phenomenon, to which Einstein did not give much thought, that took him to the pinnacle of fame.

## 1.3 The eclipse

The verification of the light deflection phenomenon was essential for Einstein. In 1911, he sent a paper to the prestigious journal "Annalen Der Physik" entitled *On the influence of gravitation on the propagation of light* [14]. Erwin Freundlich, a young assistant of the Institute for Cosmic Physics at the German University in Prague was stunned about his work and offered his help in developing methods for observing the deflection of light near the Sun or the planet Jupiter [16]. However, observing a solar

eclipse for scientific purposes was challenging due to the intricate planning, logistics, and funding required. Due to these factors, Freundlich initially dismissed the idea of organizing an expedition to observe the next solar eclipse. However, that year, the astronomer Charles Dilon Perrine, an expert in solar eclipse observation who was in charge of three expeditions for the observation of solar eclipses in Sumatra (1901), Spain (1905) and Flint Island (1908) [17] and whose aim was to detect the presence of the new planet "Vulcano" visited the observatory and encouraged Freundlich to reach out to other astronomers who may have old eclipse plates to study the light deflection effect. While Freundilich was waiting to receive the plates, Perrine was organizing an expedition to observe the next solar eclipse, on October 10, 1912, in Brazil, in which, thanks to Freundlich, light deflection measurements were included in the observation program. In the English delegation was a young Arthur S. Eddington who had dinner in Rio de Janeiro with Perrine. If they talked about Einstein prediction of light deflection, it may have been the first time that Eddington learned about the new theory of gravitation and its observable effects. Unfortunately, the intense rain completely ruined the scientific missions. As consolation, if the measurement of light deflection had been carried out, the value obtained would have been twice that predicted by Einstein, since he obtained it with his Theory of Special Relativity.

Einstein corresponded with several other astronomers over the course of months and years to bring attention to the significance of his theory and seek their assistance in refining his predictions through astronomical observations. One of these astronomers was Sir George Ellery Hale, Director of the Mount Wilson Observatory, which had the largest operational telescope in the world at the time [18]. In his letter to Hale in October 1913, Einstein asked for guidance on how to measure the positions of distant stars around the Sun during daylight. He wanted to compare these positions with those taken at night when the Sun was absent to assess the effect of the Sun's mass on light's path. In November, Hale replied that it was impossible to make these measurements during sunlight, but expressed his belief in the potential for doing so during a total eclipse.

The next opportunity for light bending verification was during the total solar eclipse of August 21, 1914. Freundlich found support from Einstein and Max Planck and led the expedition in Crimea. However, the outbreak of the First World War and the climatic hostilities frustrated again the observation of the eclipse.

Between the eclipse in Russia from 1914 to 1919, there was a renewed interest in the works of Albert Einstein. General Relativity was already published and groups of foreign astronomers began to compete to be the first to test Einstein's predictions.

In early 1919, the British intended to send two expeditions to observe the eclipse in May of that year and test Einstein's predictions. Arthur S. Eddington, who became interested in Einstein's work thanks to the Dutch astronomer Willen de Sitter, would lead the expedition. On the other hand, Freundlich was determined to organize an expedition to observe the 1919 ellipse, if the war ended in time. Unfortunately, the

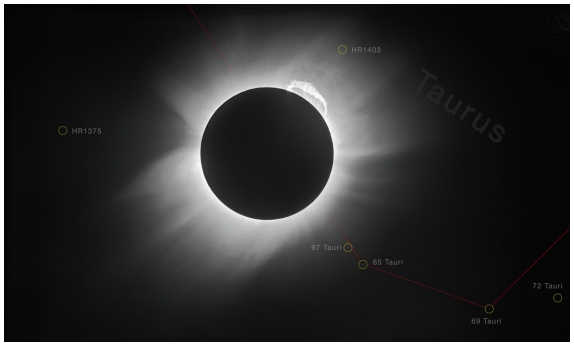


EINSTEIN THEORY TRIUMPHS

Stars Not Where They Seemed or Were Calculated to be, but Nobody Need Worry.

Figure 1.3: *Left*: One of the pictures of the solar eclipse taken in May 29, 1919 in Sobral (Brasil). Credit to ref [20]. *Right*: Fragment of the news published in the New York Times on November 10, 1919.

Russians confiscated all his instruments when World War I broke out, and Freundlich would have to wait.

This eclipse was particularly promising for measuring the light deflection effect since the Sun passed through the star cluster Hyades, located in the constellation Taurus which contains a large number of bright stars. The eclipse was visible across Africa, the Atlantic Ocean, and South America. A first expedition made up of Eddington was based on Príncipe Island. The second expedition was located in Sobral, in northern Brazil. The day of the eclipse the weather was favorable and the team was able to photograph the phenomenon (fig. 1.3). The team led by Eddington measured a deviation angle of $1.61 \pm 0.30$ and the team located in Sobral obtained a result of $1.98 \pm 0.12$ [19]. Both results were compatible with Einstein's prediction although the result given by Eddigton is considered more reliable. The announcement of the results was on November 6, 1919, at a joint meeting of the Royal Society and the Royal Astronomical Society where the representative of the expedition in Sobral proclaimed that "after a detailed study of the plates I am prepared to say that there is no doubt that they confirm Einstein's prediction. A definitive result has been obtained that light is deflected according to Einstein's law of gravitation." Einstein became famous overnight (fig. 1.3).

## 1.4 The amplification of light

The term *gravitational lensing* was born in 1919 to describe a massive object (the *lens*) that bends the light of a luminous source. It seems to have been introduced by the British physicist and writer Sir Oliver Joseph Lodge, who remarked that it was "impermissible to say that the solar gravitational field acts as a lens, for it has no focal length" [21]. That same year, Eddington discussed the possibility of observing a double image as a result of gravitational lensing and determined that the light deflection would cause such a significant reduction in its intensity that it would be unnoticeable when it reaches us. This idea was further explored by the Russian physicist Orest

Chwolson, who indicated that a gravitational lens would produce a secondary image that forms a fictitious double star which could not be seen by a telescope [22]. He added that, in case of perfect alignment between the background and the foreground star that act as a lens, the two images would stretch out forming a ring (fig. 1.4). Although it would be more accurate to call this effect "Chwolson Ring", it is today usually called "Einstein Ring".

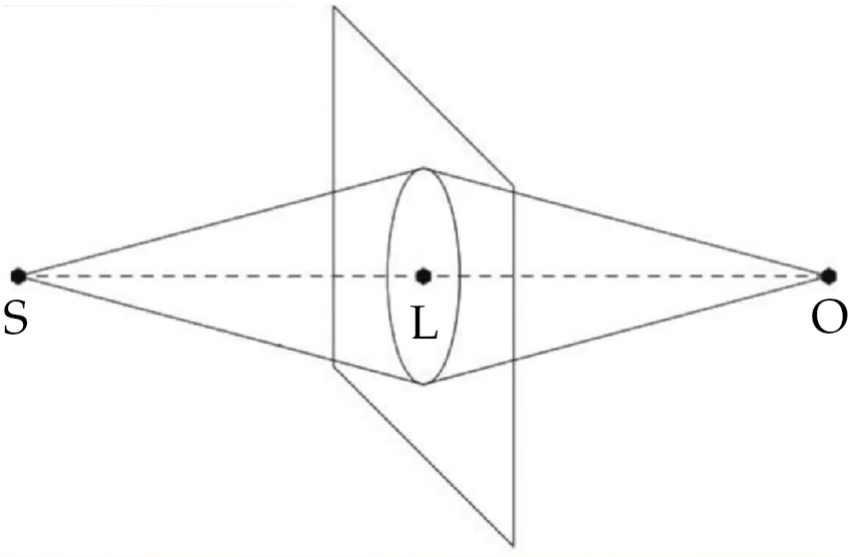


Figure 1.4: When the light source (S), the lens (L) and the observer (O) are perfectly aligned, the lens produces a ring shaped image.

In 1936, Einstein, who was a professor at Princeton, did not have many expectations to find astrophysical applications using gravitational lensing. However, a Czech amateur electrical engineer named Rudi Mandl persuaded him to further explore its applications. In particular, he proposed a basic model comparing gravitational light deflection to the action of a lens in geometrical optics. Using this idea, Einstein published a short calculation named *Lens-Like Action of a Star by the Deviation of Light in the Gravitational Field* [23] in which he suggested that the apparent luminosities of the images of a background star could be changed due to gravitational lensing. In particular, if the observer, the lens and the light source are sufficiently aligned, light would tend to be focused on the observer and the image is could be highly magnified. However, in Einstein's own words "*Of course, there is no hope to observe this phenomenon directly*" since the chances of this alignment are very low. However, years later, it was discovered that there are regions of the sky so dense that it is likely to find these alignments. Furthermore, thanks the the observations of the American astronomer Edwin Hubble, it was realized that there exist many galaxies besides ours and groups of them held by gravity, named galaxy clusters [24].

Mandl discussed the potential scope of gravitational lensing with other scientists and finally arrived to the Swiss astronomer Fritz Zwicky. He suggested that multiple

images due to gravitational lensing should be observed in the future. If a lens is able to produce multiple images, the regime is called *strong gravitational lensing*. Motivated by this, a year after Einstein showed that amplified images can be observed, he published a short paper entitled *Nebulae as Gravitational Lenses* [25] in which he stated that this effect is more likely to be observed if one considers larger structures as lenses, such as galaxies and galaxy clusters [1], rather than a single star. The reason is that the magnification of the image produced by these structures is higher. As a consequence, this amplification effect enables to observe galaxies at far greater distances than what was currently possible with the largest telescopes on Earth. In a second paper entitled *On the masses of nebulae and of clusters of nebulae* [26] he studied the possibility of using gravitational lensing to determine galaxy masses and how matter is distributed. This is currently one of the main applications of gravitational lensing.

However, the revolutionary statement arrived in 1933 when Zwicky was styding the motion of the Virgo and Coma clusters of galaxies. He used the virial theorem to obtain the expected mass of these *nebulae* and observed that was not sufficient to explain the observed large speeds of the galaxies in the cluster. He proposed the existence of an unseen or "dark" form of matter that could account for the discrepancy [27]. This idea was met with skepticism at the time, but subsequent observations and studies have confirmed the presence of dark matter and its critical role in shaping the universe. Today, the content of dark matter is considered one of the most mysterious and intriguing mysteries in astrophysics, and Zwicky's work is widely recognized as a key early contribution to our understanding of this phenomenon. He also stated that dark matter should produce gravitational lensing effects.

## 1.5 The theoretical research and the first observation

Just like the idea of light deflection was abandoned until Einstein built the equivalence principle, the field of gravitational lensing remained on "stand-by" until a new discovery came to light. This happened in 1963, after Einstein died, thanks to the Dutch astronomer Maarten Schmidt. After World War II, radio astronomy underwent rapid advancement, resulting in the identification of mysterious radio wave sources that appeared to be extremely faint stars in the optic band. Using the Hale telescope, Schmidt examined the spectra of several stars, especially 3C273, and found that it was moving at a speed of 40,000 km/s, clearly indicating that it was an extragalactic object. To account for its apparent brightness, 3C273 had to have a massive luminosity, forty times that of an ordinary galaxy. By repeating the experiment with 3C48, Schmidt obtained similar results [28]. In 1964, 3C273 and 3C48 were designated 'Quasi-Stellar Objects' by the Taiwanise-American astrophysicist Hong-Yee Chiu [29], and the terminology was later abbreviated by astronomers to form the current term *quasar*. Due to their huge intrinsic luminosity, quasars were thought to be ideal sources

[1] In the article, he used the term *nebulae*

to observe gravitational lensing effects.

After the discovery of the first quasar, the field of gravitational lensing reopened. Yuri Klimov, Sydney Liebes and the Norwegian astrophysicist Sjur Refsdal studied the effect from a geometrical point of view. They are considered to be the founders of modern theoretical research on gravitational lensing. Klimov [30] studied the effect of gravitational lensing of galaxies on galaxies, in particular ring-shaped and multiple images. Liebes [31] contemplated lensing of stars on stars, lensing by globular clusters and lensing by objects such as asteroids and planets within the Milky Way. He also considered lensing of extragalactic sources by the stars in our galaxy and estimated the probability of lensing detection. In 1964, Refsdal [32] was the first to study the possibility that the light rays emitted by a distant luminous source could traverse different and multiple paths around a lens. He added that these light rays would arrive to the observer at different times. He was therefore the first to introduce the concept of *time delay*. He applied this idea and supposed that the source is a Supernova. Due to the time delay, one would observe multiple explosions at different times. Refsdal also studied possible astrophysical application of gravitational lensing[2]. In particular, he proposed to measure the time delays between the multiple images of a supernova to obtain the mass of the lens and the expansion rate of the universe, known as the *Hubble constant*. Furthermore, he introduced the idea that quasars' luminosities may be variable and that they coud be used to measure lens masses and the Hubble constant.

At that time, the observational technology was well behind the theoretical research. For that reason, the next decade represented a significant progress from the theoretical perspective.

The Soviet physicists Yakov Zeldovich and Igor Novikov in 1967 [33] and especially the English theoretical physicist Stephen Hawking and his PhD student Bernard Carr in 1971 proposed which is to date the only known example of massive compact halo object (MACHO): *primordial black holes* (PBHs). In their work *Gravitationally Collapsed Objects of Very Low Mass* [34] they discussed how these structures are formed. It occurs at the end of inflation if quantum fluctuations of space-time curvature generate high-amplitude peaks. After reheating, these peaks become high-density regions dominated by radiation energy, which can be viewed as high-photon-density regions. If the density is high enough, gravitation is stronger than radiation pressure, leading to the collapse of these regions into black holes. PBHs could make up a significant fraction of the dark matter (see e.g. ref. [35] and references therein). Other MACHO candidates, such as neutron stars, planets or brown dwarfs, were excluded later by a variety of cosmological constraints implying that dark matter must be non-baryonic; those notably include the precision measurement of the CMB acoustic peaks and the abundance of light elements predicted in the context of the hot big-bang nucleosynthesis – see e.g. chapters 6–8 of ref. [36] for a detailed historical review.

[2]This is the reason why the first lensed supernova was named "Refsdal".

In 1973, two years after Hawking proposed the existence of PBHs, the American astrophysicists William Press and James Gunn [37] suggested observational tests to confirm the presence of a cosmologically significant density of compact bodies using gravitational lensing. In particular, they claimed that the probability of a distant point source being gravitationally lensed into two roughly equal images is high if the universe is populated with compact objects.

In 1979, thanks to the technological progress to increase the sensitivity of the telescopes and cameras, the first gravitational lens was finally found. The Anglo-American team led by the astronomers Dennis Walsh, Robert Carswell and Ray Weyman [38] detected from a radio survey two quasars QSO 0957+561A/B at redshift $z = 1.413$ with an angular separation of 6 arcsec (fig. 1.5).

Figure 1.5: Recent observation of the quasar QSO 0957+561 (center of the image), the first gravitational lensing detection. Credit: NASA/ESA Hubble Space Telescope

The team observed that the proximity between the two quasars was unusual and their redshift and visible light spectrum were highly similar. With the further detection of a lens galaxy at $z = 0.39$ [39], it was concluded that there were not two quasars but two multiple images of a single one.

## 1.6 Microlensing and current status

In 1979, the South Korean astrophysicist Kyongae Chang and Refsdal [40] studied the flux variations of QSO Q0957+561 A,B and published a landmark paper that explored the effect of stars located between the observer and the observed quasars on the brightness of the quasar image. In particular, they suggested that, although the multiple images can not be observed due to the resolution of the telescopes, the amplified apparent luminosity of the quasar might be. This magnification effect, which was first suggested by Mandl when discussing with Einstein in 1936, is called *microlensing* and this was the first time that the term was introduced. This regime is used when the angular separation between the multiples images is less than one milli-arcsecond. Furthermore, Chang and Refsdal proposed to use this enhanced brightness to search for compact objects. Although Refsdal was disappointed for not observing multiple images and therefore, time delays in quasar lensing events to obtain the Hubble constant, he created a new line of research.

In 1981, the British astrophysicist Peter Young, who identified the galaxy responsible for the first gravitational lens system QSO 0957+561, used computer simulations to obtain variable star light curves due to microlensing [41]. The American astrophysicist Richard Gott, who performed similar calculations to obtain light curves, suggested that the intensity of the quasar images could be due to microlensing effects of individual low mass stars and claimed therefore that stellar microlensing is observable [42]. As an illustration of star light curves due to microlensing, the graph of fig. 1.6 has been obtained by monitoring the luminosity of a star (S) for about three years. Between, roughly, day 400 and day 600, another star (L) passed on the line of sight, producing an enhancement of the apparent luminosity of S.

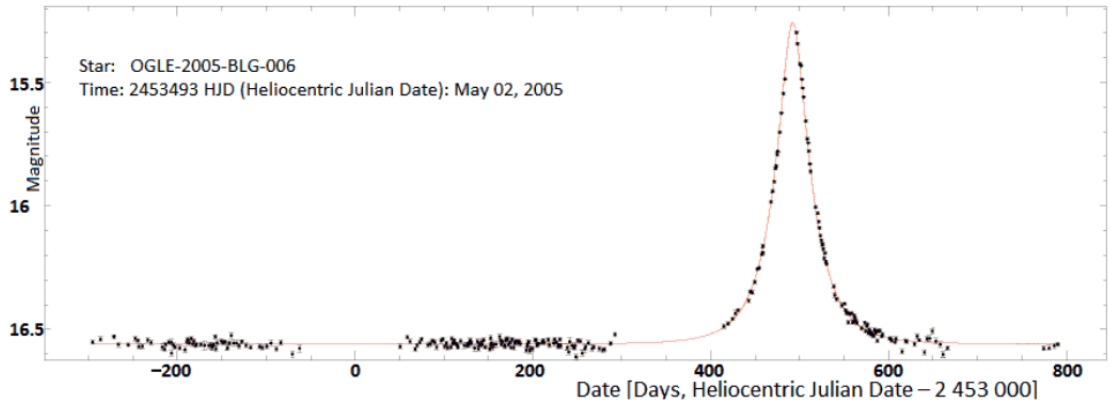


Figure 1.6: Gravitational amplification of a star by another star acting as a lens. The data was taken by the OGLE project in 2005. Credit to Jan Skowron, data from OGLE.

However, the turning point arrived in 1986 thanks to the Polish astronomer Bohdan Paczyński. He argued that gravitational lensing, which has the virtue of being directly

sensitive to the distribution of mass, as opposed to the astronomical observations which rely on luminous matter, could be a suitable probe of the clumpiness of the dark matter. In particular, he suggested that microlensing could be a useful tool to detect compact objects in the Galactic halo. The idea is that, as a compact object crosses the line of sight of a distance source, it temporarily magnifies its apparent brightness [43]. He showed that galactic microlensing should be observable and created the Optical Gravitational Lensing Experiment (OGLE), the first large-scale photometric survey. The aim of the experiment was to look for microlensing events towards the Magellanic Clouds, that were considered the best target due to the large number of source background stars, and place upper limits on the contribution of compact bodies to the dark matter halo in our galaxy. At the same time, Kayser, Refsdal and Stabell [44] studied the changes in luminosity that occur when a compact source crosses a critical curve. [3]

The first detection of a microlensing event arrived in 1989. A team led by the British astronomer Michael Irwin presented photometric data for the gravitationally lensed quasar system 2237+0305 and observed a change in brightness in one of the four component images [45]. Remembering Einstein's famous quote "Of course, there is no hope to observe this phenomenon directly", 53 years were needed to prove him wrong. The idea of using quasar microlensing for detecting a cosmologically significant density of compact bodies was further investigated in the coming years by Hawkins [46, 47] and Hawkins and Verón [48] who studied the structure of dark matter using quasar light curves, and Schneider [49], who constrained the population of compact objects that could make up the total matter density.

The first microlensing detection was a motivation to put Paczyński's idea of detecting compact objects in the Galatic halo into practice. This was done by the MACHO experiment [50], which looked for microlensing events in the Magellanic Clouds for several years in the 90s by monitoring thousands of stars hoping that some compact objects in the mass range $3 \times 10^{-4}$ to $0.06\, M_{\odot}$ would cross the line of sight and amplify their brightness. Among the 9.5 million light curves that were analysed, only 3 events consistent with microlensing were found. After similar analyses were conducted by the EROS and OGLE collaborations [51, 52], the possibility that the dark halo of our galaxy is made of compact objects in that mass range was excluded. Those constraints keep being discussed today in the literature; for instance ref. [53] argues that detection method presented inconsistencies; ref. [54] suggests that the constraints may be alleviated if the compact objects are clustered. Importantly, galactic microlensing is inefficient at detecting high-mass compact objects [55].

The difficulty of constraining the abundance of high-mass compact objects in our galactic halo motivated the observation of microlensing effects in images of multiple imaged quasars [56, 57, 58]. Microlensing can also manifest as flux ratio anomalies

[3] For a given lensing system, a *critical curve* is the set of image positions $\boldsymbol{\theta}$ whose partial amplification is infinite.

between multiple quasar images [59, 60, 61], which may be interpreted as a direct proof for the presence of CDM substructure around lensing galaxies.

One possible alternative to detect extragalactic microlensing due to compact objects beyond the solar mass is via supernova lensing. As mentioned above, Refdsal was the first to study the possibility of observing this phenomenon and use SNe as a cosmological probe. Since then there have been many research programmes looking for strong gravitational lensing of SNe [62], where microlensing is a potentially worrisome source of noise. The idea of using SN microlensing as a signal, to constrain the abundance of compact objects was first proposed by Linder, Schneider and Wagoner [63] in 1988. Rauch [64] and Metcalf and Silk [65] only considered two scenarios: all and none of the DM in the form of compact objects. Seljak and Holz [66] already contemplated that a fraction of DM in compact objects can be measured with any given SN survey [67]. The constraints were updated 7 years later by Metcalf and Silk [68], and most recently by Zumalacárregui and Seljak [69]; see also refs. [70, 71].

Another method to constrain compact dark matter, motivated by the recent discoveries of the highly magnified stars MACS J1149 Lensed Star 1 ("Icarus") [72] and WHL0137-LS ("Earendel") [73], both visible at cosmological distances, uses caustic-crossing events in giant arcs. This mechanism allows the detection of compact objects in the subsolar-mass regime.

As seen in this section, after the first gravitational lens was finally detected and microlensing was discovered, there has been a "boom" in the creation of new lines of research on this phenomenon. However, in 2015, an event that would forever change the way of doing astrophysics occurred. The LIGO/Virgo Collaboration [74] reported the first detection of a gravitational-wave signal, "ripples" in space-time caused by some of the universe's most explosive and energetic phenomena and predicted by Einstein in 1915 in his theory of general relativity. Since then, the interest in using microlensing to detect compact objects has been once again at the forefront. Consequently, all the aforementioned methods share the need of an accurate modelling of the microlensing statistics.

## 1.7 Modelling of the microlensing statistics

From the theoretical perspective, all the aforementioned methods share the need, in particular, of an accurate modelling of the probability density function of the lensing amplification, $p(A)$. This theoretical effort started in the 80s with the works of Peacock [75]; Turner, Ostriker, and Gott [76]; and Dyer [77]. They were the first to compute analytically and show predictions of the probability that the light of a distant quasar is lensed by compact objects. They determined that low-mass lenses can cause high amplifications.

In 1986 Paczynski [43] determined that the probability distribution of a point

source exhibits a $A^{-3}$ behaviour for large amplification. Years later, Schneider [78] and Seitz and Schneider [79] arrived to the same result. Still more elaborate analyses helped understanding the non-linear interaction between lenses [78, 80, 81, 82, 83, 84, 85]. Besides, a number of ray-shooting numerical simulations were performed to assess the accuracy of those theoretical works [44, 86, 64, 87].

However, those past analysis generally focused on a fraction of the effects potentially affecting the amplification statistics. The motivation of this thesis is to extend and improve upon them by proposing an accurate modelling of the statistics of extragalactic microlensing from first principles. Our model accounts for line-of-sight effects and lens-lens coupling in the mild-optical-depth regime, and extended-source corrections. The end product is a semi-analytical expression for the amplification probability, in a realistic universe whose dark matter is made of a certain fraction of compact objects.

The remainder of Part I is organised as follows. In chapter 2, we discuss on the notion of microlensing optical depth, its role in amplification statistics, and we evaluate its relevant values in practice. In chapter 3 we account for the environment and line-of-sight corrections of a single point lens; we turn this result into a probability density function for the amplification in chapter 4, where we also compare the predictions of the most recent analysis to our approach. We consider extended-source corrections in chapter 5 and conclude in chapter 6.

CHAPTER

# TWO

# OPTICAL DEPTH AND EXTRAGALACTIC MICROLENSING

This chapter is a preliminary discussion on the notion of microlensing optical depth, denoted $\tau$, which will be central in the discussions. After providing definitions of $\tau$, and illustrating its role in amplification statistics, we demonstrate that microlensing by extragalactic compact objects is characterised by a low, although not very low, optical depth.

## 2.1 Intuition and definitions

Consider a population of compact objects distributed in space. In this thesis, compactness will be defined in the sense of lensing rather than in the sense of gravitation: a compact object will loosely refer to a celestial body capable of producing multiple images and strong amplifications of point sources. Let us model such objects as point lenses. As illustration, consider the situation of a single point lens depicted in fig. 2.1. A light ray emitted by a source S is deflected by a spherically symmetric distribution of mass $m$ by an angle $\alpha$ following eq. (1.2). The angles $\beta$ and $\theta$ are the unlensed and lensed position of the image of S and $b$ is the impact parameter, which corresponds at lowest order to the minimal distance between the photon and the mass in the trajectory (equivaent to $R$ in eq. (1.2)). $D_{\rm od}$ is angular-diameter distance to the lens (or deflector), $D_{\rm os}$ is the angular-diameter distance to the light source (in the absence of the lens) and $D_{\rm ds}$ is the angular-diameter distance to the source as seen from the lens.

Let us call $d$ the distance between the source S and the axis. If $\beta$, $\theta \ll 1$, then

$$d = \beta D_{\rm os} = \theta D_{\rm od} + (\theta - \alpha) D_{\rm ds} \tag{2.1}$$

Substituting for $\alpha$ and dividing by $D_{\rm os}$ we obtain

$$\beta = \theta - \frac{4GmD_{\rm ds}}{D_{\rm od}D_{\rm os}}\frac{1}{\theta} \tag{2.2}$$

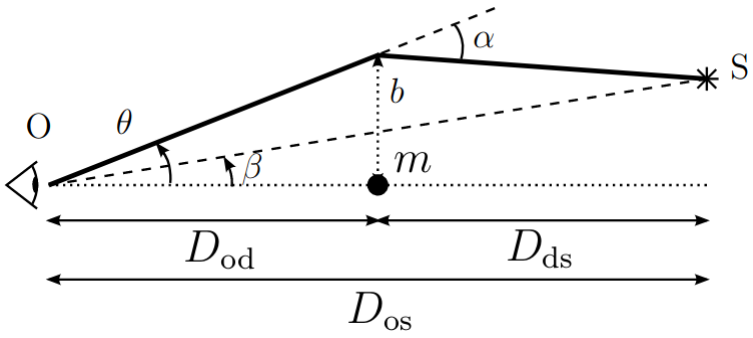


Figure 2.1: Sketch of all the quantities involved. A light ray emitted from a source at $D_{\rm os}$ is deviated by a point lens at $D_{\rm od}$.

which is the *lens equation* of a point mass lens. It relates the position of the source and its image. The prefactor in the second term of the right-hand side of eq. (2.2) contains all the information of the lens. Each lens is then fully characterised by its so-called *Einstein radius*

$$\theta_{\rm E} \equiv \sqrt{\frac{4GmD_{\rm ds}}{D_{\rm os}D_{\rm od}}}\ , \tag{2.3}$$

so the lens equation reads

$$\beta = \theta - \frac{\theta_{\rm E}^2}{\theta}. \tag{2.4}$$

and the solutions are

$$\theta_\pm = \frac{1}{2}\ \beta \pm \ \overline{\beta^2 + 4\theta_{\rm E}^2} \tag{2.5}$$

which corresponds to the fact that light can pass 'above' or 'below' the lens in fig. 2.1.

The Einstein radius technically represents the size of the ring that would be observed if a point source were exactly aligned with the lens (fig. 1.4). But it also gives an idea of the lensing *cross section* of the lens. If the angle $\beta$ separating the source and the lens on the celestial sphere is comparable to $\theta_{\rm E}$, then the image's total flux is appreciably amplified compared to the source; if on the contrary $\beta \gg \theta_{\rm E}$, then the amplification is close to unity. More precisely, the amplification factor $A \equiv F_{\rm o}/F_{\rm s}$ between the observed flux $F_{\rm o}$ and the unlensed source's flux $F_{\rm s}$ is obtained from the inverse of the determinant of the *amplification matrix*, $\boldsymbol{\mathcal{A}}$. Representing the angular positions of the sources and images by 2-dimensional vectors[1], it is defined as the Jacobian matrix of the mapping from $\boldsymbol{\theta}$ to $\boldsymbol{\beta}$.

$$\mathcal{A}_{ab} \equiv \frac{\partial \beta_{ab}}{\partial \theta_{ab}} \tag{2.6}$$

By taking the derivative of eq. (2.2) we get

$$\mathcal{A}_{ab} = -\frac{2\theta_{\rm E}^2}{\theta^4}\theta_a\theta_b + \ \ 1 - \frac{\theta_{\rm E}^2}{\theta^2}\ \ \delta_{ab} \tag{2.7}$$

[1]We can make this approximation because $\theta$ and $\beta$ are very small.

and the determinant is therefore

$$\det \boldsymbol{\mathcal{A}} = 1 - \left(\frac{\theta_{\rm E}}{\theta}\right)^4 . \tag{2.8}$$

If we substitute in the previous formula the image positions of the point mass lens, which are just the solutions of the lens equation (eq. (2.5)), and take its inverse we obtain

$$A_\pm = \frac{1}{2} \pm \frac{u^2+2}{2u\sqrt{u^2+4}} \quad , \qquad u \equiv \frac{\beta}{\theta_{\rm E}} \, . \tag{2.9}$$

Finally, assuming that $u > 0$ and that the absolute value brings a minus sign to one of the $A_\pm$, the amplification factor reads, for a point lens [88],

$$A = A_+ + A_- = \frac{u^2+2}{u\sqrt{u^2+4}} \tag{2.10}$$

For $u = 1$, i.e. when the source is at the verge of the Einstein disk, we have $A_1 = 3/\sqrt{5} \approx 1.34$.

Assuming a fixed distance to a light source, we may now picture the Einstein disks of our population of lenses covering part of the celestial sphere. The probability that a certain light source gets significantly amplified is then naturally quantified by the fraction of the sky that is covered by Einstein disks. This fraction is called the *microlensing optical depth*,

$$\boxed{\tau \equiv \frac{1}{4\pi} \sum_\ell \pi\theta_{{\rm E},\ell}^2 = \Sigma \Big\langle \pi\theta_{\rm E}^2 \Big\rangle \ ,} \tag{2.11}$$

where $\Sigma$ denotes the angular density of lenses, i.e. the number of lenses per unit solid angle in the sky, and $\langle \ldots \rangle$ denotes a statistical expectation value. If the distribution of lenses is inhomogeneous, then $\tau$ may be considered a field on the sphere.

It is instructive to express the optical depth in terms of more standard cosmological quantities. Suppose that the compact lenses are placed in a homogeneous-isotropic FLRW universe with zero spatial curvature. Denote with $\rho_{\rm c}(t, \boldsymbol{x})$ their contribution to the physical cosmic matter density at time $t$ and position $\boldsymbol{x}$. Then eq. (2.11) reads (see e.g. ref. [89])

$$\tau = 4\pi G \int_0^{\chi_{\rm s}} {\rm d}\chi \, \frac{\chi(\chi_{\rm s} - \chi)}{\chi_{\rm s}} \, a^2(\chi) \, \rho_{\rm c}(\chi) \ , \tag{2.12}$$

where $\chi$ and $\chi_{\rm s}$ respectively denote the comoving distances of the lenses and of the source from the observer; $a$ denotes the cosmic scale factor, and the notation $a(\chi), \rho_{\rm c}(\chi)$ mean that those quantities are evaluated at $\chi$ down the FLRW light cone, that is at conformal time $\eta(\chi) = \eta_0 - \chi$ if $\eta_0$ means today. It is also implicit that $\rho_{\rm c}$ is spatially evaluated along a straight line, thereby giving $\tau$ an angular dependency from the inhomogeneity of $\rho_{\rm c}$. Note that eq. (2.12) is the expression of the weak-lensing convergence, if the mass of the point lenses were smoothly distributed. In that case, the average amplification, at first order in $\tau$ and neglecting the shear, would be

$$\langle A \rangle_{\rm wl} = 1 + 2\tau \tag{2.13}$$

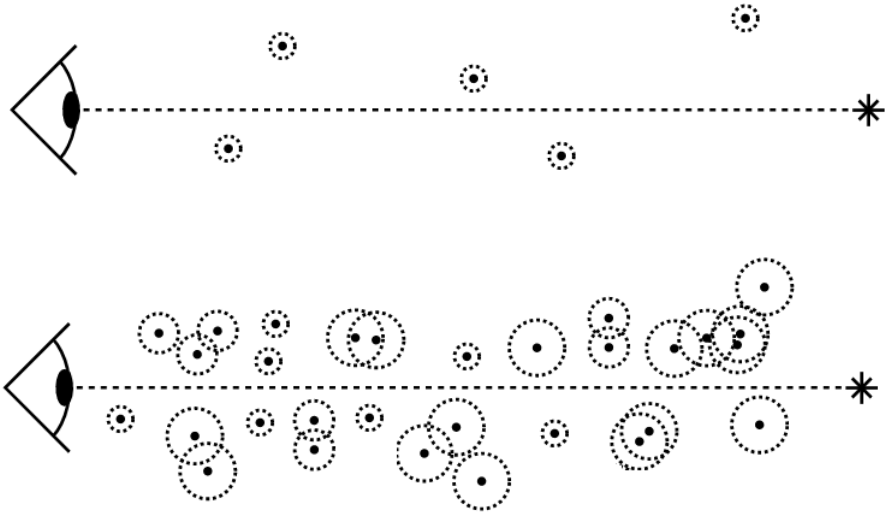

Figure 2.2: An extragalactic point-like source of light is observed through a fraction of the sky covered by $N$ lenses with their individual Einstein radii. *Top*: Region of the sky with a low optical depth ($N = 5$). Lenses are rare and well separated from each other. *Bottom*: Region of the sky with a high optical depth ($N = 30$). Lenses are common and interact with each other.

## 2.2 Amplification probability at very low optical depth

The problem of determining the statistics of microlensing amplifications turns out to be quite simple in the low-optical depth regime, $\tau \ll 1$. In this case, which corresponds to lenses being rare and well separated from each other, the total amplification produced on a given light source is well approximated by the amplification of the strongest lens of the population, i.e. with the smallest reduced impact parameter $u$ to the source. This shall be referred to as the *strongest-lens prescription*. It is then quite straightforward to derive the (complementary) cumulative distribution function (CDF) and probability density function (PDF) of the amplification [90, 89]

$$P(A;\tau) = 1 - \exp\ \left[-2\tau\ \left(\frac{A}{\sqrt{A^2-1}} - 1\right)\right] \quad , \tag{2.14}$$

$$p(A;\tau) = -\frac{\partial P}{\partial A} = \frac{2\tau}{(A^2-1)^{3/2}} \exp\ \left[-2\tau\ \left(\frac{A}{\sqrt{A^2-1}} - 1\right)\right] \quad . \tag{2.15}$$

The PDF displays the well-known asymptotic behaviour $p(A \gg 1;\tau) \propto 2\tau/A^3$ for high amplifications. It is also easy to check from eq. (2.15) that the average amplification reads

$$\langle A \rangle_{\rm c} = 1 + 2\tau \tag{2.16}$$

which agrees with eq. (2.13) at lowest order in $\tau \ll 1$. This means that the average magnification due to a sparse population of lenses equals the amplification

that would be produced by the same matter density if it were smoothly distributed in space.[2] Another remarkable property of the amplification PDF/CDF at very low optical depths is that *it does not depend on the mass of the deflectors*, but only on the optical depth. In that sense a sparse population of high-mass lenses is statistically indistinguishable from an abundant population of low-mass lenses.

## 2.3 Distribution of optical depth in a realistic universe

Given the simplicity of the amplification statistics in the low-optical depth regime, the first question that we need to address is whether or not this regime is a good description of extragalactic microlensing. A first way to address this question consists in estimating the optical depth in a realistic inhomogeneous universe containing a population of compact objects. Let $\alpha$ be the fraction of the total matter that consists of compact objects. For simplicity, the distribution of compact objects is assumed to closely follow the total matter density field: in a small region with density $\rho(t, \boldsymbol{x})$, there is a population of compact objects with mean density

$$\rho_{\rm c}(t, \boldsymbol{x}) = \alpha\, \rho(t, \boldsymbol{x}) \ . \tag{2.17}$$

We assume that $\alpha$ is constant in space and time. A concrete example of this scenario would be if a fraction $f_{\rm PBH} = \alpha/0.83$ of the DM were made of PBHs.

In such conditions, if we split the total matter density into cosmic mean $\bar{\rho}(t)$ and large-scale perturbations as $\rho(t, \boldsymbol{x}) = \bar{\rho}(t)[1+\delta(t, \boldsymbol{x})]$, where $\delta(t, \boldsymbol{x})$ denotes the density contrast, then the optical depth (2.12) takes the form

$$\tau = \alpha(\Delta_{\rm os} + \bar{\kappa}_{\rm os}) \ , \tag{2.18}$$

with[3]

$$\Delta_{\rm os} = 4\pi G\bar{\rho}_0 \int_0^{\chi_{\rm s}} {\rm d}\chi \ \frac{\chi(\chi_{\rm s}-\chi)}{\chi_{\rm s}} \frac{1}{a(\chi)} \ , \tag{2.19}$$

$$\bar{\kappa}_{\rm os} = 4\pi G\bar{\rho}_0 \int_0^{\chi_{\rm s}} {\rm d}\chi \ \frac{\chi(\chi_{\rm s}-\chi)}{\chi_{\rm s}} \frac{\delta(\chi)}{a(\chi)} \ , \tag{2.20}$$

where $\bar{\rho}_0 = \bar{\rho}(t_0)$ denotes today's cosmic mean density. If the universe were homogeneous on astronomical scales ($\delta = 0$), then we would have $\tau = \alpha\Delta_{\rm os}$; this

[2] This result was first obtained in 1976 by Weinberg [91], who thereby showed the important result that, at linear order, the average luminosity distance measured in a clumpy universe is the same as in the underlying homogeneous model. This was later generalised at any order by refs. [92, 93]; see also ref. [94] for details.

[3] The reason why we specified the subscript "os" in $\Delta_{\rm os}, \bar{\kappa}_{\rm os}$ will be clearer in chapter 3.

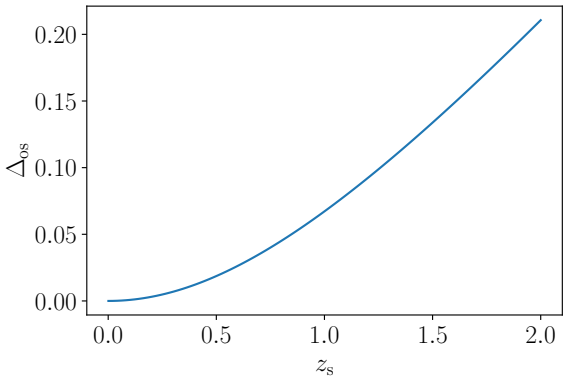


Figure 2.3: Evolution of the mean projected density term $\Delta_{os}(z_s)$ defined in eq. (2.19) as a function of the redshift $z_s$ of the source. We note that this quantity is non-negligible at high redshift, reaching about 10 % between $z = 1$ and 1.5.

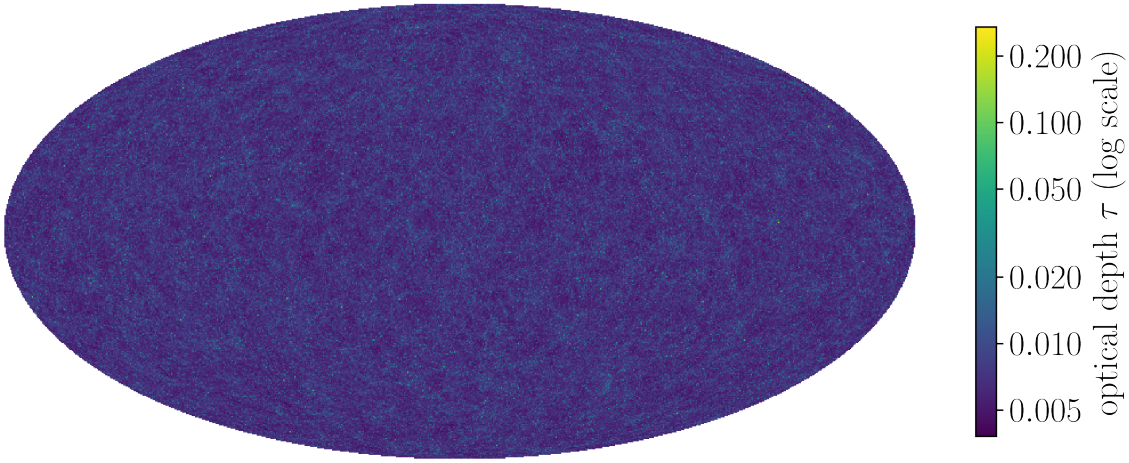


Figure 2.4: Simulated map of the microlensing optical depth $\tau$ (in logarithmic scale) in a universe with a fraction $\alpha = 0.5$ of compact objects, and a source at $z_s = 0.45$. The sky is dominated by very low values of $\tau$, with rare occurrences of mild values.

quantity thus represents the contribution of the mean cosmic density to the optical depth.[4] The evolution of $\Delta_{os}$ with the redshift $z_s$ of the source is depicted in fig. 2.3.

The second quantity in eq. (2.18), $\bar{\kappa}_{os}$, is a projection of the total density perturbation along the line of sight; it coincides with the weak-lensing convergence that would occur if matter were entirely diffuse, i.e., if the compact objects were smoothed out. For an overdense line of sight, $\bar{\kappa}_{os} > 0$, there are more compact objects and hence $\tau$ increases. We estimate the distribution of $\bar{\kappa}_{os}$ from a combination of (i) publicly available numerical results from ray tracing in an $N$-body simulation [96] and (ii) standard cosmological calculations; see chapter A for details on the simulation and our fitting functions.

For the sake of illustration, fig. 2.4 shows a sky map of the optical depth $\tau$ for $z_s = 0.45$ and a fraction $\alpha = 0.5$ of compact objects. More quantitatively, our

[4]Note also that $-\Delta_{os}$ represents the convergence of Zel'dovich's "empty-beam" [95], i.e., the negative convergence that would apply if light were propagating through an empty universe compared to FLRW.

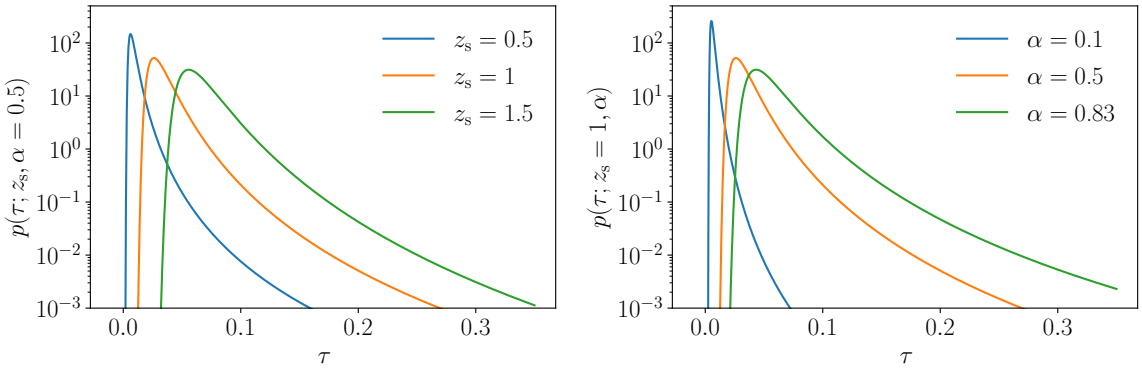


Figure 2.5: Probability density $p(\tau; z_s, \alpha)$ of the optical depth $\tau$ for a source at redshift $z_s$ in a realistic universe made of a fraction $\alpha$ of compact objects. *Left*: effect the source redshift for $\alpha = 0.5$. *Right*: effect of the fraction of compact objects for $z_s = 1$.

prediction for the PDF of the optical depth $\tau$ is shown in fig. 2.5 for various values of the fraction of compact objects $\alpha$ and of the source redshift $z_s$. We can see that, except for sources located at high redshift and for a fraction of compact objects approaching unity, the optical depth remains at most on the percent order for most of the lines of sight.

## 2.4 Relevant optical depths are not that low

The distributions shown in fig. 2.5 indicate that, except in rather extreme cases, most of the celestial sphere is characterised by a very low optical depth, thereby suggesting that the model of eq. (2.14) may be a good description of the amplification probabilities. However, this conclusion must be nuanced as we wish to focus on mild to high amplifications. Suppose for instance that we seek a microlensing signal in the Hubble diagram of type-Ia SNe, such as in refs. [65, 66, 68, 69]. To be detectable, the effect of microlensing should be larger than the intrinsic dispersion of SN magnitudes, $\sigma_{\rm int} \sim 0.1$ mag [97]. The decrease of an SN magnitude by $3\sigma_{\rm int}$ would be equivalent to an amplification factor $A = 10^{6\sigma_{\rm int}/5} \approx 1.3$, which is considerable.

Although regions with large optical depth $\tau$ are rare, they are also expected to produce more detectable amplifications than the low-$\tau$ regions. The relevant question then becomes: are detectable amplifications mostly lying in low-$\tau$ regions, which cover most of the sky, or in the rarer but more efficient high-$\tau$ regions?

To answer this question, we adopt the following protocol. Let us focus on events with amplification $A > A_1 = \sqrt{3}/5 \approx 1.34$ corresponding to sources falling within the Einstein disk of a lens, and which coincidentally produce a $3\sigma$ effect on type-Ia SNe. In a region with optical depth $\tau$, this has a probability $P(A_1; \tau) = 1 - \mathrm{e}^{-\tau}$ in the strongest-lens approach (2.14). So for the entire sky, the probability of such a

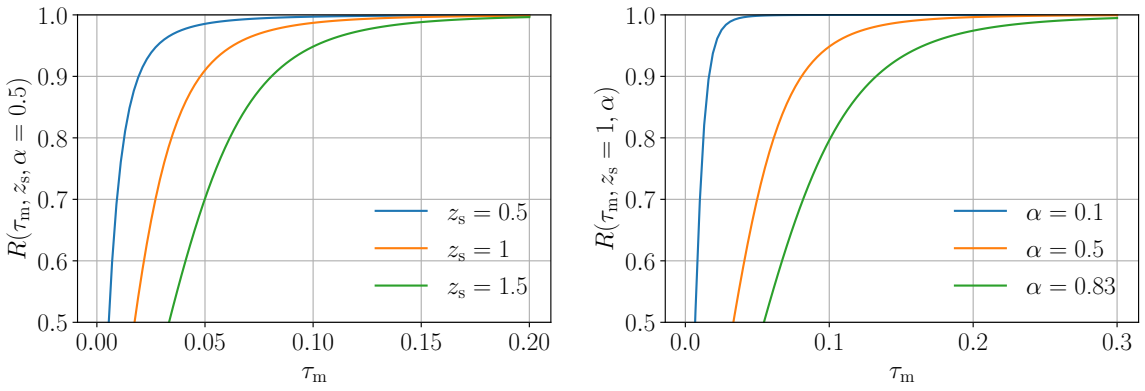


Figure 2.6: Proportion $R(\tau_\mathrm{m}, z_\mathrm{s}, \alpha)$ of the microlensing events with amplification $A > A_1 \approx 1.34$ occurring within regions of the sky with optical depth lower than $\tau_\mathrm{m}$, for a source at $z_\mathrm{s}$ in a universe with a fraction $\alpha$ of compact objects. *Left*: effect of the redshift of the source for $\alpha = 0.5$. *Right*: effect of the fraction of compact objects for $z_\mathrm{s} = 1$.

high-amplification event would be

$$P(A_1; z_\mathrm{s}, \alpha) = \int_0^\infty \mathrm{d}\tau \; p(\tau; z_\mathrm{s}, \alpha) \;\; 1 - \mathrm{e}^{-\tau} \quad , \tag{2.21}$$

for a fraction $\alpha$ of compact objects and a source at $z_\mathrm{s}$. Now suppose that we mask all the regions of the sky with an optical depth larger than $\tau_\mathrm{m}$; the probability would become

$$P_{\tau_\mathrm{m}}(A_1; z_\mathrm{s}, \alpha) = \frac{\int_0^{\tau_\mathrm{m}} \mathrm{d}\tau \; p(\tau; z_\mathrm{s}, \alpha) \, (1 - \mathrm{e}^{-\tau})}{\int_0^{\tau_\mathrm{m}} \mathrm{d}\tau \; p(\tau; z_\mathrm{s}, \alpha)} \; . \tag{2.22}$$

The ratio of those probabilities,

$$R(\tau_\mathrm{m}, z_\mathrm{s}, \alpha) \equiv \frac{P_{\tau_\mathrm{m}}(A_1; z_\mathrm{s}, \alpha)}{P(A_1; z_\mathrm{s}, \alpha)} \; , \tag{2.23}$$

then defines the fraction of high-amplification events that survive the masking operation; in other words, $R(\tau_\mathrm{m})$ is the proportion of high-amplification events happening in regions whose optical depth is lower than $\tau_\mathrm{m}$.

The evolution of the ratio $R(\tau_\mathrm{m}; z_\mathrm{s}, \alpha)$ as a function of $\tau_\mathrm{m}$ is depicted in fig. 2.6 for various values of $z_\mathrm{s}, \alpha$. For sources at high redshift, and for a non-negligible fraction of compact objects, we see that in order to properly account for, say, 99 % of the high-amplification events, we must allow the optical depth to reach values larger than 0.1. Hence, as far as high amplifications ($A > 1.34$) are concerned, the relevant regions of the sky do not necessarily have very low optical depths.

The general conclusion of the analysis conducted in this section is that we must a priori go beyond the simple model given by eqs. (2.14) and (2.15) in order to accurately model the statistics of extragalactic microlensing. This will be the purpose of the next

two sections, where we propose a complete set of corrections to the strongest-lens approach.

CHAPTER

# THREE

# POINT LENS WITH ENVIRONMENT AND LINE-OF-SIGHT PERTURBATIONS

The discussion of chapter 2 suggests that the simplest modelling of extragalactic microlensing statistics – the strongest-lens approach sketched in sec. 2.2 – may not be sufficient, because the relevant optical depths are low but not extremely low. In this context, we shall thus add perturbative corrections to this simple approach. We assume that when a source's light is significantly amplified, lensing is still mostly due to a single lens, which we may call the *dominant lens*. However, we now allow for corrections due to the rest of the universe – large-scale matter inhomogeneities, their substructure and the other compact lenses altogether – which we shall treat as tidal perturbations to the dominant lens.

In this section, we consider the problem of a single point lens that is perturbed by the presence of matter lumps in its environment and along the line of sight. We demonstrate that this problem can be suitably reformulated as a point lens with an external shear, and we derive the expression of the angular differential cross section $\Omega(A)$ of the amplification.

## 3.1 Description of the set-up

The concrete situation that we consider is depicted in fig. 3.1. An extragalactic point-like source (supernova or quasar) at $z_\mathrm{s}$ is observed through an inhomogeneous universe. On large scales, we assume that the inhomogeneity of the matter distribution is well described by the ΛCDM cosmological model. On small scales, we assume that a fraction $\alpha$ of the total matter density is made of compact objects, which we model as point masses.[1] Just like in sec. 2.3, we assume that the distribution of compact objects closely follows the total matter density field: in a region with

[1] Although binary systems are generally common in the universe, the separation between members of a binary is generally much smaller than their Einstein radius; hence binaries practically behave as point lenses.

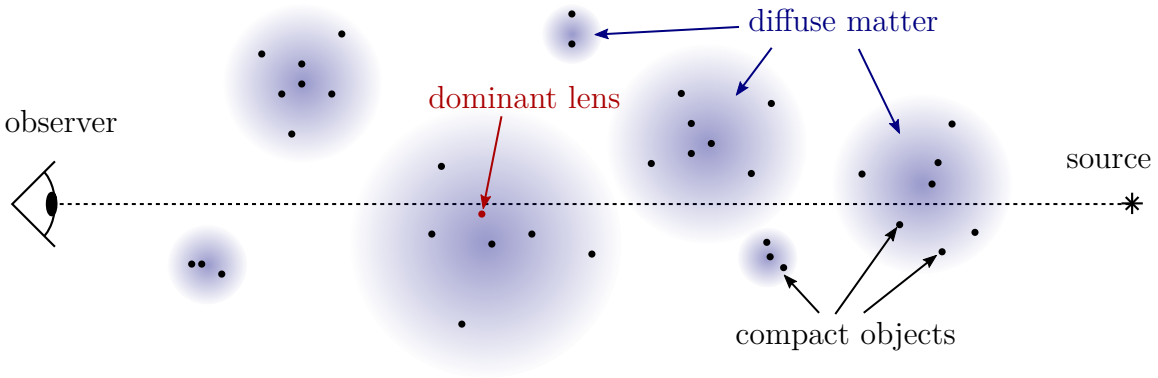


Figure 3.1: An extragalactic point-like source of light is observed through the inhomogeneous universe. A fraction $\alpha$ of the matter density is made of compact objects, $\rho_{\rm c}(t, \boldsymbol{x}) = \alpha\rho(t, \boldsymbol{x})$, while the rest is treated as diffuse matter. Since the microlensing optical depth associated with compact objects is small, any significant amplification is dominated by a single lens: the dominant lens.

density $\rho(t, \boldsymbol{x})$, there is a Poisson-distributed population of compact objects with mean density $\rho_{\rm c}(t, \boldsymbol{x}) \equiv \alpha\rho(t, \boldsymbol{x})$. We assume that $\alpha$ is constant in space and time.

**Dominant lens** We define the dominant lens as the one that would produce the strongest amplification $A$ if it were alone in the universe. Equivalently, it is the lens with the smallest reduced impact parameter $\beta/\theta_{\rm E}$, where $\beta$ is the angle between the unlensed source position and the lens position, and $\theta_{\rm E}$ its Einstein radius. We shall denote with a "d" subscript the quantities associated with the dominant lens, e.g., its redshift $z_{\rm d}$.

**Tidal perturbations** All the other inhomogeneities of the universe, which includes both astronomical structures and the non-dominant compact objects, are treated in the *tidal regime*. In the terminology of ref. [98], this means that apart from the immediate vicinity of the dominant lens, light propagates through a smooth spacetime geometry. This is equivalent to stating that the angle between multiple images produced by the dominant lens, which is on the order of its Einstein radius $\theta_{\rm E}$, is much smaller than the typical scale over which the gravitational field produced by the other inhomogeneities changes appreciably. This notably requires all the non-dominant compact objects to lie far from the line of sight. In practice, the tidal approximation means that non-dominant inhomogeneities only produce weak-lensing convergence and shear which perturb the behaviour of the dominant lens.

## 3.2 Lens equation and equivalent lens

We now discuss the lens equation associated with the set-up described in sec. 3.1. We then show that, with a suitable change of variables, it may be turned into the lens equation of a point lens with external shear.

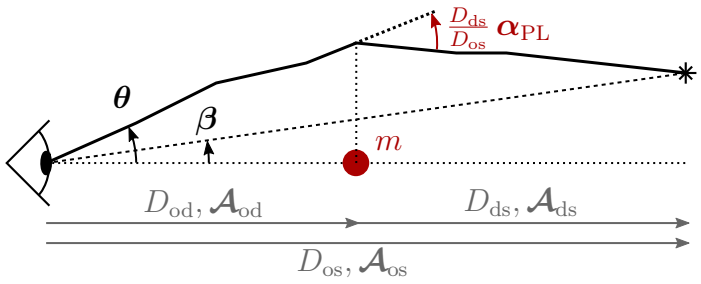


Figure 3.2: Schematic representation of the quantities involved in the lens equation (3.1). The total displacement $\boldsymbol{\theta} - \boldsymbol{\beta}$ is caused by the dominant point-like lens and the tidal distortions $\boldsymbol{\mathcal{A}}_{\rm od}, \boldsymbol{\mathcal{A}}_{\rm ds}, \boldsymbol{\mathcal{A}}_{\rm os}$.

### 3.2.1 Lens equation with tidal perturbations

The relevant quantities defined below are depicted in fig. 3.2. The line of sight is conventionally set as the direction in which the main lens is observed. With respect to that origin, we call $\boldsymbol{\beta}$ the unlensed position of the source. Throughout this article, "unlensed" will refer to the case where light would propagate in the reference FLRW model. We denote with $\boldsymbol{\theta}$ the observed position of an image of the source.

The lens equation is the relation between $\boldsymbol{\theta}$ and $\boldsymbol{\beta}$. For a dominant point lens with tidal perturbation along the line of sight, it takes the form [99, 100, 101, 102, 103, 104, 98, 105]

$$\boxed{\boldsymbol{\beta} = \boldsymbol{\mathcal{A}}_{\rm os}\,\boldsymbol{\theta} - \boldsymbol{\mathcal{A}}_{\rm ds}\,\boldsymbol{\alpha}_{\rm PL}(\boldsymbol{\mathcal{A}}_{\rm od}\boldsymbol{\theta})\ ,} \tag{3.1}$$

where we have introduced some notation. The heart of eq. (3.1) is the displacement angle $\boldsymbol{\alpha}_{\rm PL}(\boldsymbol{\theta})$ of the dominant (point-like) lens only. In the absence of other inhomogeneities, we would simply have $\boldsymbol{\beta} = \boldsymbol{\theta} - \boldsymbol{\alpha}_{\rm PL}(\boldsymbol{\theta})$. Its explicit expression is

$$\boldsymbol{\alpha}_{\rm PL}(\boldsymbol{\theta}) = \frac{\theta_{\rm E}^2\boldsymbol{\theta}}{|\boldsymbol{\theta}|^2} \equiv \frac{\theta_{\rm E}^2}{\boldsymbol{\theta}}\ , \tag{3.2}$$

where $\theta_{\rm E}$ is the unperturbed angular Einstein radius,

$$\theta_{\rm E}^2 \equiv \frac{4GmD_{\rm ds}}{D_{\rm od}D_{\rm os}} = \frac{4Gm(\chi_{\rm s}-\chi_{\rm d})}{a(\chi_{\rm d})\chi_{\rm d}\chi_{\rm s}}\ , \tag{3.3}$$

and $m$ the mass of the dominant lens.

The three quantities $\boldsymbol{\mathcal{A}}_{\rm od}, \boldsymbol{\mathcal{A}}_{\rm os}, \boldsymbol{\mathcal{A}}_{\rm ds}$ are $2\times 2$ distortion matrices which encode the tidal perturbations along the line of sight. They are defined as follows: *in the absence of the main lens*, for an observer at (a) and source at (b), the unlensed position $\boldsymbol{\beta}_{\rm ab}$ and lensed position $\boldsymbol{\theta}_{\rm ab}$ of the source are related by $\boldsymbol{\beta}_{\rm ab} = \boldsymbol{\mathcal{A}}_{\rm ab}\boldsymbol{\theta}_{\rm ab}$. Thus, in the absence of the dominant lens [$\boldsymbol{\alpha}_{\rm PL}(\boldsymbol{\theta}) = \mathbf{0}$] the lens equation would reduce to $\boldsymbol{\beta} = \boldsymbol{\mathcal{A}}_{\rm os}\boldsymbol{\theta}$, which corresponds to standard weak lensing [106]. The distortion matrices may be decomposed as

$$\boldsymbol{\mathcal{A}}_{\rm ab} = \mathbf{1} - \begin{array}{cc} \kappa_{\rm ab}+{\rm Re}(\gamma_{\rm ab}) & {\rm Im}(\gamma_{\rm ab})-\omega_{\rm ab} \\ {\rm Im}(\gamma_{\rm ab})+\omega_{\rm ab} & \kappa_{\rm ab}-{\rm Re}(\gamma_{\rm ab}) \end{array}\ , \qquad {\rm a,b} \in \{{\rm o,d,s}\}\ . \tag{3.4}$$

In this decomposition, $\kappa_{ab} \in \mathbb{R}$ represents the convergence that is be produced by the diffuse matter from (a) to (b); the symmetric trace-free part, encoded in $\gamma_{ab} \in \mathbb{C}$, represents the shear produced in the same interval; the anti-symmetric part $\omega_{ab} \in \mathbb{R}$ represents the solid rotation of images from (a) to (b).

In the following, we shall work *at first order in the shear*, $\gamma_{ab} \ll 1$. In that regime, it can be shown that the rotation is a second-order quantity $\omega \sim |\gamma|^2$ (see ref. [107], sec. 2.3.2); we shall thus neglect $\omega_{ab}$. However, as will be clearer in the very next paragraph, the convergence may reach values exceeding 10 %, hence we shall work non-perturbatively in $\kappa_{ab}$.

### 3.2.2 Physical origin of the convergence and shear

Let us now elaborate on the convergences $\kappa_{ab}$ and shears $\gamma_{ab}$ appearing in the distortion matrices that enter in the lens equation (3.1).

**Convergence is due to the diffuse matter** that is intercepted by the line of sight. More precisely, $\kappa_{ab}$ represents the excess (or deficit) of focusing from diffuse matter, with respect to the homogeneous FLRW reference, for a source located at (b) and observed from (a). Its explicit expression is

$$\kappa_{ab} \equiv 4\pi G \int_{\chi_a}^{\chi_b} \mathrm{d}\chi \, \frac{(\chi-\chi_a)(\chi_b-\chi)}{\chi_b-\chi_a} \, a^2(\chi) \, [(1-\alpha)\rho - \bar{\rho}] \tag{3.5}$$

$$= (1-\alpha)\bar{\kappa}_{ab} - \alpha\Delta_{ab} \, . \tag{3.6}$$

where $\Delta_{ab}$ and $\bar{\kappa}_{ab}$ are generalisations of the $\Delta_{os}$ and $\bar{\kappa}_{os}$ defined in eqs. (2.19) and (2.20),

$$\Delta_{ab} \equiv 4\pi G\bar{\rho}_0 \int_{\chi_a}^{\chi_b} \mathrm{d}\chi \, \frac{(\chi-\chi_a)(\chi_b-\chi)}{\chi_b-\chi_a} \, \frac{1}{a(\chi)} \, , \tag{3.7}$$

$$\bar{\kappa}_{ab} \equiv 4\pi G\bar{\rho}_0 \int_{\chi_a}^{\chi_b} \mathrm{d}\chi \, \frac{(\chi-\chi_a)(\chi_b-\chi)}{\chi_b-\chi_a} \, \frac{\delta(\chi)}{a(\chi)} \, . \tag{3.8}$$

The first term in eq. (3.6) is quite intuitive; since the fraction of diffuse matter is $1-\alpha$, any excess $\bar{\kappa}_{ab}$ in total projected density translates into $(1-\alpha)\bar{\kappa}_{ab}$ from its diffuse component. The second term is more subtle; it encodes the deficit of diffuse matter, relative to FLRW, that occurs as one turns a fraction $\alpha$ of it into compact matter. In the extreme case $\alpha = 1$, there is no diffuse matter at all, which implies a significant focusing deficit, $\kappa_{ab} = -\Delta_{ab}$, with respect to FLRW – this is Zel'dovich's empty-beam case [95]. The presence of $\Delta_{ab}$ in $\kappa_{ab}$ is the reason why the convergence can reach relatively large values and should not be treated at linear order. Note finally that eqs. (2.18) and (3.6) imply the following relation between convergences and optical depth: $\kappa_{os} = \bar{\kappa}_{os} - \tau$.

**Shear is due to both diffuse and compact matter** unlike convergence. This is because shear is associated with long-range tidal forces generated by any matter lump. For a source located at (b) and observed from (a), we may decompose the total shear as

$$\gamma_{\mathrm{ab}} = \bar{\gamma}_{\mathrm{ab}} + s_{\mathrm{ab}} \ . \tag{3.9}$$

In eq. (3.9), $\bar{\gamma}_{\mathrm{ab}}$ is the *macroshear* associated with the smooth density contrast, that is, the shear that would be produced on a beam of light in the absence of any compact object near the line of sight. Its formal expression is [108]

$$\bar{\gamma}_{\mathrm{ab}} = -4\pi G\bar{\rho}_0 \int_{\chi_{\mathrm{a}}}^{\chi_{\mathrm{b}}} \mathrm{d}\chi \, \frac{(\chi-\chi_{\mathrm{a}})(\chi_{\mathrm{b}}-\chi)}{\chi_{\mathrm{b}}-\chi_{\mathrm{a}}} \int_{\mathbb{R}^2} \frac{\mathrm{d}^2\boldsymbol{r}}{\pi r^2} \, \frac{\delta(\chi,\boldsymbol{r})}{a(\chi)} \, \mathrm{e}^{2\mathrm{i}\varphi} \ , \tag{3.10}$$

where $\boldsymbol{r} = r(\cos\varphi, \sin\varphi)$ denotes the physical transverse position of a point, orthogonally to the line of sight, $\mathrm{d}^2\boldsymbol{r} = r\mathrm{d}r\mathrm{d}\varphi$. Specifically, $r$ is the distance between a point and the line of sight and $\varphi$ is its polar angle about that axis.

The second term of eq. (3.9), $s_{\mathrm{ab}}$, is the *microshear* produced by compact objects in the vicinity of the line of sight, except the dominant lens. If the region between (a) and (b) contains $N$ point-like lenses labelled with $\ell$, then the microshear reads [105]

$$s_{\mathrm{ab}} = -4\pi G \sum_{\ell=1}^{N} \frac{(\chi_\ell-\chi_{\mathrm{a}})(\chi_{\mathrm{b}}-\chi_\ell)}{\chi_{\mathrm{b}}-\chi_{\mathrm{a}}} \, \frac{a(\chi_\ell)m_\ell}{\pi r_\ell^2} \, \mathrm{e}^{2\mathrm{i}\varphi_\ell} \ , \tag{3.11}$$

where $m_\ell$ is the mass of lens $\ell$, $\chi_\ell$ its comoving distance from the observer, $r_\ell$ its physical distance from the optical axis and $\varphi_\ell$ its polar angle about it. Note that eq. (3.10) is nothing but the continuous limit of eq. (3.11).

The careful reader may have noticed that the macroshear $\bar{\gamma}_{\mathrm{ab}}$ does not come with any prefactor $(1-\alpha)$. Such a prefactor could be expected indeed, to avoid double-counting the shear of compact matter, which should be encoded in $s_{\mathrm{ab}}$ already. The reason is that, in the following, we shall compute $s_{\mathrm{ab}}$ as if the compact objects were randomly distributed transversely to the line of sight. Hence, $s_{\mathrm{ab}}$ will not account for the large-scale clustering of those objects. Because they follow the total matter density contrast $\delta(t,\boldsymbol{x})$ on large scales, their contribution to cosmic shear is essentially the same as if they were replaced by diffuse matter. Therefore, $\bar{\gamma}_{\mathrm{ab}}$ is unchanged under changes of the compact matter fraction $\alpha$. Increasing $\alpha$ only produces more shear via $s_{\mathrm{ab}}$.

### 3.2.3 Equivalent lens

The lens equation (3.1) contains a priori nine real parameters besides the dominant lens's Einstein radius: the three convergences and the six shear components. But only a few specific combinations of those parameters turn out to be relevant to the problem of amplification probabilities. Multiplying eq. (3.1) to the left with

$(1-\kappa_{\rm od})(1-\kappa_{\rm os})^{-1}(1-\kappa_{\rm ds})\boldsymbol{\mathcal{A}}_{\rm ds}^{-1}$ and working at first order in the shears, we find the *equivalent lens equation*

$$\boxed{\tilde{\boldsymbol{\beta}} = (1-\boldsymbol{\Gamma})\,\tilde{\boldsymbol{\theta}} - \frac{\tilde{\theta}_{\rm E}^2}{\tilde{\boldsymbol{\theta}}}\ ,} \tag{3.12}$$

whose new variables are

$$\tilde{\boldsymbol{\beta}} \equiv \frac{(1-\kappa_{\rm od})(1-\kappa_{\rm ds})}{1-\kappa_{\rm os}}\,\boldsymbol{\mathcal{A}}_{\rm ds}^{-1}\boldsymbol{\beta}\ , \tag{3.13}$$

$$\tilde{\boldsymbol{\theta}} \equiv \boldsymbol{\mathcal{A}}_{\rm od}\boldsymbol{\theta}\ , \tag{3.14}$$

and the new parameters read

$$\tilde{\theta}_{\rm E} \equiv \sqrt{\frac{(1-\kappa_{\rm od})(1-\kappa_{\rm ds})}{1-\kappa_{\rm os}}}\,\theta_{\rm E}\ , \tag{3.15}$$

$$\boldsymbol{\Gamma} \equiv \begin{matrix} {\rm Re}(\gamma) & {\rm Im}(\gamma) \\ {\rm Im}(\gamma) & -{\rm Re}(\gamma) \end{matrix}\ , \qquad \gamma \equiv \frac{\gamma_{\rm os}}{1-\kappa_{\rm os}} - \frac{\gamma_{\rm od}}{1-\kappa_{\rm od}} - \frac{\gamma_{\rm ds}}{1-\kappa_{\rm ds}}\ . \tag{3.16}$$

In other words, under the linear change of variables $(\boldsymbol{\beta},\boldsymbol{\theta}) \mapsto (\tilde{\boldsymbol{\beta}},\tilde{\boldsymbol{\theta}})$, our initial problem of a point lens with generic tidal perturbations has turned into the much simpler eq. (3.12), which describes a point mass with an external shear[2] $\gamma$ in the same plane. This equivalent problem has been well studied since the 1980s [80, 83, 109].

## 3.3 Amplification cross section

Let us use the equivalent lens model (3.12) to derive the amplification cross section. We define the *differential amplification cross section* $\Omega(A)$ so that $\Omega(A){\rm d}A$ is the angular area (solid angle) of the region of the sky where the amplification is between $A$ and $A+{\rm d}A$.

### 3.3.1 For the equivalent lens

We first work in the twiddled world described by eq. (3.12). If the effective shear $\gamma$ were zero, then the problem would reduce to a single point lens whose constant-amplification contours are circles, with radius $\tilde{\beta}_0(\tilde{A}) = \tilde{\theta}_{\rm E}\,[2\tilde{A}/(\tilde{A}^2-1)^{1/2}-2]^{1/2}$. The cross section would thus read, in this simple case,

$$\tilde{\Omega}_0(\tilde{A}) = 2\pi\tilde{\beta}_0(\tilde{A})\ \frac{{\rm d}\tilde{\beta}_0}{{\rm d}\tilde{A}}\ = \frac{2\pi\tilde{\theta}_{\rm E}^2}{(\tilde{A}^2-1)^{3/2}}\ . \tag{3.17}$$

The problem is more involved in the presence of shear. In that case the source plane displays two distinct regions separated by an astroid-shaped caustic[3] (see right

[2]This particular shear combination $\gamma$ is different from the line-of-sight shear combination $\gamma_{\rm LOS} = \gamma_{\rm os}+\gamma_{\rm od}-\gamma_{\rm ds}$ that was isolated in ref. [105], even in the absence of the convergences.

[3]For a given lensing system, *caustics* are the set of source positions $\boldsymbol{\beta}$ whose amplification is infinite. Hence, critical curves are the images of caustics by the lensing system.

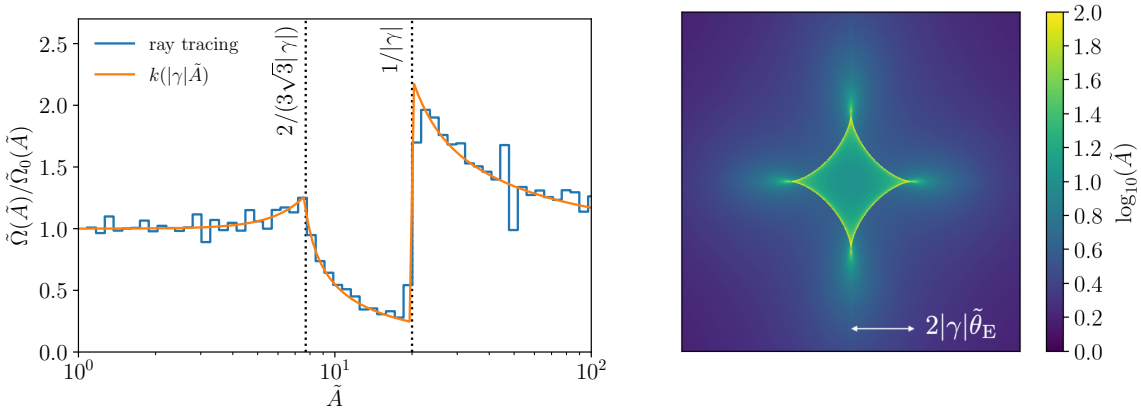


Figure 3.3: Properties of the equivalent point lens with external shear. *Left panel*: Ratio of the amplification cross section $\tilde{\Omega}(\tilde{A})$ in the presence of shear (here $\gamma = 0.05$) with the no-shear case $\tilde{\Omega}_0(\tilde{A})$ (3.17). The solid-line histogram shows results from ray tracing, while the dashed line shows the analytical fit $k(|\gamma|\tilde{A})$ of eq. (3.19) as proposed in ref. [109]. *Right panel*: Amplification map $\tilde{A}(\tilde{\boldsymbol{\beta}})$. The astroid-shaped caustic has a size $2|\gamma|\tilde{\theta}_\mathrm{E}$; inside the astroid a source has four images, outside it has two images, and exactly on it it has three images among which one is infinitely amplified.

panel of fig. 3.3). Outside the caustic a source has two images while inside it has four images. The shear $\gamma$ fixes the size and orientation of the astroid. To the best of our knowledge there is no analytic expression for the amplification $\tilde{A}(\tilde{\boldsymbol{\beta}})$ or its contours in that case. Nevertheless, Nityanda & Ostriker [80] noticed the remarkable fact that for low values of the shear $|\gamma|$, corrections the the amplification cross section should only depend on the product $|\gamma|A$. More than a decade later, Kofman et al. [109] further pushed this idea by writing

$$\tilde{\Omega}(\tilde{A}) = \tilde{\Omega}_0(\tilde{A})\, k(|\gamma|\tilde{A}) \ , \tag{3.18}$$

where $\tilde{\Omega}_0(\tilde{A})$ is the no-shear cross section of eq. (3.17), while $k$ is a function fitted from numerical simulations,[4]

$$k(x) = \begin{cases} 1 + 7.7\, x^{3.5} & x \leq \dfrac{2}{3\sqrt{3}} \ , \\ \dfrac{0.17}{(x-0.33)^{1/2}} + \dfrac{0.023}{x-0.33} & \dfrac{2}{3\sqrt{3}} \leq x \leq 1 \ , \\ 1 + \dfrac{0.85}{x} + \dfrac{0.37}{x^5} & x \geq 1 \ . \end{cases} \tag{3.19}$$

For the sake of completeness, we have reproduced in fig. 3.3 the comparison between numerical ray tracing and Kofman et al.'s result (3.18) for $\gamma = 0.05$. The simulation uses inverse ray tracing with a simple adaptive mesh refinement, see ref. [89] for details. Agreement is excellent.

[4] In ref. [109], that function was denoted with $\varphi$. We changed the notation so as to avoid confusion with the polar angle of subsec. 3.2.2, and adopted "$k$" instead, in honour of Lev Kofman.

### 3.3.2 Back to the original problem

We now translate the results of the twiddled world in terms of $\Omega(A)$. The first step is to express $\tilde{A}$ in terms of $A$. At first order in the shear, we find

$$\tilde{A} \equiv \frac{\mathrm{d}^2\tilde{\boldsymbol{\theta}}}{\mathrm{d}^2\tilde{\boldsymbol{\beta}}} = \frac{(1-\kappa_{\rm os})^2}{(1-\kappa_{\rm od})^2(1-\kappa_{\rm ds})^2}\,\frac{\det\boldsymbol{\mathcal{A}}_{\rm od}}{\det\boldsymbol{\mathcal{A}}_{\rm ds}^{-1}}\,\frac{\mathrm{d}^2\boldsymbol{\theta}}{\mathrm{d}^2\boldsymbol{\beta}} = (1-\kappa_{\rm os})^2 A\ . \tag{3.20}$$

The conversion of $\tilde{\Omega}$ into $\Omega$ must take two aspects into account. On the one hand, since those are differential cross sections, their relation involves the Jacobian $|\mathrm{d}\tilde{A}/\mathrm{d}A|$, just like when one changes variables in a probability density function, for example. Second, since $\tilde{\Omega}$ is a cross section in the twiddled source plane, it is expressed in the twiddled units $[\tilde{\beta}]^2$, which differ from the units $[\beta]^2$ of the original source plane. Taking both aspects into account yields

$$\Omega(A)\,\mathrm{d}A = \frac{\mathrm{d}^2\boldsymbol{\beta}}{\mathrm{d}^2\tilde{\boldsymbol{\beta}}} \times \tilde{\Omega}(\tilde{A})\,\mathrm{d}\tilde{A}\ . \tag{3.21}$$

Substituting eqs. (3.13), (3.18) and (3.20) into eq. (3.21), and still working at first order in the shear, we find the following elegant expression for the cross section,

$$\boxed{\Omega(A) = 2\pi\vartheta_{\rm E}^2\,k\left(\frac{|\gamma|A}{A_{\rm min}}\right)\frac{A_{\rm min}^2}{(A^2-A_{\rm min}^2)^{3/2}}\ ,} \tag{3.22}$$

where $A_{\rm min} \equiv (1-\kappa_{\rm os})^{-2}$ is the minimal amplification in this setup, i.e. the amplification that would be observed if the dominant lens were infinitely far from the line of sight, so that only the weak-lensing convergence is at play. It is implicit that $\Omega(A < A_{\rm min}) = 0$. Besides, we have introduced $\vartheta_{\rm E}$ such that

$$\vartheta_{\rm E}^2 \equiv \frac{(1-\kappa_{\rm ds})\,\theta_{\rm E}^2}{(1-\kappa_{\rm od})(1-\kappa_{\rm os})} = \frac{4Gm(1-\kappa_{\rm ds})D_{\rm ds}}{(1-\kappa_{\rm od})D_{\rm od}(1-\kappa_{\rm os})D_{\rm os}}\ . \tag{3.23}$$

Physically, $\vartheta_{\rm E}$ represents the the lensed Einstein radius, i.e. the size of the Einstein ring that would be observed if the source were perfectly aligned with the dominant lens in the presence of the external convergences; this can be checked by setting $\boldsymbol{\beta} = \mathbf{0}$ in eq. (3.1).

Summarising, the convergence due to diffuse matter has two distinct effect on $\Omega(A)$: (i) they rescale amplifications according to $A \to A/A_{\rm min} = (1-\kappa_{\rm os})^2 A$, thereby fixing the minimum amplification accessible to the system; (ii) they rescale the dominant lens's Einstein radius as $\theta_{\rm E} \to \vartheta_{\rm E}$, thereby changing the cross section directly. The shear, due to both diffuse and compact matter, affects $\Omega(A)$ via Kofman et al.'s function $k(|\gamma|A/A_{\rm min})$ only.

CHAPTER

# FOUR

# AMPLIFICATION PROBABILITIES

In the previous section, we have derived the amplification cross section $\Omega(A)$ for a single point lens with perturbations (3.22). We shall now turn this result into a PDF for the amplification, $p(A)$, using the statistical properties of the dominant lens and its perturbations.

## 4.1 Amplification probability for a single lens

In realistic scenarios where the mass of the compact objects is small (e.g. comparable to a solar mass), then the typical angle separating two such objects is much smaller than the angular scales over which $\bar{\kappa}, \bar{\gamma}, \tau$ are changing appreciably. Thus, we may consider a "mesoscopic" cone with half angle $\Theta$ at the observer which contains a large number of compact objects, but across which the macroscopic quantities $\bar{\kappa}, \bar{\gamma}, \tau$ are constant (see fig. 4.1). Since those empirically show significant changes on the arcmin scale, we have $\Theta \ll 1$.

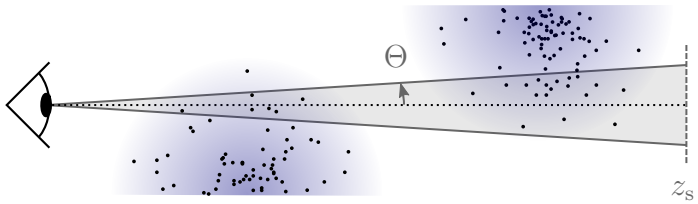


Figure 4.1: Mesoscopic cone with half angle $\Theta$ at the observer, containing a large number of compact objects, but across which the macroscopic quantities $\tau, \bar{\kappa}, \bar{\gamma}$ can be considered constant.

The first step of our calculation consists in expressing the PDF $p_1(A)$ of the amplification due to one dominant lens in the mesoscopic cone. If all the parameters entering the amplification cross section (3.22) were fixed, then we would have by definition $p_1(A) = \Omega(A)/(\pi\Theta^2)$. But since the properties of the main lens – namely its mass $m$ and comoving distance $\chi$ from the observer – and the microshear $s = \gamma - \bar{\gamma}$ vary a lot across the mesoscopic cone, we must marginalise over their statistical

distribution,

$$p_1(A) = \frac{1}{\pi\Theta^2} \int \mathrm{d}m\, \mathrm{d}\chi\, \mathrm{d}^2 s\; p(m,\chi,s)\, \Omega(A; m, \chi, |\bar{\gamma} + s|) \;, \tag{4.1}$$

where $\Omega$ depends on $m$ via the Einstein radius of the dominant lens, $\theta_{\mathrm{E}}^2 \propto m$, and on $\chi$ via $\theta_{\mathrm{E}}$ and the (od), (ds) convergences and shears. We did not explicitly include the fixed macroscopic parameters $\tau, \bar{\kappa}_{\mathrm{os}}, \bar{\gamma}_{\mathrm{os}}$ to alleviate notation.

### 4.1.1 Approximations

In order to model the joint distribution $p(m,\chi,s)$, we make the following assumptions:

1. The mass $m$ of the dominant lens is uncorrelated with the other parameters. Since $\Omega \propto m$, this implies that we may simply replace $m$ by its average value $\langle m \rangle$ in the remainder of this calculation.

2. Compact objects are randomly distributed in space and their *comoving* number density $n_{\mathrm{c}}$ is constant within the mesoscopic cone. This implies, in particular, that $p(\chi) = 3\chi^2/\chi_{\mathrm{s}}^3$.

Besides, in order to simplify the evaluation of the various convergences and shears involved in $\Omega(A)$, we shall adopt the following *mean-field approximation*:

$$\bar{\kappa}_{\mathrm{ab}} \approx \left(\frac{\chi_{\mathrm{b}} - \chi_{\mathrm{a}}}{\chi_{\mathrm{s}}}\right)^2 \bar{\kappa}_{\mathrm{os}} \;, \qquad \bar{\gamma}_{\mathrm{ab}} \approx \left(\frac{\chi_{\mathrm{b}} - \chi_{\mathrm{a}}}{\chi_{\mathrm{s}}}\right)^2 \bar{\gamma}_{\mathrm{os}} \;. \tag{4.2}$$

The intuition behind this approximation appears by examining the integrals (3.8) and (3.10) defining $\bar{\kappa}_{\mathrm{ab}}$ and $\bar{\gamma}_{\mathrm{ab}}$. Consider all the possible lines of sight with the same fixed $\bar{\kappa}_{\mathrm{os}}$, $\bar{\gamma}_{\mathrm{os}}$. They are in principle quite diverse, because the matter density contrast $\delta$ may display significant variations along them, and hence they may have a variety of $\bar{\kappa}_{\mathrm{od}}, \bar{\kappa}_{\mathrm{ds}}, \bar{\gamma}_{\mathrm{od}}, \bar{\gamma}_{\mathrm{ds}}$. However, on average all the elements $\mathrm{d}\chi$ along the line of sight should conspire so as to produce the required $\bar{\kappa}_{\mathrm{os}}, \bar{\gamma}_{\mathrm{os}}$. If we neglect the effect of dark energy on structure formation, we know that $\delta \propto a$, which motivates us to consider that the mean-field contribution of $\delta(\chi)/a(\chi)$ to $\bar{\kappa}_{\mathrm{ab}}, \bar{\gamma}_{\mathrm{ab}}$ is independent of $\chi$. As the latter is taken off the integrals over $\chi$, eqs. (3.8) and (3.10) imply

$$\bar{\kappa}_{\mathrm{ab}}, \bar{\gamma}_{\mathrm{ab}} \propto \int_{\chi_{\mathrm{a}}}^{\chi_{\mathrm{b}}} \mathrm{d}\chi\; \frac{(\chi - \chi_{\mathrm{a}})(\chi_{\mathrm{b}} - \chi)}{\chi_{\mathrm{b}} - \chi_{\mathrm{a}}} \propto (\chi_{\mathrm{b}} - \chi_{\mathrm{a}})^2 \;, \tag{4.3}$$

whence eq. (4.2). We shall also apply a similar rule to the full convergence $\kappa_{\mathrm{ab}}$.

The difficult step then consists in determining the distribution for the microshear, and evaluating its consequences on $p_1(A)$.

### 4.1.2 Distribution of the microshear

The statistics of the shear caused by a random distribution of point masses has been, in fact, a well-know problem for a long time. It was first considered for masses placed in the same plane by Nityananda & Ostriker [80], using one of the methods exposed in the famous review [110] by Chandrasekhar in 1943 on statistical problems in astrophysics. However, the very last step of the calculation was only performed three years later by Schneider [111]. The result was then generalised to any lens profile by Lee & Spergel [84] and finally to multiple lens planes in Lee et al. [85].

In the case that we are interested in here, if the dominant lens is fixed at a comoving distance $\chi$ from the observer, then the reduced microshear $s = s_{\rm os}/(1-\kappa_{\rm os}) - s_{\rm od}/(1-\kappa_{\rm od}) - s_{\rm ds}/(1-\kappa_{\rm ds})$ caused by the other compact objects has an amplitude $S \equiv |s|$ distributed as

$$p(S;\chi)\,\mathrm{d}S = \frac{f(\chi)\tau S\,\mathrm{d}S}{[f^2(\chi)\tau^2 + S^2]^{3/2}}\ , \qquad P(S;\chi) = \left(1 - \frac{S^2}{f^2(\chi)\tau^2}\right)^{-1/2}\ . \tag{4.4}$$

Equation (4.4) is controlled by an effective optical depth $f\tau$, with[1]

$$f(\chi;\chi_{\rm s},\kappa_{\rm os}) \equiv \frac{\int_0^{\chi}\frac{\mathrm{d}\chi'}{a(\chi')}\ \frac{\chi'(\chi_{\rm s}-\chi')}{(1-\kappa_{\rm os})\chi_{\rm s}} - \frac{\chi'(\chi-\chi')}{[1-\kappa_{\rm od}(\chi)]\chi}\ + \int_{\chi}^{\chi_{\rm s}}\frac{\mathrm{d}\chi'}{a(\chi')}\ \frac{\chi'(\chi_{\rm s}-\chi')}{(1-\kappa_{\rm os})\chi_{\rm s}} - \frac{(\chi'-\chi)(\chi_{\rm s}-\chi')}{[1-\kappa_{\rm ds}(\chi)](\chi_{\rm s}-\chi)}}{\int_0^{\chi_{\rm s}}\frac{\mathrm{d}\chi'}{a(\chi')}\ \frac{\chi'(\chi_{\rm s}-\chi')}{\chi_{\rm s}}} \tag{4.5}$$

$$\approx \frac{1}{(1-\kappa_{\rm os})^{7/4}}\,\frac{2\chi}{\chi_{\rm s}}\ \left(1 - \frac{\chi}{\chi_{\rm s}}\right)\ . \tag{4.6}$$

The last approximation holds when the scale factor can be considered constant in the integrals (i.e. for $\chi_{\rm s} \to 0$) and in the mean-field approximation for $\kappa_{\rm od}, \kappa_{\rm ds}$. The $(1-\kappa_{\rm os})^{-7/4}$ is empirical. The shape of the function $f(\chi)$ for various values of the source redshift and external convergence $\kappa_{\rm os}$ is depicted in fig. 4.2. Since the derivation of eq. (4.4) in ref. [85] uses different conventions and notation, we propose a full derivation in chapter B for completeness.

Let us finally point out that eq. (4.4) is actually an approximation where high values of $S$ are overestimated. Indeed, the compact objects responsible for the microshear are, by definition, non-dominant lenses. As such, their individual shear should not exceed the one that would be produced by the dominant lens if it were alone. So in principle $p(S)$ should also depend on, e.g., the impact parameter of the dominant lens $\beta_{\rm d}$, which would set an upper bound on $S$. This upper bound would go to infinity as $\beta_{\rm d} \to 0$, i.e. for large values of the amplification. Albeit more rigorous, these considerations would significantly complicate the treatment of the problem. We thus choose to ignore them, with the perspective of placing an upper bound on the effect of the microshear on $p(A)$.

[1] We shall often omit the fixed variables $\chi_{\rm s}, \kappa_{\rm os}$ and just write $f(\chi)$ instead of $f(\chi;\chi_{\rm s},\kappa_{\rm os})$, just like we do not specify the dependence of $\tau$ on those parameters.

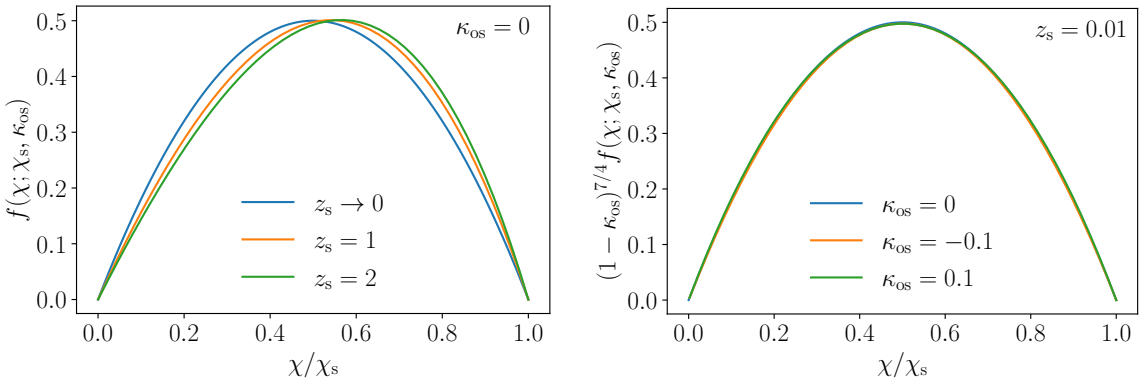


Figure 4.2: Factor $f(\chi; \chi_s, \kappa_s)$ defined in eq. (4.5) as a function of the ratio $\chi/\chi_s$. *Left*: showing the dependence on the source redshift, by comparing $z_s \to 0$ to $z_s = 1, 2$ for $\kappa_{os} = \kappa_{od} = \kappa_{ds} = 0$. *Right*: showing the dependence in $\kappa_{os}$ in the mean-field approximation, for $z_s \ll 1$.

### 4.1.3 The macroshear is negligible

The total shear $\gamma = \bar{\gamma} + s$ is the sum of the microshear $s$ discussed above with the macroshear $\bar{\gamma}$ due to the large-scale structure. While the distribution of microshear has a heavy tail, $\text{Prob}(> S) \propto S^{-1}$, it turns out that the macroshear does not share this property, because the structures producing it are more diffuse. As shown in sec. A.2, the conditional PDF of the macroshear at fixed convergence is surprisingly well fit by a two-dimensional Gaussian distribution, which therefore predicts very few high values for the macroshear.

Note that $s$ must be compared with $\bar{\gamma} \equiv \bar{\gamma}_{os}/(1-\kappa_{os}) - \bar{\gamma}_{od}/(1-\kappa_{od}) - \bar{\gamma}_{ds}/(1-\kappa_{ds})$ rather than with $\bar{\gamma}_{os}$ alone. The difficulty is that ray tracing in numerical simulations is performed for a unique observer at present time; they allow one to compute $\bar{\gamma}_{os}, \bar{\gamma}_{od}$, but not $\bar{\gamma}_{ds}$. To circumvent this issue we apply again the mean-field approximation introduced in subsec. 4.1.1, which yields

$$\bar{\gamma} \approx f\, \bar{\gamma}_{os} \ , \tag{4.7}$$

with $f$ defined in eq. (4.5). It is not surprising to find here the same correction factor $f$ as for the effective optical depth of microshear: both have the same origin. Within that approximation, the PDF of $|\bar{\gamma}|$ is obtained from eq. (A.10) by simple rescaling.

Figure 4.3 compares the distributions of the microshear and macroshear amplitudes, for a source at $z_s = 0.95$, a dominant lens at $z = 0.5$, and for a line of sight with $\bar{\kappa}_{os} = 0$ for simplicity. Three values for the fraction of compact matter are considered, $\alpha = 0.83, 0.1, 0.01$ – the first case would correspond to the whole DM being made of compact objects. Those values correspond, respectively, to the effective optical depths $f\tau = 2.5 \times 10^{-2}, 3.0 \times 10^{-3}, 3.0 \times 10^{-4}$. Although the macroshear is generally not negligible compared to the microshear, especially when $\alpha$ is small, it is unable to produce large amplitudes. But large values of the shear are necessary

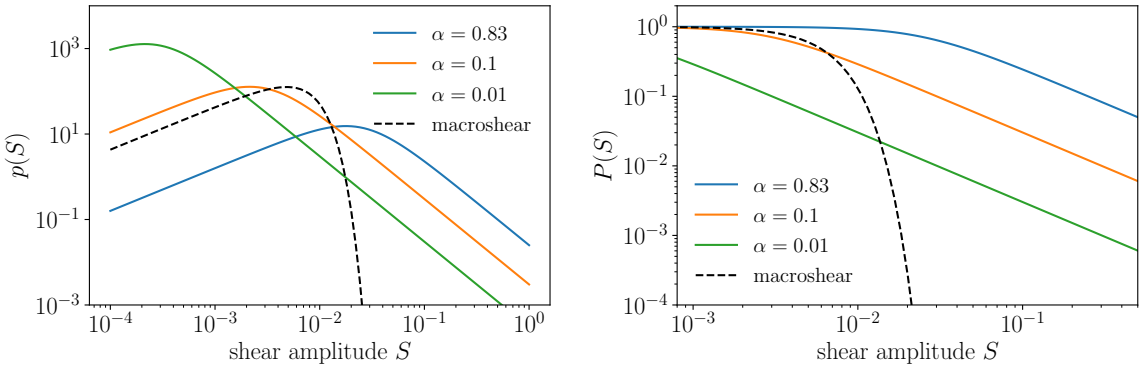


Figure 4.3: Distributions of the amplitude of microshear (solid lines), if the source located at $z_\mathrm{s} = 0.95$ and the dominant lens at $z = 0.5$. The left panel shows PDFs while the right panel shows CDFs. Three values for the fraction of compact matter are considered, $\alpha = 0.83, 0.1, 0.01$. Dashed lines indicate the distributions of the amplitude of the macroshear $|\bar{\gamma}| \approx f|\gamma_\mathrm{os}|$, for lines of sight with $\bar{\kappa}_\mathrm{os} = 0$.

to produce changes in $\Omega(A)$ at reasonable amplifications, $A < 10$ (see sec. 3.3). In the situation illustrated here, $|\bar{\gamma}| < 3\,\%$ which would only affect $\Omega(A \gtrsim 13)$. Summarising, when macroshear is comparable to, or even larger than, microshear, then both have a negligible impact on the amplification statistics anyway. We shall thus neglect macroshear from now on, and replace $\Omega(A; m, \chi, |\bar{\gamma}+s|)$ with $\Omega(A; m, \chi, S)$ in eq. (4.1).

### 4.1.4 Final expression of $p_1(A)$

Substituting, in eq. (4.1), the probability density $p(m, s, \chi) = p(m)\, p(S; \chi)\, p(\chi)$ – where $p(S; \chi)$ is given by eq. (4.4) – and the expression (3.22) of $\Omega(A; m, \chi, S)$, and performing the change of variable $S \mapsto y \equiv S/f\tau$, we find

$$p_1(A) = \frac{2}{\Theta^2} \frac{A_\mathrm{min}^2}{(A^2 - A_\mathrm{min}^2)^{3/2}} \int_0^{\chi_\mathrm{s}} \mathrm{d}\chi\, p(\chi) \Big\langle \vartheta_\mathrm{E}^2(\chi) \Big\rangle_m K\left(\frac{f(\chi)\tau A}{A_\mathrm{min}}\right) , \tag{4.8}$$

where $\langle \ldots \rangle_m$ denotes an average over the mass $m$ of the dominant lens, and[2]

$$K(x) \equiv \int_0^\infty \mathrm{d}y\, \frac{y\, k(xy)}{(1+y^2)^{3/2}} \approx 1 - 0.81\, x^2(1-3x) \left(1 + \frac{3}{2}\, x^{3/2}\right)^{-8/3} . \tag{4.9}$$

The last step of the simplification of $p_1(A)$ consists in fully isolating the effect of the (micro)shear. For that purpose, we may multiply and divide eq. (4.8) with the average value of the weakly lensed squared Einstein radius,

$$\Big\langle \vartheta_\mathrm{E}^2 \Big\rangle \equiv \int_0^{\chi_\mathrm{s}} \mathrm{d}\chi\, p(\chi) \Big\langle \vartheta_\mathrm{E}^2(\chi) \Big\rangle_m = \frac{4G\,\langle m \rangle}{(1-\kappa_\mathrm{os})\chi_\mathrm{s}} \int_0^{\chi_\mathrm{s}} \frac{\mathrm{d}\chi}{a(\chi)}\, \frac{1-\kappa_\mathrm{ds}(\chi)}{1-\kappa_\mathrm{od}(\chi)}\, \chi(\chi_\mathrm{s} - \chi) , \tag{4.10}$$

[2] In ref. [109], the function $K(x)$ is denoted by $f_1(x)$. The approximation in the second equality of eq. (4.9) was proposed in ref. [109] and its comparison with the exact result is shown in fig. 4 therein.

to get

$$\boxed{p_1(A) = \frac{2\,\langle\vartheta_{\rm E}^2\rangle}{\Theta^2}\,\frac{A_{\rm min}^2}{(A^2-A_{\rm min}^2)^{3/2}}\,\mathcal{K}\quad\frac{\tau}{(1-\kappa_{\rm os})^{7/4}}\frac{A}{A_{\rm min}}\quad,} \tag{4.11}$$

with the last function that we shall define in this derivation:

$$\mathcal{K}(x) \equiv \frac{\int_0^{\chi_{\rm s}}\frac{{\rm d}\chi}{a(\chi)}\,\frac{1-\kappa_{\rm ds}(\chi)}{1-\kappa_{\rm od}(\chi)}\,\chi(\chi_{\rm s}-\chi)\,K[(1-\kappa_{\rm os})^{7/4}f(\chi)x]}{\int_0^{\chi_{\rm s}}\frac{{\rm d}\chi}{a(\chi)}\,\frac{1-\kappa_{\rm ds}(\chi)}{1-\kappa_{\rm od}(\chi)}\,\chi(\chi_{\rm s}-\chi)}\,. \tag{4.12}$$

The presence of the $(1-\kappa_{\rm os})^{7/4}$ factor in the argument of $K$ in eq. (4.12) is designed to absorb the empirical dependence on $\kappa_{\rm os}$ in $f$, and hence make $\mathcal{K}(x)$ practically insensitive to $\kappa_{\rm os}$.

The function $\mathcal{K}(x)$ defined in eq. (4.12) fully encapsulates the effect of the microshear. In principle, this function depends on the source redshift $z_{\rm s}$ via $\chi_{\rm s}=\chi(z_{\rm s})$, and on the macrostructure along the line of sight via $\kappa_{\rm os},\kappa_{\rm od},\kappa_{\rm ds}$. In practice, however, fig. 4.4 shows that $\mathcal{K}(x)$ is quite insensitive to those parameters. Such an empirical independence of $\mathcal{K}(x)$ in its external parameters encourages us to look for a simple and universal fitting function for it. We find that

$$\mathcal{K}(x) = 1-0.254\,x^{2.33}\,(1-1.30\,x)\quad\left(1+\frac{5}{4}\quad\frac{x}{1.83}\right)^{5/4\quad-3.43} \tag{4.13}$$

provides an excellent fit, with an accuracy of a few parts in $10^4$ (see fig. 4.4).

The main conclusion of this subsection is that, to an excellent level of precision, the effect of the microshear on $p_1(A)$ mostly depends on the optical depth $\tau$. It reduces by about 1 % the probability of amplifications $A\sim 1/\tau$, and enhances larger ones ($A\sim 10/\tau$) by about 15 %. Since we are considering low values for the optical depths, we can already anticipate that the net impact of shear on reasonable amplifications will be negligible.

## 4.2 From one lens to many: the strongest-perturbed-lens prescription

Now that we dispose of an accurate expression for the amplification PDF $p_1(A)$ of a single perturbed lens within a mesoscopic cone (fig. 4.1), we can generalise it to a large number $N\gg 1$ of such lenses. For that purpose, we shall adapt the strongest-lens prescription of sec. 2.2, which consists in assuming that the total amplification $A$ produced by the $N$ perturbed lenses in the cone, is well-approximated by the amplification due to the strongest of them. Importantly, that is *not* to say that we are entirely neglecting the effect of the other lenses, because it is already encoded in the convergence and microshear corrections. As such, the strongest-perturbed-lens approach must be understood as a statistical prescription that is physically consistent with the set of approximations that we have considered so far.

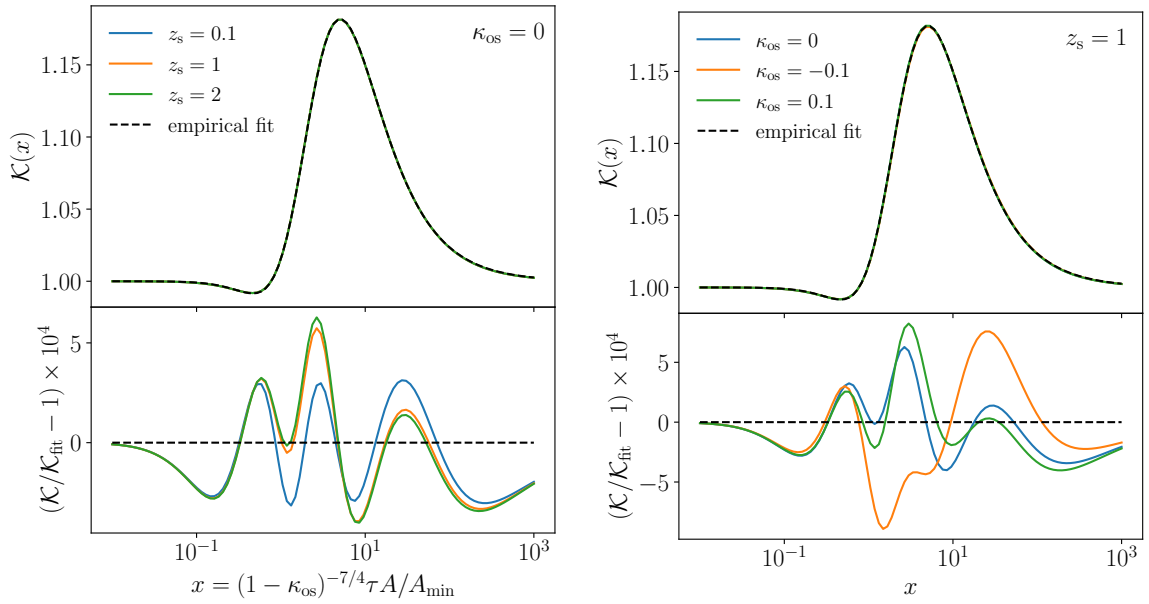


Figure 4.4: Integral $\mathcal{K}(x)$ defined in eq. (4.12) as a function of $x = (1-\kappa_{os})^{-7/4}\tau A/A_{min}$, which encapsulates all the microshear corrections to $p_1(A)$, with the empirical fitting function proposed in eq. (4.13). *Left*: Checking the dependence in $\chi_s = \chi(z_s)$, for a fixed $\kappa_{os} = 0$. *Right*: Checking the dependence in $\kappa_{os}$ for $z_s = 1$. The bottom panels show the relative accuracy of the empirical fit. We can see that $\mathcal{K}$ is mostly insensitive to both $z_s$ and $\kappa_{os}$, and that the fitting function is an excellent approximation.

Let us be more specific. The probability that the strongest individual amplification is smaller than $A$, is equal to the probability that all $N$ lenses individually produce an amplification smaller than $A$. Hence, the probability $P(A)$ that the strongest amplification is larger than $A$ reads

$$P(A) = 1 - \left[1 - \int_A^\infty \mathrm{d}A'\, p_1(A')\right]^N . \tag{4.14}$$

The strongest-lens approximation consists in assuming that the above is a good model for the CDF of the total amplification.

Examining the expression (4.11) of $p_1(A)$, we notice that it is proportional to $1/N$,

$$p_1(A) \propto \frac{\langle \vartheta_E^2 \rangle}{\Theta^2} = \frac{1}{N}\Sigma\pi\left\langle \vartheta_E^2 \right. \approx \frac{1}{N}\frac{\tau}{1-\kappa_{os}} , \tag{4.15}$$

where we recognised the projected angular density of lenses within the mesoscopic cone, $\Sigma = N/(\pi\Theta^2)$, and the microlensing optical depth $\tau = \Sigma\pi\,\langle\theta_E^2\rangle$. We also considered $\langle\vartheta_E^2\rangle \approx \langle\theta_E^2\rangle/(1-\kappa_{os})$, as suggested by eq. (4.10) where $\kappa_{od}, \kappa_{ds}$ only produce minor

corrections.[3] Thus, in the large-$N$ limit, we have

$$P(A) \approx 1 - \exp\ -\int_A^\infty \mathrm{d}A'\ N p_1(A')\ . \tag{4.16}$$

Substituting the explicit expression of $p_1(A)$, and changing the integration variable to $X \equiv A/A_{\min}$, we finally obtain the main result of this article,

$$\boxed{P(A; z_\mathrm{s}, \alpha, \bar{\kappa}_\mathrm{os}) = 1 - \exp\ -\frac{2\tau}{1-\kappa_\mathrm{os}} \int_{A/A_\mathrm{min}}^\infty \frac{\mathrm{d}X}{(X^2-1)^{3/2}}\ \mathcal{K}\ \frac{\tau X}{(1-\kappa_\mathrm{os})^{7/4}}}\quad , \tag{4.17}$$

with the parameters $\tau = \alpha(\Delta_\mathrm{os} + \bar{\kappa}_\mathrm{os})$, $\kappa_\mathrm{os} = (1-\alpha)\bar{\kappa}_\mathrm{os} - \alpha\Delta_\mathrm{os}$ and $A_\mathrm{min} = (1-\kappa_\mathrm{os})^{-2}$, which explicitly depend on the fraction $\alpha$ of compact objects, the homogeneous convergence deficit $\Delta_\mathrm{os}(z_\mathrm{s})$ given in eq. (2.19), and the average weak-lensing convergence $\bar{\kappa}_\mathrm{os}$ that would be observed if all the matter were diffuse. Note that eq. (4.17) is independent of the size $\Theta$ of the mesoscopic cone that we started with. In the case where the external convergence and shear are neglected, i.e. $\kappa_\mathrm{os} = 0, A_\mathrm{min} = 1, \mathcal{K} = 1$, we recover the simple result of eq. (2.14).

## 4.3 Marginalising over the line-of-sight convergence

Equation (4.17) gives the amplification CDF within a mesoscopic area of the sky where $\bar{\kappa}_\mathrm{os}$, and hence $\tau, \kappa_\mathrm{os}$ can be considered fixed. The full CDF is obtained by marginalising over all mesoscopic lines of sight, that is

$$P(A; z_\mathrm{s}, \alpha) = \int \mathrm{d}\bar{\kappa}_\mathrm{os}\ p(\bar{\kappa}_\mathrm{os}; z_\mathrm{s})\, P(A; z_\mathrm{s}, \alpha, \bar{\kappa}_\mathrm{os})\ . \tag{4.18}$$

Just like in sec. 2.3, we use the results from simulations and standard cosmology to estimate $p(\bar{\kappa}_\mathrm{os}; z_\mathrm{s})$, as explained in sec. A.1.

The final amplification CDF is depicted in fig. 4.5, for different values of the fraction $\alpha$ of compact objects and of the source redshift $z_\mathrm{s}$. As expected, the probability of high amplifications increases with both $\alpha$ and $z_\mathrm{s}$, because the optical depth $\tau$ increases with both parameters. For a source at $z_\mathrm{s} = 1$, the probability that it is amplified by a factor larger than two is 1.6 % if all the DM (83 % of the total matter) in the universe is made of compact objects. This probability falls to 0.23 % if 10 % of matter is compact, and to 0.056 % if only 1 % of the matter is compact.

The upper panels of fig. 4.5 show both the exact $P(A; z_\mathrm{s}, \alpha)$ and the case where

[3] This implies that the weakly lensed optical depth is approximated as $\Sigma\pi\ \vartheta_\mathrm{E}^2\ \approx \tau/(1-\kappa_\mathrm{os})$. In the presence of a positive convergence, i.e. an overdense line of sight, the effective optical depth is thus larger than the one expected without accounting for the convergence corrections.

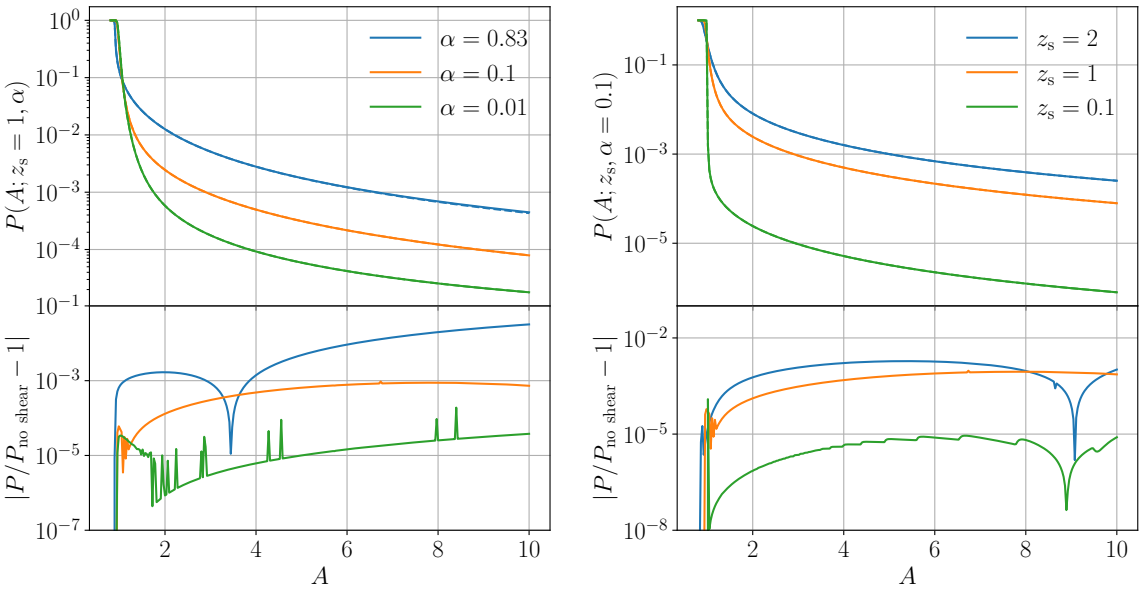


Figure 4.5: Final CDF of the amplification, $P(A; z_s, \alpha) \equiv \text{Prob}(> A|z_s; \alpha)$, once marginalised over the line-of-sight convergence $\bar{\kappa}_{\rm os}$. *Left*: dependence in the fraction $\alpha$ of compact objects for $z_s = 1$. *Right*: dependence in the source redshift $z_s$, for $\alpha = 0.1$. Upper panels indicate both the exact result (solid lines) and the case where the effect of shear is neglected therein, i.e., for $\mathcal{K} = 1$ (dashed lines). The solid and dashed lines are superimposed – their relative difference is depicted in the bottom panels; the rapidly oscillating features are non-physical artefacts due to numerical integration.

microshear is neglected, which corresponds to setting $\mathcal{K} = 1$ in eq. (4.17),

$$P_{\text{no shear}}(A; z_s, \alpha, \bar{\kappa}_{os}) \equiv 1 - \exp\left[-\frac{2\tau}{1-\kappa_{os}} \int_{A/A_{min}}^{\infty} \frac{dX}{(X^2-1)^{3/2}}\right] \tag{4.19}$$

$$= 1 - \exp\left[-\frac{2\tau}{1-\kappa_{os}} \left(\frac{A}{\sqrt{A^2 - A_{min}^2}} - 1\right)\right]. \tag{4.20}$$

The associated curves are essentially indistinguishable by eye; their relative difference, $|P/P_{\text{no shear}} - 1|$, is shown in the bottom panels of fig. 4.5 and is sub-percent for $A < 6$. Of course, due to the behaviour of the function $\mathcal{K}(x)$, larger amplifications ($A \sim 1/\tau$) are expected to be affected more significantly by the microshear. But in practice such high amplifications are so rare that they have no observational relevance. Hence, the main take-home message of this subsection is that *the effect of shear is negligible in the statistics of extragalactic microlensing*. This implies that, for practical purposes, one may safely use the simple no-shear expression (4.20) for $P(A; z_s, \alpha; \bar{\kappa}_{os})$. Such a conclusion could hardly have been guessed from the beginning. The external shear is known to be a crucial parameter in the modelling of strong lenses (e.g. [112]), and fig. 3.3 shows that it generally has a significant impact on the amplification cross section. But since the effect shows up around amplifications $A \sim 1/\tau$, and that the amplification PDF is already low for $A \gtrsim 1/\tau$, the net integrated effect on $P(A)$ ends up being negligible for interesting values of $A$.[4]

## 4.4 Comparison with Zumalacárregui & Seljak

In ref. [69] (hereafter ZS17), Zumalacárregui & Seljak have set constraints on the fraction of extragalactic compact objects that would produce a microlensing signal in the supernova data. For that purpose, they used a phenomenological model for the amplification statistics. It is worth comparing the predictions of that model to our approach in order to evaluate what one may call *theoretical systematics* on any analysis of supernova microlensing.

ZS17's model, based on earlier developments by Seljak & Holz [66] and Metcalf & Silk [65, 68], is expressed in terms of a shifted magnification $\mu$, such that $1+\mu$ represents the magnification of an image with respect to its empty-beam counterpart, i.e., if that image were seen through an empty universe. It is related to our amplification $A$ as

$$1 + \mu = (1 + \Delta_{os})^2 A \ , \tag{4.21}$$

where $\Delta_{os}$ is the same as defined in eq. (2.19). With such conventions, $\mu = 0$ corresponds to $A = (1 + \Delta_{os})^{-2}$, which is indeed the empty-beam case. The distribution of

[4] Another argument is that, for realistic sources of light, large amplifications such that $A \sim 1/\tau$ are very hard to access due to the finite size of the sources (see chapter 5). However, with gravitational waves sources, magnification factors of many hundreds are possible and therefore the net effect could not be negligible.

$\mu$ is then designed by assuming that $\mu$ can be written as the sum $\mu = \mu_\mathrm{s} + \mu_\mathrm{c}$ of a weak-lensing contribution from the smooth matter, $\mu_\mathrm{s}$, and a microlensing contribution from compact objects, $\mu_\mathrm{c}$.

The smooth part is written as $\mu_\mathrm{s} = (1-\alpha)\bar{\mu}$, where $\bar{\mu}$ would be the magnification in the absence of compact objects. Note that this is quite similar to our approach described in subsec. 3.2.2, except that we have worked with convergences rather than shifted magnifications. In ZS17, the statistics of $\bar{\mu}$ are obtained using the `TurboGL` code [113, 114].

The statistics of microlensing part, $\mu_\mathrm{c}$, are based on an empirical model originally used by Rauch to fit ray-shooting simulations in ref. [115],

$$p_\mathrm{R}(\mu_\mathrm{c}; \bar{\mu}_\mathrm{c}) = N \left( \frac{1 - \mathrm{e}^{-\mu_\mathrm{c}/\Delta\mu}}{(1+\mu_\mathrm{c})^2 - 1} \right)^{3/2} , \tag{4.22}$$

where $N$ and $\Delta\mu$ are two functions of $\bar{\mu}_\mathrm{c}$ that are chosen so as to ensure that $p_\mathrm{R}$ is normalised to 1 and with expectation value $\langle \mu_\mathrm{c} \rangle = \bar{\mu}_\mathrm{c}$. This value is set to be $\bar{\mu}_\mathrm{c} = \alpha\bar{\mu}$ by the magnification theorem [93], and plays a role comparable to the optical depth $\tau$ in our approach.

In such conditions, ZS17's model for the PDF of the magnification $\mu = \mu_\mathrm{c} + \mu_\mathrm{s}$ reads

$$p_\mathrm{ZS17}(\mu; z_\mathrm{s}) = \int_0^\infty \mathrm{d}\bar{\mu}\; p_\mathrm{TurboGL}(\bar{\mu}; z_\mathrm{s})\, p_\mathrm{R}[\mu - (1-\alpha)\bar{\mu}; \alpha\bar{\mu}] , \tag{4.23}$$

which undoubtedly has the advantage of simplicity. Figure 4.6 shows a comparison between the predictions of our model with those of ZS17's model, in the case of point-like sources for simplicity. Compared to our approach, ZS17's model tends to overestimate by more than 10 % the large-amplification events for high values of $\alpha$; for low values of $\alpha$, on the contrary, it tends to underestimate them by more than 100 %. Coincidentally, both models nearly agree (up to a few percent) for $\alpha = 0.35$, which turns out to be the maximum fraction of compact objects allowed at 95 % confidence level in ZS17. Since $P_\mathrm{ZS17}(A) > P(A)$ for smaller values of $\alpha$, this suggest that conducting an analysis similar to ZS17's with our model for amplification statistics would yield slightly weaker constraints on $\alpha$. Such an analysis is beyond the scope of this article, but the present results show that theoretical systematics can generally reach 100 % for extragalactic microlensing.

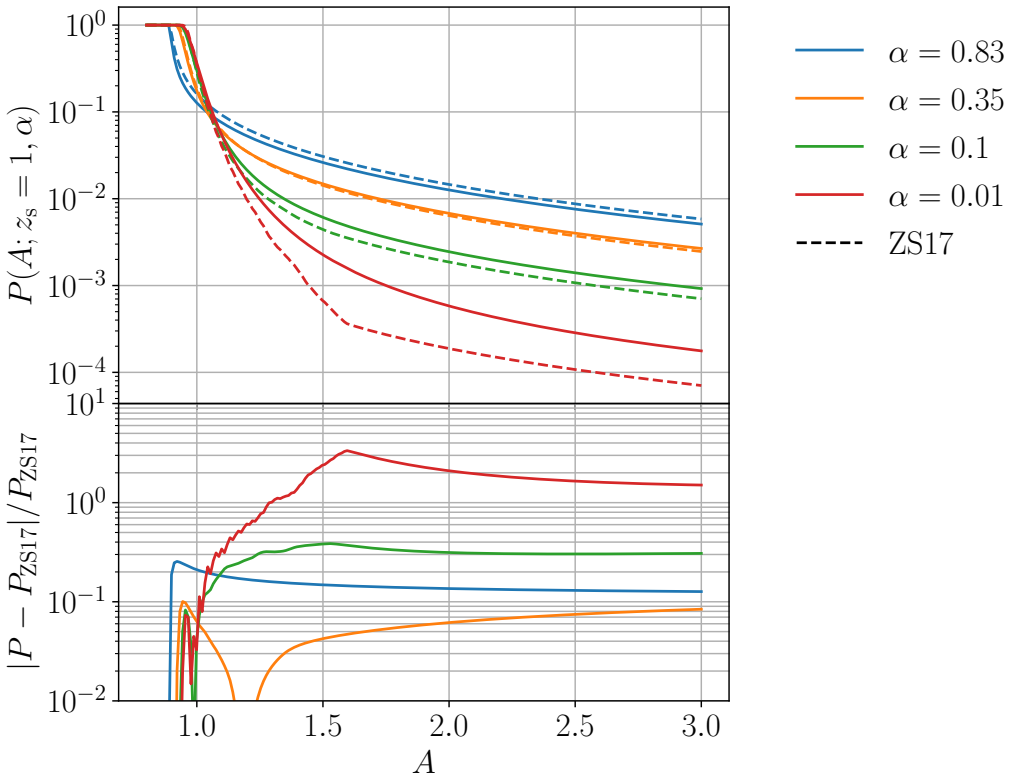


Figure 4.6: Comparison of our model for the amplification CDF (solid lines) and the phenomenological model used in ZS17 [69] (dashed lines), for point-like sources at $z_s = 1$ and different values of the fraction of compact objects $\alpha$.

CHAPTER

# FIVE

# EXTENDED SOURCES

So far we have considered point-like sources, but the finite size of real light sources is known to have significant effects on the amplification distribution. As a rule of thumb, if a source has an unlensed angular size $\sigma$, then it smoothes out the amplification map obtained in the point-source case on the angular scale $\sigma$ – see e.g. fig. 13 of ref. [89] for illustration. This implies that the effect of small structures, i.e. lenses with small Einstein radii, is suppressed.[1] In this subsection, we show how to add finite-source corrections to the amplification distributions derived in the previous sections.

## 5.1 Extended-source corrections on an isolated point lens

We have seen in subsec. 3.2.3 that the problem of a point lens with tidal corrections can be conveniently phrased as an equivalent point lens with a single effective shear correction. Besides, the analysis leading to fig. 4.5 shows that the effect of shear is statistically negligible in the point-source case. Since the extended-source case is deduced from the point-source case by a smoothing of its amplification map, if the effect of shear is small in the latter, it must also be small in the former. Hence, in all the remainder of this section we shall neglect the shear, so the equivalent lens is a mere unperturbed point lens,

$$\tilde{\boldsymbol{\beta}} = \tilde{\boldsymbol{\theta}} - \frac{\tilde{\theta}_{\mathrm{E}}^2}{\tilde{\boldsymbol{\theta}}} \ , \tag{5.1}$$

where the twiddled quantities are expressed in terms of the original ones in eqs. (3.13) to (3.15), all the shears being set to zero.

Let us now consider a source shaped as a disk with angular radius $\sigma$, and whose surface brightness is homogeneous within the disk. Since we are neglecting the shear, the source shape is still a disk in the twiddled world, with radius $\tilde{\sigma} = (1 - \kappa_{\mathrm{od}})(1 -$

[1] That is why, for example, the constraints on the abundance of PBHs set by SN microlensing in ref. [69] only apply to masses larger than $10^{-2} M_\odot$.

$\kappa_{\rm ds})^{-1}(1-\kappa_{\rm os})^{-1}\sigma$. The amplification profile of such a homogeneous disk source by a point lens was derived in ref. [116]. If $\tilde{\beta}$ denotes, in the twiddled world, the angle between the centre of the source and the main lens, we define the reduced impact parameter as $\tilde{u} \equiv \tilde{\beta}/\tilde{\theta}_{\rm E}$ and the reduced source's radius $\tilde{r} \equiv \tilde{\sigma}/\tilde{\theta}_{\rm E}$; the amplification profile then reads

$$\tilde{A}(\tilde{u},\tilde{r}) = \frac{\tilde{u}+\tilde{r}}{2\pi\tilde{r}^2}\ \sqrt{4+(\tilde{u}-\tilde{r})^2}\,\mathrm{E}(m) - \frac{\tilde{u}-\tilde{r}}{2\pi\tilde{r}^2}\frac{8+(\tilde{u}^2-\tilde{r}^2)}{\sqrt{4+(\tilde{u}-\tilde{r})^2}}\,\mathrm{F}(m) + \frac{2(\tilde{u}-\tilde{r})^2}{\pi\tilde{r}^2(\tilde{u}+\tilde{r})}\frac{1+\tilde{r}^2}{\sqrt{4+(\tilde{u}-\tilde{r})^2}}\,\Pi(n,m)\ , \quad (5.2)$$

where

$$n \equiv \frac{4\tilde{u}\tilde{r}}{(\tilde{u}+\tilde{r})^2}\ , \qquad m \equiv \frac{4n}{4+(\tilde{u}-\tilde{r})^2}\ , \quad (5.3)$$

and the functions F, E and Π are the complete elliptic integrals of the first, second and third type, respectively, in Wolfram's convention for elliptic integrals[2]. The maximum amplification is obtained when $\tilde{u}=0$ and reads

$$\tilde{A}_{\rm max}(\tilde{r}) \equiv \tilde{A}(0,\tilde{r}) = \sqrt{1+\frac{4}{\tilde{r}^2}}\ , \quad (5.4)$$

which goes to infinity as the source becomes very small ($\tilde{r}\to 0$). More generally, the entire amplification profile of the point-source case (2.10) is recovered in that limit. The left panel of fig. 5.1 illustrates the amplification profile for several values of $\tilde{r}$.

In the next sections, we proceed with the calculation of the amplification probability in the presence of finite-source corrections. This calculation will closely follow the point-source case: amplification cross-section; strongest-lens approximation; and marginalisation over the mesoscopic cone.

## 5.2 Amplification cross section of an isolated lens

With an extended source, the amplification profile changes from eq. (2.10) to eq. (5.2), so the differential cross section amplification must change as well. In particular, since $\tilde{A} \le \tilde{A}_{\rm max}(\tilde{r})$, we must have $\tilde{\Omega}_{\tilde{\sigma}}(\tilde{A} > \tilde{A}_{\rm max}) = 0$. Thanks to the axial symmetry of the amplification profile, just like the point-lens case, we have

$$\tilde{\Omega}_{\tilde{\sigma}}(\tilde{A}) = 2\pi\tilde{\beta}(\tilde{A},\tilde{r})\ \frac{\partial\tilde{\beta}}{\partial\tilde{A}}\ = \pi\tilde{\theta}_{\rm E}^2\ \frac{\partial\tilde{u}^2}{\partial\tilde{A}}\ , \quad (5.5)$$

except that now $\tilde{u}(\tilde{A},\tilde{r})$ is the inverse of eq. (5.2) at fixed $\tilde{r}$, which cannot be done analytically.

[2] `https://reference.wolfram.com/language/guide/EllipticIntegrals.html`

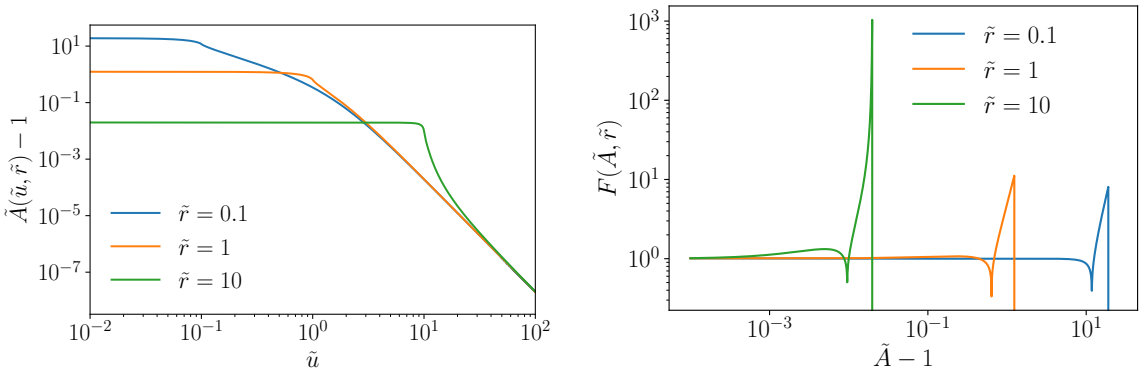


Figure 5.1: Finite-source corrections for the amplification of a homogeneous disk source with angular radius $\tilde{\sigma} = \tilde{r}\tilde{\theta}_\mathrm{E}$ by a point lens with Einstein radius $\tilde{\theta}_\mathrm{E}$. *Left*: Amplification profile $\tilde{A}$ as a function of the reduced impact parameter $\tilde{u} = \tilde{\beta}/\tilde{\theta}_\mathrm{E}$. The larger the source, the smoother the profile and the smaller the maximum amplification. *Right*: Correction factor to the differential amplification cross section, $F \equiv \tilde{\Omega}_{\tilde{\sigma}}/\tilde{\Omega}_0$, for the same values of $\tilde{r}$.

For later convenience, we introduce the finite-source factor $F$ as the ratio between the finite-source and point-source amplification cross sections,

$$F(\tilde{A},\tilde{r}) \equiv \frac{\tilde{\Omega}_{\tilde{\sigma}}(\tilde{A})}{\tilde{\Omega}_0(\tilde{A})} = \frac{\partial\tilde{\beta}^2}{\partial\tilde{A}}\,\frac{\mathrm{d}\tilde{A}}{\mathrm{d}\tilde{\beta}_0^2}\ . \tag{5.6}$$

This way, finite-source corrections are fully encapsulated in a single function, just like shear corrections were encapsulated in the function $k$ in sec. 3.3. A significant difference, however, is that the function $F$ has two variables while $k$ had only one, which makes the analysis technically harder. The right panel of fig. 5.1 shows three examples of $\tilde{A} \mapsto F(\tilde{A},\tilde{r})$, for $\tilde{r} = 0.1, 1, 10$. As expected, for low amplifications $F \approx 1$, which translates the fact that far from the lens, the finiteness of the source has essentially no effect. For larger amplifications, the cross section is enhanced for $\tilde{A} \lesssim \tilde{A}_\mathrm{max}(\tilde{r})$ and then suddenly drops to zero beyond.

The amplification cross section in the original problem (non-twiddled world) is obtained from $\tilde{\Omega}(\tilde{A})$ similarly to subsec. 3.3.2. The calculation uses that, in terms of the original quantities, $\tilde{r} = \sqrt{A_\mathrm{min}}\,\sigma/\vartheta_\mathrm{E}$. The final result is

$$\Omega_\sigma(A) = 2\pi\vartheta_\mathrm{E}^2\,F\left(\frac{A}{A_\mathrm{min}},\ \frac{\sigma}{\sqrt{A_\mathrm{min}}\,\vartheta_\mathrm{E}},\ \frac{A_\mathrm{min}^2}{(A^2-A_\mathrm{min}^2)^{3/2}}\right)\ . \tag{5.7}$$

## 5.3 Amplification probabilities with extended sources

Just like in the point-lens case, the amplification PDF for one lens in a mesoscopic cone with half angle $\Theta$ reads

$$p_1(A;\sigma) = \frac{1}{\pi\Theta^2}\int \mathrm{d}m\,\mathrm{d}\chi\ p(m,\chi)\,\Omega_\sigma(A;m,\chi)\ . \tag{5.8}$$

Substituting eq. (5.7) and $p(m,\chi) = (3\chi^2/\chi_\mathrm{s}^3)\,p(m)$, we may again gather all the finite-source corrections within a single function as

$$p_1(A;\sigma) = \frac{2\,\langle\vartheta_\mathrm{E}^2\rangle}{\Theta^2}\,\frac{A_\mathrm{min}^2}{(A^2-A_\mathrm{min}^2)^{3/2}}\,\mathcal{F}\quad\frac{A}{A_\mathrm{min}},\sigma,\kappa_\mathrm{os}\quad, \tag{5.9}$$

with $\mathcal{F} \equiv \langle\vartheta_\mathrm{E}^2 F\rangle \,/\, \langle\vartheta_\mathrm{E}^2\rangle$, that is, explicitly,

$$\mathcal{F}(X,\sigma,\kappa_\mathrm{os}) = \frac{\int_0^{\chi_\mathrm{s}} \frac{\mathrm{d}\chi}{a(\chi)}\,\frac{1-\kappa_\mathrm{ds}}{1-\kappa_\mathrm{od}}\,\chi(\chi_\mathrm{s}-\chi)\int \mathrm{d}m\;\frac{m}{\langle m\rangle}\,F\quad X,\sigma\quad\overline{\frac{1-\kappa_\mathrm{od}}{(1-\kappa_\mathrm{os})(1-\kappa_\mathrm{ds})}\,\frac{a(\chi)\chi\chi_\mathrm{s}}{4Gm(\chi_\mathrm{s}-\chi)}}}{\int_0^{\chi_\mathrm{s}} \frac{\mathrm{d}\chi}{a(\chi)}\,\frac{1-\kappa_\mathrm{ds}}{1-\kappa_\mathrm{od}}\,\chi(\chi_\mathrm{s}-\chi)}\quad, \tag{5.10}$$

where $X = A/A_\mathrm{min}$. Equation (5.9) is formally quite similar to eq. (4.11), which was the case of point-like sources with external shear. However, here the correction factor $\mathcal{F}(X,\sigma,\kappa_\mathrm{os})$ has three variables, instead of one for the function $\mathcal{K}(x)$ of eq. (4.11).

Figure 5.2 shows examples of the $\mathcal{F}$ function for two types of sources (SNe and QSOs)[3] at $z_\mathrm{s} = 1$, in the case where all the compact objects have the same mass $m$; we have set all the convergences to zero for simplicity. As expected, $\mathcal{F}$ being a smoothed version of $F$, it preserves some of its features; in particular, the amplification probability is suppressed beyond a critical value of $X = A/A_\mathrm{min}$. For a given source size $\sigma$, the lower the deflectors' mass $m$, the larger the values of $r$ and hence the smaller the critical amplification; this is apparent in both panels of fig. 5.2, where the curves are displaced to the left as $m$ decreases. For relatively large values of the deflectors' mass, $\mathcal{F}(X,\sigma)$ is almost self-similar. As expected, the lens mass required to allow large amplifications to happen is much larger for QSOs than for SNe, because the latter is much closer to a point source than the former.

Finally, the total amplification CDF, produced by an infinite population of lenses in the mesoscopic cone, is derived from eq. (5.9) following the exact same method as in sec. 4.2, i.e. in the framework of the strongest-perturbed lens approximation. The result is

$$\boxed{P(A;\sigma,z_\mathrm{s},\alpha,\bar\kappa_\mathrm{os}) = 1-\exp\quad\frac{-2\tau}{1-\kappa_\mathrm{os}}\int_{A/A_\mathrm{min}}^{\infty}\frac{\mathrm{d}X}{(X^2-1)^{3/2}}\,\mathcal{F}(X,\sigma,\kappa_\mathrm{os})\quad,} \tag{5.11}$$

with $\tau = \alpha(\Delta_\mathrm{os}+\bar\kappa_\mathrm{os})$, $\kappa_\mathrm{os} = (1-\alpha)\bar\kappa_\mathrm{os} - \alpha\Delta_\mathrm{os}$ and $A_\mathrm{min} = (1-\kappa_\mathrm{os})^{-2}$. Averaging over the mesoscopic cone is obtained by marginalising over $\bar\kappa_\mathrm{os}$, as discussed in sec. 4.3.

Examples of $P(A;z_\mathrm{s},\alpha,\bar\kappa_\mathrm{os},\sigma)$ for various values of its parameters are depicted in fig. 5.3; we fixed $\bar\kappa_\mathrm{os} = 0$ for simplicity. Compared to the point-source case, the amplification probability is slightly enhanced near some critical value that depends on

[3]The typical size of type-Ia SNe can be inferred from the typical expansion velocity of $20\,000\,\mathrm{km\,s^{-1}}$ of the luminous envelope about a month after explosion, which gives around 2 light-days, or 300 AU. The size of the inner region of QSO, which suffers the effect of microlensing, is also about 4 to 8 light-days [117, 118].

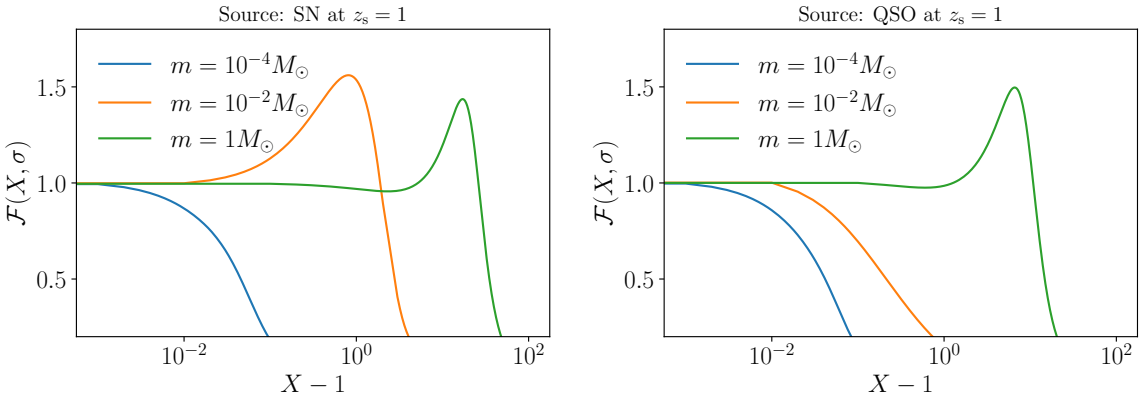


Figure 5.2: Examples of the extended-source correction factor $\mathcal{F}(X, \sigma, \kappa_{\rm os} = 0)$ involved in eq. (5.9), for two different kind of sources at $z_{\rm s} = 1$, in the case where all the compact objects have the same mass $m$. *Left*: The sources are SNe, with physical radius 300 AU, i.e. $\sigma_{\rm SN} = \mathcal{O}(10^{-13})$ rad at $z_{\rm s} = 1$. *Right*: The sources are QSOs, with physical radius 4 light days, i.e. $\sigma_{\rm QSO} = \mathcal{O}(10^{-9})$ rad at $z_{\rm s} = 1$.

the lens masses, source redshift and size, after what it gets quickly suppressed. As expected from our analysis of the function $\mathcal{F}$, finite-source effects are stronger as the source size increases and the mass of the compact objects decreases.

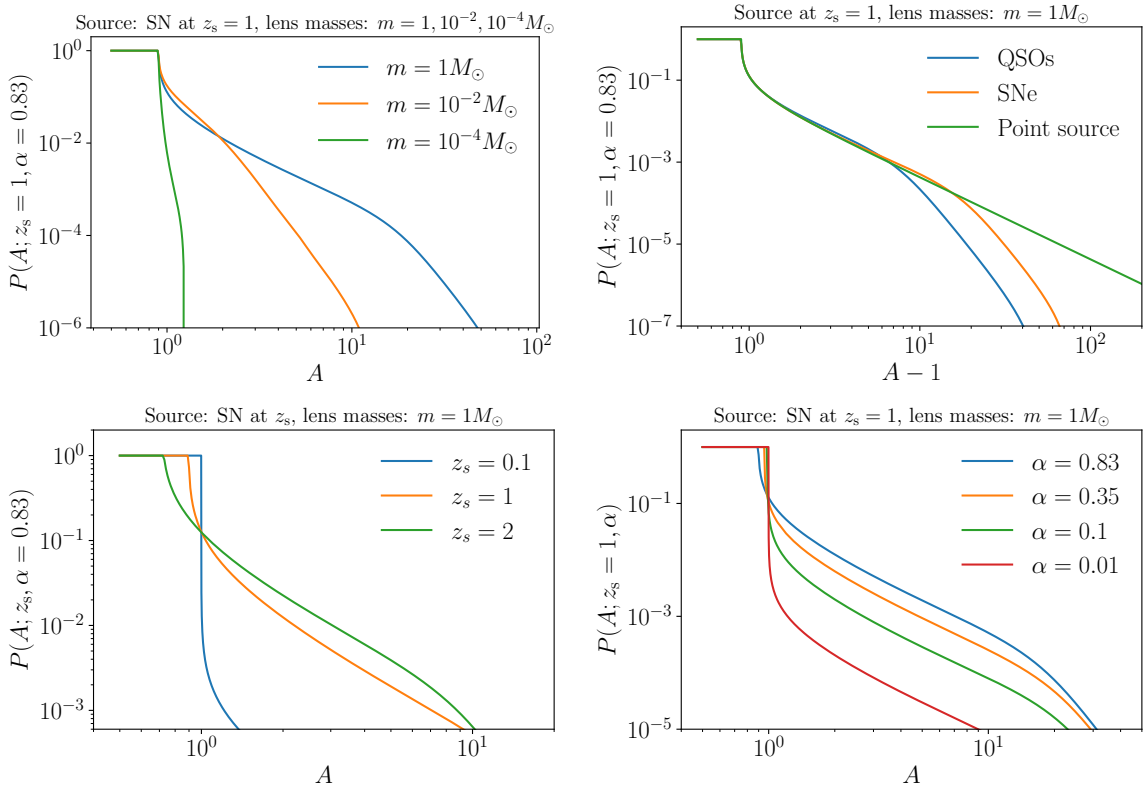


Figure 5.3: Examples of the amplification CDF $P(A; \sigma, z_s, \alpha, \bar{\kappa}_{os})$ with extended sources, as given by eq. (5.11), for a line of sight with $\bar{\kappa}_{os} = 0$. *Top left:* Varying the mass $m$ of the compact objects. *Top right:* Changing the source type, namely point sources, SNe [physical radius 300 AU i.e. $\sigma_{SN} = \mathcal{O}(10^{-13})$ at $z_s = 1$], and QSOs [physical radius 4 light days i.e. $\sigma_{QSO} = \mathcal{O}(10^{-9})$ at $z_s = 1$]. *Bottom left*: Varying the source redshift $z_s$. *Bottom right*: Varying the fraction $\alpha$ of compact objects.

CHAPTER

# SIX

# CONCLUSION

Extragalactic microlensing is a potentially powerful probe of the nature of dark matter (DM). In particular, a handful of past studies have used supernova microlensing to set constraints on the fraction of intergalactic DM that could be made of compact objects. Those analyses relied on a simple phenomenological modelling of the microlensing amplification statistics, which did not account for the coupling between the main deflector responsible for the amplification and its environment – the other lenses and the large-scale cosmic structures. Such an approximation is expected to be valid in the limit of very low optical depths, and for lines of sight that are representative of the mean homogeneous and isotropic model.

In this work, we started assessing the validity of the very-low-optical-depth assumption, and found that for observationally interesting values of the microlensing amplification, relevant optical depths are low to mild ($\tau \lesssim 0.1$). This first result, together with the known fact that environmental effects are generally non-negligible in strong lensing, suggests that environmental and line-of-sight corrections may be significant in extragalactic microlensing. Hence, they must be taken into account in order to accurately predict the probability of microlensing amplification by a cosmic population of compact objects.

We have derived, from first principles, an expression for the amplification probability that we expect to be valid up to mild optical depths. Our approach, which may be referred to as the "strongest perturbed lens model", consistently accounts for: (i) the external convergences due to overdensities or underdensities in the smooth matter distribution along the line of sight; and (ii) the external shears produced by the large-scale structure and the lenses near the line of sight. This result and its derivation constitute the main focus of the article. The derivation was performed in the case of point-like sources of light, but we also explicitly derived the extended-source corrections for completeness. In numerical illustrations, the statistical distributions of the line-of-sight convergences and shears were extracted from ray tracing in $N$-body simulations, for which we found interesting fitting functions.

From this new model of microlensing amplification probabilities, two conclusions turn out to be particularly noteworthy. First, in observationally relevant situations, the effect of external shear (both due to the large-scale structure and to compact objects near the line of sight) is statistically negligible – corrections are at most on the order of a part in a thousand. Second, however, the predictions of our model are still quantitatively discrepant from the literature, with relative differences larger than 100 % in some cases. Such differences might be explained from our non-linear treatment of the external convergences and our careful embedding of microlenses within the cosmic large-scale structure. This result emphasises the crucial importance of an elaborate theoretical modelling of amplification statistics in order to extract accurate constraints on the fraction of compact objects in the universe.

The next step of this work naturally consists in applying its result to, e.g., SN data similarly to what was done in refs. [66, 65, 68, 69, 119]. This will require an efficient numerical implementation of our model for the amplification probability, which can be technically challenging for extended-source corrections. Application to data requires to properly deal with their outliers, in order to distinguish between lensed and intrinsically anomalous SNe.

# Part II

# Gravitational wave propagation in a clumpy universe

# ABSTRACT

Just like light, gravitational waves can also experience gravitational lensing in the presence of a gravitational field. However, the wavelength of gravitational waves is larger than in the electromagnetic case and the geometric optics approximation may no longer hold. Diffraction effects may arise and one has to use a full wave optics treatment. In the second part of this thesis, we investigate the scales in which these effects are important and detectable. An important conclusion is that these scales are normally very tiny implying that, in most of the cases, geometric optics is a valid approximation. However, interference effects may arise also in this regime. We thus propose a new terminology for that particular case. Finally we compute the expected rate of lensed events for three different scenarios: (i) a universe filled with compact objects in which microlensing effects are observable; (ii) a universe filled with dark matter halos in which the change of the waveform is due to strong lensing effects; (iii) the same dark matter halos filled with compact objects in which the strong lensing signal is observed with small microlensing contributions. An other important conclusion is that lensed events are expected to be observed in the current and near future observation runs. Just like light, lensing of gravitational wave is a potentially powerful probe to study and constrain the abundance of compact objects.

CHAPTER

# SEVEN

# INTRODUCTION

This chapter highlights the major events in the history of lensing of gravitational waves[1] and the previous works that have motivated the second part of this thesis.

## 7.1 A gravitational and electromagnetic analogy

As mentioned in Part I, the eighteenth century gave rise to an intense debate about the nature of light. The wave theory of Huygens was contradicted in 1861 by the Scottish mathematician James Clerk Maxwell, who proposed that light is an electromagnetic phenomenon that can propagate through vacuum without the need of a medium [4]. In 1865, he published the article *A Dynamical Theory of the Electromagnetic Field* and showed that electromagnetic fields can propagate through space as waves, moving at the speed of light [121]. His theory suggested that light is a form of oscillation within the same field responsible for electric and magnetic phenomena.

In 1893 the British mathematician and physicist Oliver Heaviside, who used Maxwell's equations to made significant contributions to the development of electromagnetic theory and telegraphy, published his paper *A Gravitational and Electromagnetic analogy* where he used the electromagnetic theory to study gravity and the possibility of waves propagating through the gravitational field [122]. In the first part of the article, he uses the analogy between the inverse-square law of gravitation and the electrostatic force to define a wave equation for gravity that could be form without the presence of matter. In the second part of the volume, he suggests that it is likely that the speed of propagation of gravity is equal to that of light. Although indirectly, Heaviside was the first to propose a theory on the possible existence of *gravitational waves*.

In July 1905, the French Academy of Sciences published a paper written by the French mathematician and theoretical physicist Henri Poincaré entitled *Sur la*

[1]For a more detailed historical introduction of gravitational waves see ref. [120]

*dynamique de l'électron*. In this work he suggested that, just like accelerating electric charges produce electromagnetic waves, accelerating masses should produce waves of energy through gravitational fields. He was the first to call them gravitational waves (*onde gravifique*) [123]. Using Lorentz transformations these proposed gravitational waves should propagate at the speed of light.

## 7.2 Einstein's approximations

In 1915, Albert Einstein published his theory of general relativity [15] where he explains that gravity is geometrical by nature. He tried to emulate Heaviside and Poincaré's idea of gravitational waves by finding an analytical wave solution for gravity similar to electromagnetic waves. Since an oscillating electric dipole generates electromagnetic waves, according to Poincare's idea, a "gravitational dipole" should generate gravitational waves. However, in a gravitational field there is no equivalent to a negative electric charge because there are no negative masses. Furthermore, due to momentum conservation, the rest of the universe should also oscillate. As a result, gravitational waves do not follow a dipole radiation pattern but a quadrupole.

Einstein was therefore a bit skeptical about the idea of gravitational waves. In fact, on February 1916, he wrote a letter to the German physicist Karl Schwarzschild saying, in Einstein's own words, "*according to the final theory there are no gravitational waves analogous to light waves*".[2] This reminds us of his famous quote in which he believed it was impossible to observe gravitational lenses. But this time we needed more years to prove that he was wrong again.

After publishing his theory of general relativity, Einstein did not give up and tried to find a wave equation for gravity. However, Enstein's field equations can only be analytically solved in particular cases with specific approximations and symmetry assumptions. He therefore used some approximations and manipulated his equations to make them look like the Maxwell's equations that predict electromagnetic waves. Finally, under a coordinate system change, he found a wave solution and concluded that there are, in fact, three different types of gravitational waves. Einstein assumed gravitational waves that propagate in an empty and flat space. In 1922, the German mathematician and theoretical physicist Hermann Weyl named these solutions *longitudinal–longitudinal*, *transverse–longitudinal*, and *transverse–transverse* gravitational waves [124].

That year, Arthur Eddington, at the pinnacle of fame due to the discovery of the first experimental evidence of light deflection thanks to the eclipse in 1919, published an article in which he criticizes Einstein's wave solutions. In particular, he suggested that, in the first two solutions, Einstein used a flat space and a coordinate system that oscillates. Consequently, he stated that they were not real gravitational waves.

[2] `https://einsteinpapers.press.princeton.edu/vol8-trans/224`

However, he did not exclude the third solution and proved that it propagates at the speed of light regardless of the coordinate system.

In 1936 Einstein was already a professor at Princeton. He submitted an article to *Physical Review*, together with his young assistant the American-Israeli physicist Nathan Rosen, in which they claimed that gravitational waves do not exist. The referee of the journal, Howard P. Robertson, reported that their conclusion was due only on the existence of cylindrical-coordinate singularities. The Einstein-Rosen manuscript had an important error. That same year, after other scientists confirmed the error, Einstein made fundamental changes in his article with Rosen and arrived to new conclusions. In the paper, renamed *On gravitational waves*, he obtained a solution for cylindrical gravitational waves and concluded that gravitational waves are just conventional cylindrical waves in Euclidean space [125]. Einstein eventually became convinced that gravitational waves actually existed, while Nathan Rosen remained convinced that they were simply a mathematical concept without any genuine physical significance.

In order to settle this debate it was needed to observe the physical effects of gravitational waves in order to prove their existence. The first one to propose this idea was the British theoretical physicist Felix Pirani. In 1956, he published the article *On the physical significance of the Riemann tensor* in which he performed a *gedankenexperiment* and studied the behaviour of free particles moved by waves and provided a physical interpretation for the Riemann tensor [126]. The relevance of his work lies on the fact of assessing the problem of coordinate system choice from a physical point of view. This was further explored in 1969 by the German-American physicist Peter Bergman, an important Einstein's collaborator. In his article *The Riddle of Gravitation* he described how a set of particles would move in the presence of a gravitational wave [127]. When a gravitational wave passes over a set of particles, it causes them to experience a slight distortion in their positions, perpendicular to the gravitational wave direction. This distortion is known as the strain, and it is proportional to the amplitude of the gravitational wave.

Bergmann's work helped to establish the mathematical formalism for describing the strain induced by a gravitational wave. Later on it was showed that the strain could be decomposed into two polarizations, known as the "plus" and "cross" polarizations, which correspond to different directions of stretching and squeezing (fig. 7.1).

## 7.3 The first detector

1957 was an important year in the history of gravity. In a meeting in Chapel Hill, North Carolina, the interest in searching for gravitational waves began. At that time, the community was focused on whether gravitational waves could transmit energy.

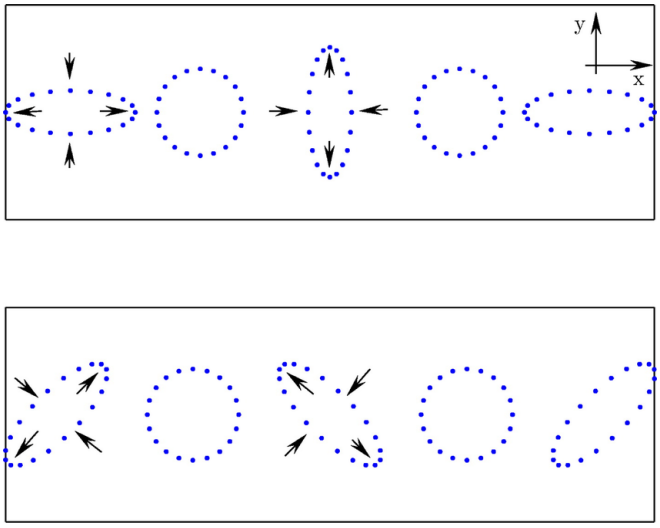


Figure 7.1: When a gravitational wave passes over a set of particles, it causes their directions to stretch (top) and squeeze (bottom). Credit to ref. [128].

At that meeting,[3] the American theoretical physicist Richard Feynman proposed an experiment to solve the issue. This thought experiment, known today as the "sticky bead argument", involves two beads initially at rest threaded on a horizontal wire that is free to move. If a gravitational wave passes transversely through the wire it would produce longitudinal compressive stress and the beads would eventually start to move and oscillate along the wire (fig. 7.2). If the contact between the bead and the wire is "sticky", then they would heat up due to friction implying that the gravitational wave would have transmitted energy to the wire. As a result, gravitational waves can transmit energy. This argument was further developed by the Austrian-British mathematician and cosmologist Hermann Bondi who showed that General Relativity predicts the existence of gravitational radiation and can actually have physical effects. This claim led to a series of papers between 1959 to 1989 by Bondi and Pirani which concluded that gravitational waves are plane waves.

The feat of gravitational wave detection had also its beginning at the meeting in Chapel Hill. The American engineer Joseph Weber, who was in the audience, was fascinated by the discussions about gravitational wave and decided to create a mechanism to detect gravitational waves. In 1966, he developed the first resonant mass gravitational wave detector, which is now commonly known as the "Weber bar" [129]. This pioneering work in the field of gravitational wave detection was essentially a large cylinder made of aluminum that was designed to vibrate at its resonant frequency in response to a passing gravitational wave. The cylinder was suspended by wires and kept in a vacuum to minimize any external disturbances (fig. 7.3).

[3]The Chapel Hill conference is today known as GR1, the first of a series of conferences held every three years and whose aim is to discuss the state of the art in the field of General Relativity and gravitation. The last two editions were GR22, held in Valencia in 2019, and GR23, held in Beijing in 2022.

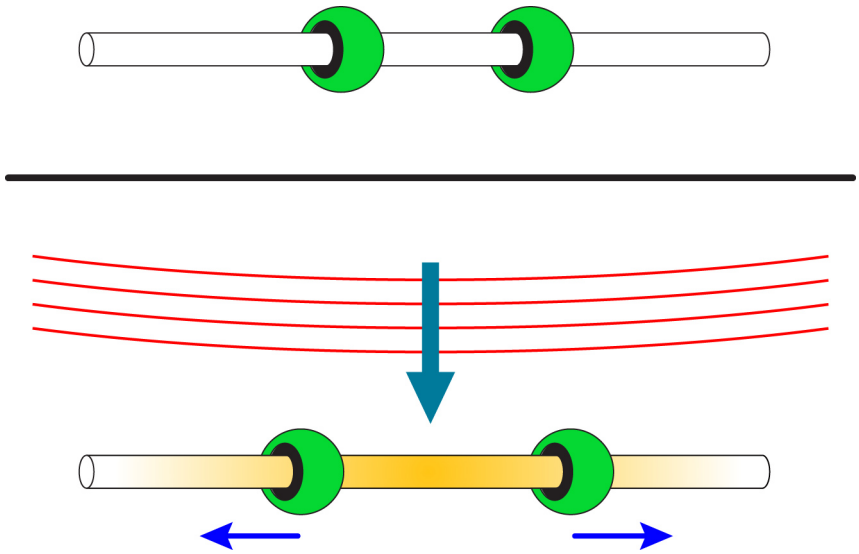

Figure 7.2: Sketch of the "sticky bead argument", originally proposed anonymously by Feynman. Credit to ref. [130].

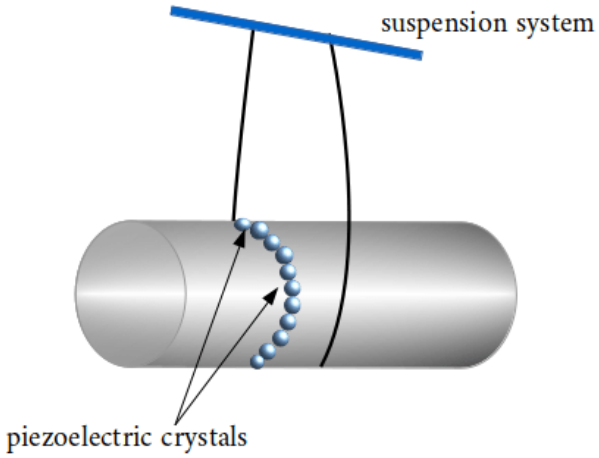


Figure 7.3: Sketch of the cylinder detector. The piezoelectric crystals detect the vibrations induced by gravitational waves. Credit to ref. [131].

When the cylinder vibrated, it would generate a small electrical signal that could be measured and analyzed. In order to minimize the local noise he built two detectors and separated them by 950 km. One was placed at the University of Maryland and the other at the Argonne National Laboratory in Chicago. In 1969, Weber believed that his gravitational wave detector had detected gravitational waves from astrophysical sources from the center of our galaxy [132]. However, his results were controversial and not widely accepted by the scientific community at the time, mainly because other groups built their own "Weber bars" and failed to find any detection.

## 7.4 The laser interferometers: LIGO and Virgo

Gravitational waves are incredibly difficult to detect because gravity is much weaker than electromagnetism. Einstein himself thought that their effect would be practically negligible. Furthermore, by the 1970s many groups searched for detections using and improved Weber's original design but with no success. Consequently, during that period, there was a prevailing sense of pessimism and disappointment among those who were actively searching for gravitational waves. However, in 1974 there was a glimmer of positivism. The American physicists Russell Alan Hulse and Joseph Hooton Taylor Jr. discovered the first binary pulsar using the Arecibo radio telescope in Puerto Rico. The binary pulsar, also known as PSR B1913+16, consists of two neutron stars orbiting around each other in a tight binary system. The discovery was made by observing the regular pulses of radio waves emitted by one of the neutron stars, which was a known pulsar. The observations revealed that the pulsar's pulses were arriving at Earth at slightly different times, depending on the position of the pulsar in its orbit. This indicated that the pulsar was in orbit around another massive object, which was later identified as a second neutron star. The binary pulsar was particularly significant because it provided strong evidence for the existence of gravitational waves. The emission of gravitational waves causes the two neutron stars to gradually lose energy, causing them to spiral closer together at a rate that is consistent with the predictions of General Relativity (fig. 7.4). Hulse and Taylor were awarded the Nobel Prize in Physics in 1993 for their discovery of the binary pulsar and their subsequent measurements of its orbit.

This indirect detection of gravitational waves was announced in 1979 [134] and motivated the community to keep searching for further detections. Some groups started to use interferometric methods in order to observe gravitational waves. The idea of using a laser interferometer was first suggested in 1962 by the soviet physicists M. E. Gertsenshtein and V. I. Pustovoit [135] and first implemented in the early 1970s by the American physicists Robert L. Forward, who was a former student of Weber, and Rainer Weiss.

A laser interferometer is designed to detect small changes in the length of a pair of perpendicular arms. The basic principle is to use interferometry to measure the difference in length between the two perpendicular arms, which are typically on the order of several kilometers. The interferometer consists of a laser beam that is split into two beams, which are then sent down the arms. The beams are then reflected back by a mirror towards the point of origin, where they are recombined. When the beams are recombined, they create a pattern of interference that is used to measure the difference in length between the two arms. If the two arms are exactly the same length, the interference pattern will be perfectly stable. However, if there is a difference in length between the two arms, the interference pattern will shift slightly (fig. 7.5).

In order to detect gravitational waves, the interferometer must be extremely sen-

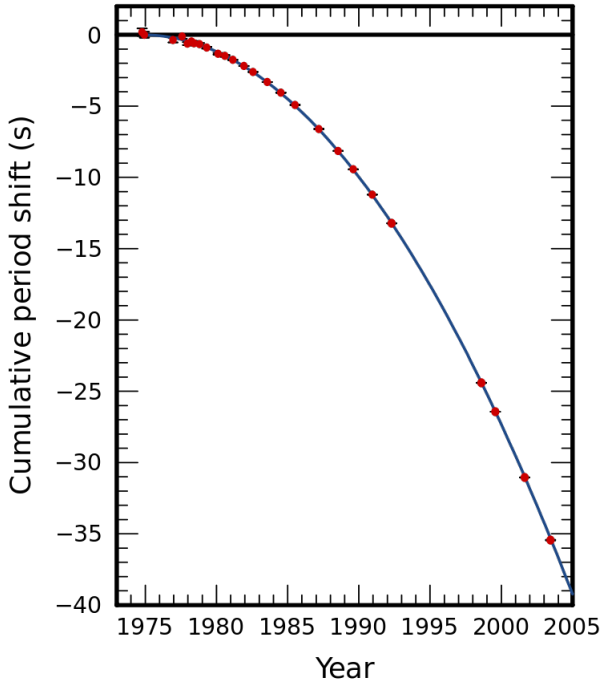


Figure 7.4: Orbital decay of PSR B1913+16. Data points show the point of closest approach of the stars. The solid line show the prediction of General Relativity. Credit to [133].

sitive to changes in length. This requires using a long vacuum tube to isolate the mirrors and reduce any external noise or interference. The vacuum helps to prevent air molecules from interfering with the laser beam. The interferometer must also be carefully designed and constructed to minimize any sources of noise that could interfere with the measurement. For example, the mirrors must be carefully suspended so they can move under the gravitational wave and isolate them from external vibrations. In addition, the laser beam must be carefully controlled to ensure that it remains stable.

When a gravitational wave passes through the interferometer, it exerts a tidal force which gives a movement to the mirrors and causes the lengths of the two arms to change slightly. This change in length causes a corresponding change in the interference pattern that is observed at the point of recombination. By carefully analyzing the interference pattern, one can detect and measure the strain of the gravitational wave. The signal produced by a gravitational wave is extremely small, typically less than one thousandth of the diameter of a proton. This requires using sophisticated data analysis techniques to separate the signal from the noise.

In the following decades the community constructed more detectors using interferometric methods with increased sensitivity [136, 137]. In 1985, a German group from Garching proposed at the Marcel Grossmann Meeting in Rome the first full-sized interferometer with a length of 3 km [138]. A year later, a Scotish group designed the

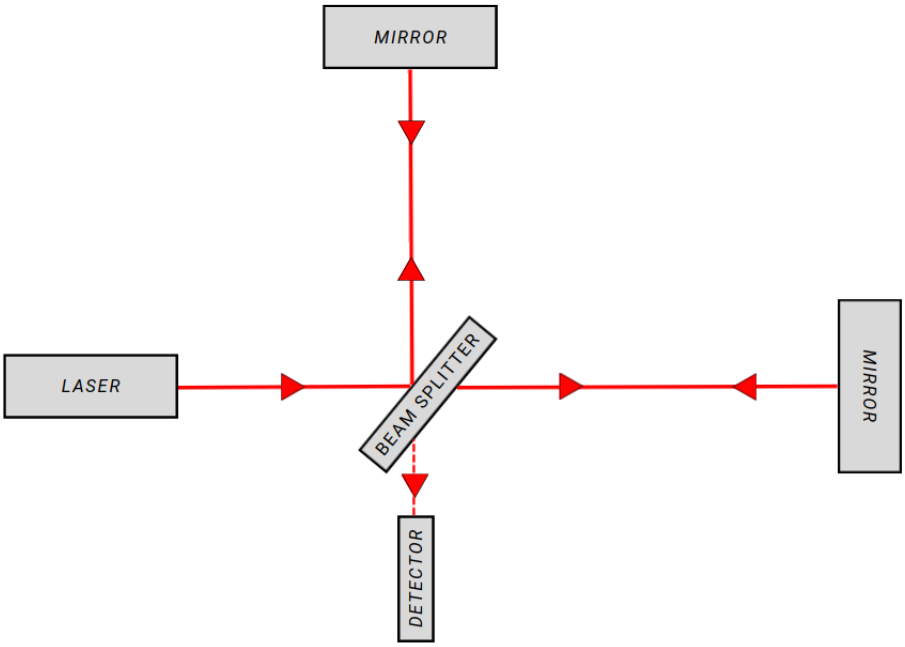


Figure 7.5: The light path through a basic interferometer. If there is a difference in length between the two arms due to, for example, the effect of a gravitational wave, a different interference pattern is observed at the detector.

first Long Baseline Gravitational Wave Observatory [139]. Later on, these two groups started a collaboration that culminated in the construction in 1995 of GEO600, an interferometer with arms of 600 m in length.

On the other hand, the French wanted to start their own project of gravitational wave detectors. In 1983 they proposed the idea for the Virgo interferometer [140], named for the large cluster of galaxies. After some funding issues at the beginning, in 1993 the project was approved with funding provided by the Italian National Institute for Nuclear Physics (INFN) and the French National Centre for Scientific Research (CNRS). The interferometer was built near the town of Cascina, in the Tuscany region of Italy. The construction of Virgo was not without its challenges. The interferometer was originally designed to be 6-kilometer long, but difficulties in acquiring land for the detector meant that the length had to be reduced to 3 kilometers. Additionally, there were technical challenges in building the detector itself, including the need to achieve ultra-high vacuum conditions inside the interferometer tubes in order to minimize interference from air molecules. Despite these challenges, Virgo was completed in 2003 and began its first observational run in 2007. The detector underwent a major upgrade between 2011 and 2017, which improved its sensitivity by a factor of ten.

On the other side of the Atlantic, in 1967 at the Massachusetts Institute of Technology (MIT) and soon after Gertsenshtein and Pustovoit suggested to use laser interferometry, Rainer Weiss implemented that idea and proposed the Laser

Interferometer Gravitational-Wave Observatory (LIGO) [141]. However, it took several decades for the technology and funding to become available to build such a detector. Construction of the first LIGO detector began in 1994, with funding from the National Science Foundation (NSF) and other international partners. The detector was built in Livingston, Louisiana, and was based on a design called the Michelson interferometer, which splits a laser beam into two perpendicular beams and measures changes in the interference pattern when the beams are recombined. The construction of LIGO was a massive undertaking that involved many technical challenges. One of the most significant challenges was achieving ultra-high vacuum conditions inside the interferometer tubes, which were 4-kilometer long, in order to minimize interference from air molecules. Another challenge was the need to isolate the detector from sources of noise, such as seismic vibrations from nearby roads and railroads. Despite these challenges, the first LIGO detector began operating in 2002, and its first observational run began in 2005. The detector was upgraded between 2008 and 2010 to improve its sensitivity, and a second detector was built in Hanford, Washington, which began operating in 2015.

## 7.5 GW150914: The first detection

Gravitational waves were not detected during the period when the first LIGO was operational, from 2002 to 2010. However, on September 14, 2015, at 5:51 a.m. Eastern Daylight Time, both LIGO detectors observed a signal [74] with a time difference of 7 milliseconds that lasted about a fifth of a second (fig. 7.6[4]). The signal matched the predicted waveform of gravitational waves generated by the merger of two black holes of around 36 and 29 solar masses into a single, more massive black hole located 1.3 billion light-years away (fig. 7.7).

During the inspiral and merger of the binary system, an enormous amount of energy was released in the form of gravitational waves. The total energy emitted was equivalent to $3M_\odot\, c^2$. At its peak, the power radiated as gravitational waves was greater than the combined power of all the light emitted by all stars in the observable universe. The probability of the signal being a random fluctuation in the detectors' noise was calculated to be less than $6 \cdot 10^{-7}$. The gravitational-wave event was named GW150914, from the date of observation.

After the first observation of gravitational waves, the LIGO/Virgo collaboration reported the detection of other binary black hole merger events. Nonetheless, on August 17, 2017, the LIGO and Virgo detectors observed a signal that was unique from previous detections because it was caused by the merger of two neutron stars [142]. The signal was also observed in the electromagnetic spectrum by several telescopes around the world, marking the first time that a cosmic event was observed in both gravitational waves and light. Just like the first detection, the event, which last 100

[4] `https://www.gravitational wave-openscience.org/events/gravitational wave150914/P150914`

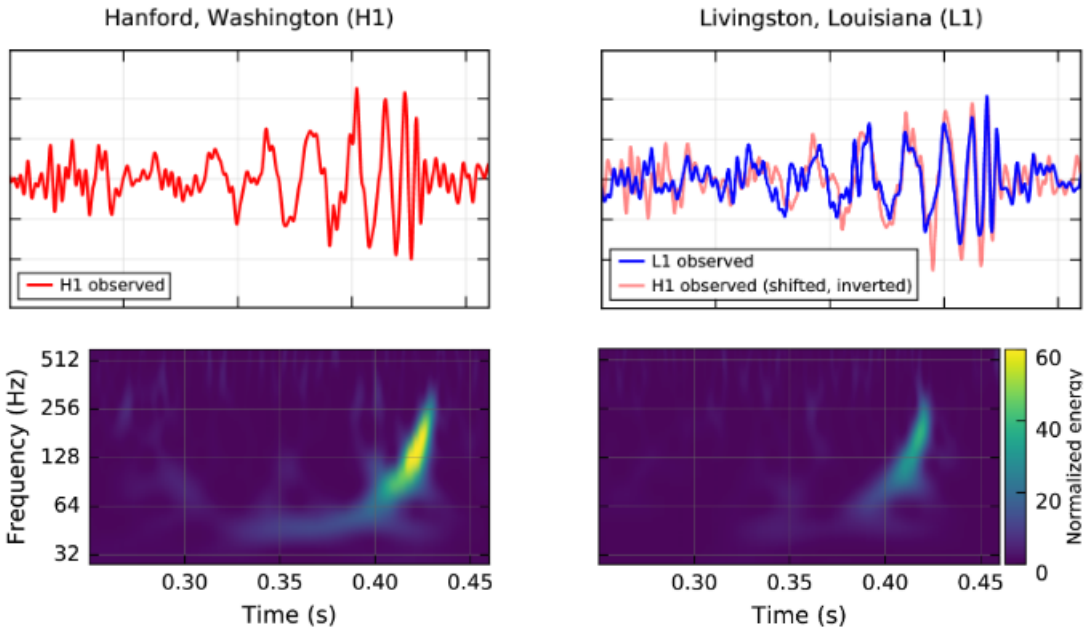


Figure 7.6: GW150914 observed by the LIGO Hanford (H1) and Livingston (L1) detectors. *Top*: Strain of the signal. For comparison, the H1 signal is shown in the L1 signal shifted in time of arrival and inverted. *Bottom*: Time-frequency representation of the energy associated with GW150914. Credit to the Gravitational Wave Open Science Center.

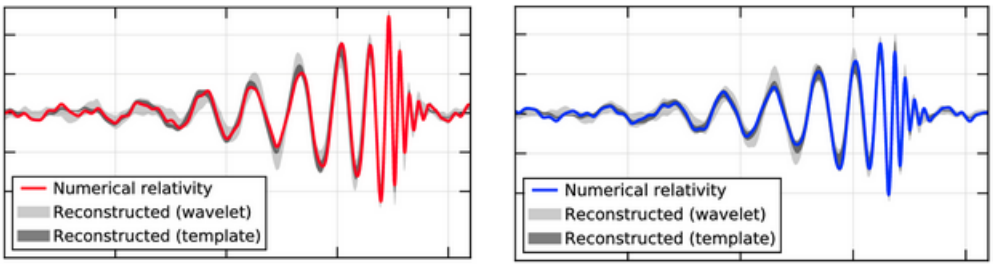


Figure 7.7: Reconstructed waveform of GW150914 by H1 (left) and L1 (right) compared to the predictions of General Relativity. Shaded areas show 90% credible regions. Credit to the Gravitational Wave Open Science Center.

seconds, was named GW170817 and occurred about 130 million light-years away in the galaxy NGC 4993. The merging of the two neutron stars generated a burst of gravitational waves and a kilonova.

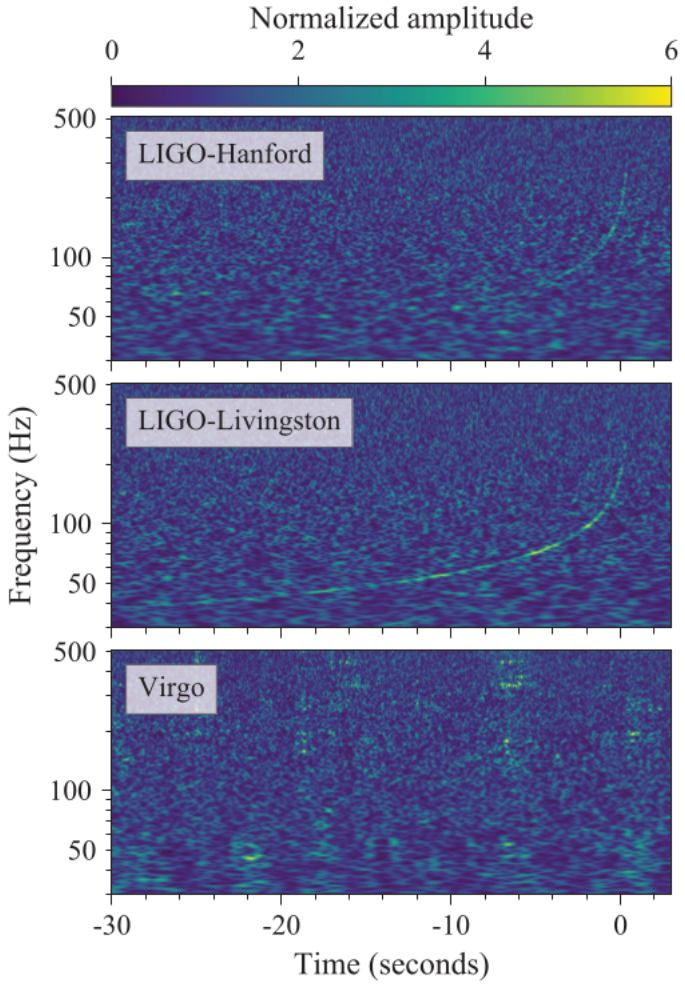


Figure 7.8: A time-frequency decomposition of the energy associated with GW170817. The Virgo detector did not capture any visible data of the event due to its relatively lower sensitivity compared to the other detectors. Credit to ref. [142]

The detection of GW170817 (fig. 7.8) and the observation of its subsequent electromagnetic counterpart marked a major breakthrough in multi-messenger astronomy, which involves studying the universe using multiple forms of radiation, including gravitational waves, light, and cosmic rays. The gamma-ray burst detected by the Fermi and INTEGRAL spacecraft began only 1.7 seconds after the gravitational wave merger signal. As a result, GW170817 set a constraint on the propagation speed of gravitational waves, $|c_{\rm GW}/c - 1| \lesssim 10^{-15}$, leading to a crucial evidence: *gravitational waves propagate at the speed of light*. This result corroborated therefore the predictions of Heaviside, Poincaré and Einstein, and confirmed the analogy between gravity and light.

## 7.6 Other gravitational wave observatories

As of March 2023, there have been more than 20 detections and there are more than 90 candidates. The observations are conducted in a series of "runs", with three completed so far, during which the detectors undergo maintenance and upgrades. The first run, referred to as O1, took place from September 12, 2015 to January 19, 2016, while O2 took place from November 30, 2016 to August 25, 2017 [143]. O3 commenced on April 1, 2019 and was divided into two parts: O3a, from April 1 to September 30, 2019, and O3b, from November 1, 2019 to March 27, 2020 [144, 145, 146]. The suspension of observation during October 2019 was for upgrades and repairs to the equipment, while cessation in March 2020 was due to the COVID-19 pandemic. The fourth run, O4, is planned to start in May 2023[5]. O5 observing period is expected to last until 2028.

Besides the LIGO and Virgo detectors, there is another large interferometer designed to detect gravitational waves that will join the LIGO/Virgo collaboration in the next observation run (O4) and whose first observation run ended on April 21, 2020. The Kamioka Gravitational Wave Detector (KAGRA) [147] is a gravitational wave observatory located in Japan. It is designed to detect gravitational waves in the frequency range of 10 to $10^4$ Hz. KAGRA uses a cryogenic system to cool its mirrors to near absolute zero, which reduces thermal noise and improves its sensitivity to gravitational waves. KAGRA is expected to become fully operational in the coming years.

Furthermore, there are several proposed gravitational wave observatories, each with its own unique characteristics and capabilities. Together they aim to create a network of interferometers that would allow to observe gravitational waves regardless of the sky location. Here's an overview of them.

- *IndIGO (LIGO-India)*: The IndIGO (Indian Initiative in Gravitational-wave Observations) is a collaborative project between several Indian research institutions to build and operate gravitational wave observatories in India. Currently, there are two IndIGO observatories under construction, located in Hingoli and Hanle. The observatories are expected to be completed in the next few years and will join other gravitational wave observatories [148].

- *Cosmic Explorer*: Cosmic Explorer is planned to be an underground facility consisting of multiple interferometers whose arms would be 40 km long, several times longer than those of LIGO and Virgo. The longer arms would allow Cosmic Explorer to detect gravitational waves from much farther away and with greater sensitivity, potentially detecting hundreds or thousands of events per year.

[5] `https://www.ligo.caltech.edu/page/observing-plans`

- *Einstein Telescope*: The Einstein Telescope is a proposed gravitational wave observatory that will be built in Europe. It will consist of three nested detectors, each with arms 10-kilometer long, arranged in an equilateral triangle. The Einstein Telescope will be designed to detect gravitational waves in the frequency range of 0.1 to $10^4$ Hz, which is a range that has not been extensively explored by other gravitational wave observatories. The detector will be built underground, to diminish seismic noise. The project is still in the planning stages and is expected to be completed in the late 2030s or early 2040s.

- *LISA*: The Laser Interferometer Space Antenna (LISA) is a planned gravitational wave observatory that will consist of three spacecraft in a triangular formation, separated by millions of kilometers. LISA will detect gravitational waves in the low-frequency range of 0.1 mHz to 1 Hz, which is too low for ground-based observatories like LIGO and Virgo to detect. LISA is expected to be launched by the European Space Agency in 2037. On December 3, 2015 the European Space Agency (ESA) launched LISA Pathfinder, a spacecraft whose mission was to test the technologies needed for LISA. The mission demonstrated that the LISA operation is feasible.

It is worth mentioning that there is a plan to improve the sensitivity of the existing LIGO detectors by a factor of two, and lower the low-frequency cutoff to 10 Hz with a third-generation detector, named "LIGO Voyager". Voyager, which would be an upgrade to A+, is planned to be operational around 2027–2028.

## 7.7 Lensing of gravitational waves

As mentioned in the previous section, there is a direct connection between gravity and light due to the similarities between gravitational and electromagnetic waves. As a result, just like light, gravitational waves can also be deflected due to the gravitational field of a mass, suffering therefore, gravitational lensing. This idea was first proposed in 1971 by J.K. Lawrence [149]. He studied the gravitational radiation observed by Weber and concluded that it is focused by the galactic core acting as a gravitational lens. In 1974, Hans C. Ohanian [150] investigated the gain in intensity that can be achieved by the gravitational radiation by using a massive object as a lens.

However, gravitational and electromagnetic waves present important differences. While geometric optics is a valid approximation to treat the propagation of light [151, 152, 88], it might not be the case for gravitational waves, since the wavelength is comparable to the size of the lens [153]. Consequently, a full wave optics analysis is needed [154, 155, 156, 157].

Just like electromagnetic waves, lensing can manifest itself in different regimes. When a gravitational wave passes by a lens with a smaller impact parameter than its Einstein radius, the lens can produce multiple images and strong lensing effects. If the detector is sensitive enough, the two images appear as two independent

gravitational wave sources with different amplitudes and arrival times. Some approaches [158, 159, 160] consider that this effect results in a magnification of the waveform leading to a change in the inferred luminosity distances.

However, when the gravitational wave travels through a region of compact objects, microlensing effects may arise. References [156, 161] study the microlensing of stellar-mass objects. References [162, 163] investigate the effect of those microlenses embedded in galaxy or cluster and conclude that they would produce interference distortions in the observed strains and therefore microlensing would become increasingly significant. Reference [164] mix strong and microlensing to enhance the inference of the microlensing effects. Some authors also study the microlensing effects from a phenomenological approach [165].

As it happens with light, if a significant fraction of dark matter is in the form of compact objects like primordial black holes, there can be microlensing effects in the gravitational wave signal [166, 167, 168, 169] and can be observable by LIGO and Virgo. Lensing of gravitational waves is therefore a good observable and a powerful method to constrain the abundance of compact objects.

The motivation of the second part of this thesis is to explore this method further from the theoretical perspective. In particular, the aim is to study the gravitational lensing of gravitational waves through a region of compact objects and obtain an expected rate of observed lensed events. To do so, we study the scales in which wave optics effects are relevant and detectable and we model the lensing probability in different scenarios. The remainder of Part II is organised as follows. In chapter 8, we review the theory of lensing of gravitational waves and study its different regimes. In chapter 9 we explore the relevant scales for lensing detection. We use the results to model the probability of lensed signals in a more realistic universe with dark matter halos filled with compact objects in chapter 10 and compute the predictions in chapter 11. We conclude in chapter 12.

CHAPTER

# EIGHT

# SCALES OF LENSING OF GRAVITATIONAL WAVES

In this chapter we review the theory of lensing of gravitational wave and study its different regimes. In particular, we use the wave optics approximation to derive the amplification factor from the diffraction integral and apply the result to the particular case of a point lens and a singular isothermal sphere. Furthermore we explore the geometric optics limit of the lens and conclude with the different regimes in which lensing can manifest itself.

Gravitational waves are solutions of the Einstein's field equations that are obtained using the "linearized gravity" approximation. Let us assume that the spacetime metric can be decomposed into

$$g_{\mu\nu} = \bar{g}_{\mu\nu} + h_{\mu\nu} \ , \qquad |h_{\mu\nu}| \ll 1 \tag{8.1}$$

where $\bar{g}_{\mu\nu}$ represents a general background metric and $h_{\mu\nu}$ the amplitude of the fluctuations that constitute the gravitational wave. In the remainder of this part, a subscript with a comma denotes the coordinate partial derivative, semicolons refer to background covariant derivatives, $\bar{\nabla}_\mu$, and $\bar{\Box} \equiv \bar{\nabla}^\mu \bar{\nabla}_\mu = \bar{g}^{\mu\nu}\bar{\nabla}_\nu\bar{\nabla}_\mu$ is the D'Alembert operator of the background metric. The linearized limit and the gauge invariances lead us to the propagation equation in vacuum (see sec. 5.4 in [170] for the complete derivation)

$$\bar{\Box}\gamma_{\mu\nu} + 2\bar{R}_{\alpha\mu\beta\nu}\gamma^{\alpha\beta} = 0 \tag{8.2}$$

where $\bar{R}_{\alpha\mu\beta\nu}$ is the Riemann curvature tensor of the background metric and

$$\gamma_{\mu\nu} \equiv h_{\mu\nu} - \frac{1}{2}h\bar{g}_{\mu\nu} \tag{8.3}$$

with $h \equiv h^\mu_\mu = \bar{g}^{\mu\nu}h_{\mu\nu}$.

In the framework of the eikonal approximation, the typical wavelength of the gravitational wave is much smaller than the curvature radius of the background and much smaller than the typical scale in which the amplitude evolves. In this regime,

the second term in eq. (8.2) vanishes and the propagation equation can be turned into a wave equation [171]

$$\bar{\Box}h_{\mu\nu} = 2h_{\rho(\mu;\nu)} - h_{\mu\nu;\rho} \tag{8.4}$$

where the brackets indicate the indices being symmetrized. Let us now introduce the wave-ansatz

$$h_{\mu\nu} = H_{\mu\nu}e^{i\phi} + \text{c.c.} \tag{8.5}$$

where $H_{\mu\nu}$ is the complex amplitude and polarization of the gravitational wave and $\phi$ its phase, which includes information about the spin and the masses of the source, and c.c. means complex conjugate. Inserting the wave-ansatz into 8.4 we obtain

$$\bar{\Box}h_{\mu\nu} = (-k^\rho k_\rho H_{\mu\nu} + i\mathcal{D}H_{\mu\nu} + \Box H_{\mu\nu})e^{i\phi} + \text{c.c.} \tag{8.6}$$

where $k_\mu \equiv \phi_{i\mu}$ is the wave four-vector, and $\mathcal{D}$ is a differential operator defined as

$$\mathcal{D} \equiv 2k^\mu \bar{\nabla}_\mu + k^\mu_{;\mu}. \tag{8.7}$$

By taking the real part of eq. (8.6) we get the dispersion relation

$$k^\mu k_\mu = 0 \tag{8.8}$$

which shows, as mentioned in the introduction, that gravitational waves propagate at the speed of light. Finally, if we take the gradient of the dispersion relation we obtain the geodesic equation

$$k^\mu k_{\nu;\mu} = 0. \tag{8.9}$$

which implies that, just like light, gravitational waves propagate along null geodesics. This means that everything that we know about light can be applied to gravitational waves. As a result, *gravitational waves can also experience gravitational lensing.*

Let us now compute the solution of $h_{\mu\nu}$ for a gravitational wave propagating in the $z$-direction, which takes the form, over a basis that is parallel transported along the geodesic

$$h_{\mu\nu} = \begin{bmatrix} 0 & 0 & 0 & 0 \\ 0 & h_+ & h_\times & 0 \\ 0 & h_\times & h_+ & 0 \\ 0 & 0 & 0 & 0 \end{bmatrix} \tag{8.10}$$

where $h_+$ and $h_\times$ are the two transverse polarization modes known as the plus (+) and cross (×) tensor modes. These two tensors are parallel transported. Gravitational waves are therefore purely tensor polarized. The $h_+$ polarization mode acts like a gravitational force in the $x$ and $y$ direction and $h_\times$, diagonally. The general wave is a linear combination of the two polarization modes. In the propagation basis they read

$$h_+(t) = \frac{h_0(t)}{2}(1 + \cos^2\iota)\ \cos\left[\phi(t) + \phi_0\right] \tag{8.11}$$

$$h_\times(t) = h_0(t)\cos\iota\ \sin\left[\phi(t) + \phi_0\right] \tag{8.12}$$

where $\iota$ is the polar inclination angle, i.e., the angle between the axis of rotation of the binary and the line of sight, $\phi_0$ is the phase at the moment of emission of the gravitational wave and

$$h_0(t) = \frac{[2\mathcal{M}_z^5\,\omega_0^2(t)]^{1/3}}{(1+z)^2 D_{\rm A}} \tag{8.13}$$

is the time dependent amplitude of the gravitational wave. $D_{\rm A}$ is the angular diameter distance in the background metric, $\omega_0(t)$ is the observed cyclic frequency of the gravitational wave and $\mathcal{M}_z$ is the redshifted chirp mass of the binary system that produces the gravitational wave, defined at leading order for a quasi-circular inspiral, as

$$\mathcal{M}_z = (1+z)\frac{(m_1 m_2)^{3/5}}{(m_1+m_2)^{1/5}} \tag{8.14}$$

where $m_1$ and $m_2$ are the masses of the binary.

## 8.1 Diffraction integral and wave optics

Now, let us consider the situation depicted in fig. 8.1. A source of gravitational waves at $z_{\rm s}$ is observed through an inhomogeneous universe. As mentioned in Part I, $D_{\rm os}, D_{\rm od}$ and $D_{\rm ds}$ correspond to the angular diameter distance from the observer to the source, from the observer to the lens and from the lens to the source respectively. The line of sight is conventionally set as the direction in which the main lens is observed. With respect to that origin, we denote $\boldsymbol{\beta}$ the unlensed position of the source and $\boldsymbol{\theta}$ the observed position of an image of the source. Since $D_{\rm os}, D_{\rm od}$ and $D_{\rm ds}$ are very large

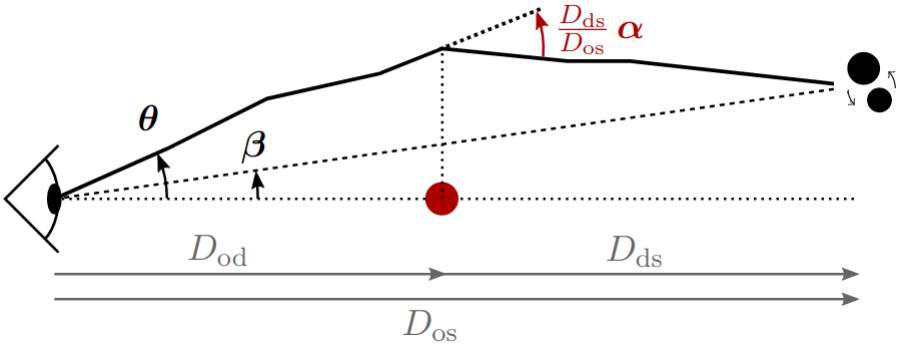


Figure 8.1: Schematic representation of the quantities involved in the time delay

compared to the typical size of a lens, we can use the thin lens approximation in which lensing occurs in the plane of the main lens. In this regime the time delay between the lensed and unlensed path at a given $\boldsymbol{\theta}$ is determined by:

$$t_{\rm d}(\boldsymbol{\theta},\boldsymbol{\beta}) \approx \frac{1}{c}\frac{D_{\rm od}D_{\rm os}}{2D_{\rm ds}}|\boldsymbol{\theta}-\boldsymbol{\beta}|^2 + t_\Phi(\boldsymbol{\theta}) \tag{8.15}$$

The first term of the equation is the geometric time delay, which is the different amount of time that light rays take to reach the observer from different path lengths,

and $t_\Phi$ is the Shapiro time delay from traversing a lensed path $s$ through different values of the gravitational potential of the lens [172]

$$t_\Phi \approx -\frac{2}{c^3}\int \Phi \, \mathrm{d}s \tag{8.16}$$

In the remainder it is useful to work in units of the redshifted Einstein radius of a lens of mass $M_\mathrm{L}$ at redshift $z_\mathrm{L}$

$$\theta_\mathrm{E} \equiv \sqrt{\frac{4GM_\mathrm{L}(1+z_\mathrm{L})D_\mathrm{ds}}{c^2 D_\mathrm{os} D_\mathrm{od}}} \tag{8.17}$$

and time delays in units of the dilated Schwarzschild diameter crossing time

$$t_\mathrm{M} = 4GM_\mathrm{L}(1+z_\mathrm{L})/c^3. \tag{8.18}$$

With these units we can express the dimensionless position of the source and the image

$$\boldsymbol{x} \equiv \frac{\boldsymbol{\theta}}{\theta_\mathrm{E}}, \quad \boldsymbol{y} \equiv \frac{\boldsymbol{\beta}}{\theta_\mathrm{E}} \tag{8.19}$$

and the dimensionless time delay and frequency

$$T_\mathrm{d} \equiv \frac{t_\mathrm{d}}{t_\mathrm{M}}, \quad w \equiv t_\mathrm{M}\omega \tag{8.20}$$

where $\omega = 2\pi f$. We have oriented the source at $\alpha = 0$ in the polar coordinates $(x, \alpha)$ of the transverse plane.

Suppose that the wavelength of the gravitational wave $\lambda$ is comparable to the path difference between the signals emitted at the same time. In that case, diffraction effects become relevant and lensing has to be treated in the wave optics regime. In that case, there is only one image formed from the superposition of all paths. If we write the dimensionless frequency as a function of the Schwarzschild radius of the lens $R_\mathrm{s}$ [173]

$$w = \frac{4\pi R_\mathrm{s}(1+z_\mathrm{L})}{\lambda} \tag{8.21}$$

we obtain a handy condition to use the wave optics approximation,

$$w < 2\pi \tag{8.22}$$

i.e., if the wavelength of the gravitational wave is comparable to the Schwarzschild radius of the lens ($\lambda > R_\mathrm{s}$), the wave optics treatment is necessary.

Let us denote the amplitude of the unlensed gravitational wave [$h_0$ in eq. (8.11) and eq. (8.12)] in frequency domain by $h(f, \boldsymbol{\beta})$. Lensing effects in the waveform can be described in terms of the amplification factor $F$

$$h_\mathrm{L}(f, \boldsymbol{\beta}) = F(f, \boldsymbol{\beta}) h(f, \boldsymbol{\beta}) \tag{8.23}$$

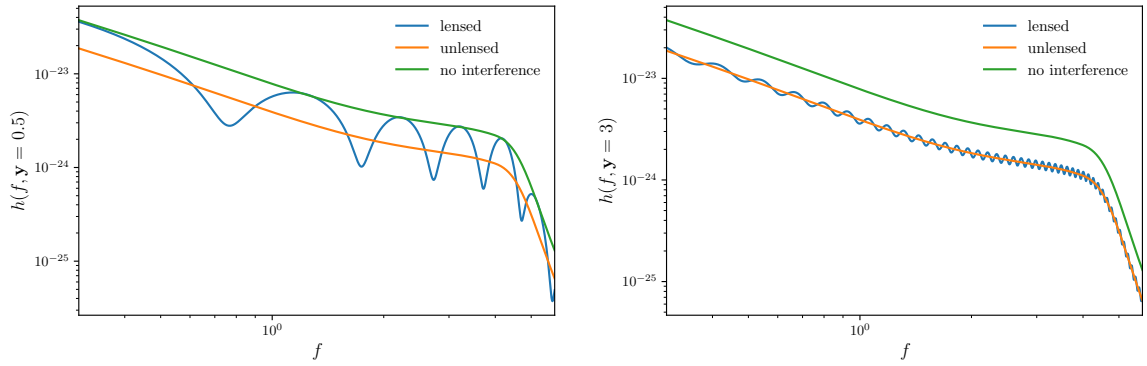


Figure 8.2: Amplitude of a lensed (blue) and unlensed (orange) waveform in frequency domain. We also show the amplitude of a gravitational wave that has been only amplified. The gravitational wave is sourced by a non-rotating compact binary at $z_{\rm s} = 1.0$ and $\boldsymbol{y} = 0.5$ (left) and $\boldsymbol{y} = 3$ (right) with $m_1 = m_2 = 30M_\odot$, $q = m_1/m_2 = 1$ and the lens is a point mass of $M_{\rm L} = 10^3 M_\odot$ located at $z_{\rm L} = 0.2$. When we move far away from the lens (increasing $\boldsymbol{y}$), the interference is very small and the lensed and unlensed signal are practically indistinguishable.

where $h_{\rm L}(f, \boldsymbol{\beta})$ is the observed lensed waveform and $f$, its frequency. This frequency-dependent amplification of the waveform is the main difference with respect to electromagnetic waves (fig. 8.2).

If the time delay is known, one can obtain the amplification factor in the thin lens approximation by solving the diffraction integral [88]

$$F(f, \boldsymbol{\beta}) = \frac{D_{\rm od} D_{\rm os}}{D_{\rm ds}} \frac{1}{c} \frac{f}{i} \int \mathrm{d}^2\theta \; e^{2\pi i f \, t_d(\boldsymbol{\theta}, \boldsymbol{\beta})} \tag{8.24}$$

The observed waveform in time domain is therefore

$$h_{\rm L}(t, \boldsymbol{\beta}) = \int \mathrm{d}f \; e^{-2\pi i f t} F(f, \boldsymbol{\beta}) h(f, \boldsymbol{\beta}) \tag{8.25}$$

Here, $h(f, \boldsymbol{\beta})$ is the Fourier transform of the temporal profile of the unlensed waveform $h(t, \boldsymbol{\beta})$.

## 8.2 Point lens

In this section we compute the time delay produced by a point lens and obtain the diffraction integral. The point lens approximation is also valid for extended lenses whose size is much smaller than its Einstein radius. In the Born approximation the Shapiro time delay reads

$$t_\Phi \approx -\frac{t_{\rm M}}{2} \ln \frac{\sqrt{D_{\rm ds}^2 + b^2} - D_{\rm ds}}{\sqrt{D_{\rm od}^2 + b^2} + D_{\rm od}} \tag{8.26}$$

where $b$ is the impact parameter, which corresponds at lowest order to the minimal distance between the gravitational wave and the mass of the lens in the trajectory. If $\theta \ll 1$, we can approximate $b \approx \theta D_{\rm od}$. Assuming that $D_{\rm ds}$ and $D_{\rm od}$ are on the same order of magnitude the Shapiro time delay can be approximated as

$$t_\Phi \approx -t_{\rm M} \ln\theta + \text{const.} \tag{8.27}$$

Including the geometric term, the dimensionless time delay becomes

$$T_{\rm d} = \frac{1}{2}[(x\cos\alpha - y)^2 + x^2\sin^2\alpha] - \ln x - \ln\theta_{\rm E} \tag{8.28}$$

where $x \equiv |\boldsymbol{x}|$ and $y \equiv |\boldsymbol{y}|$. Inserting the above equation into eq. (8.24) we obtain the amplification factor for a point mass lens [174]

$$F(w,\boldsymbol{y}) = \frac{w}{2\pi i}\int_0^\infty x\,\mathrm{d}x \int_0^{2\pi}\mathrm{d}\alpha\, e^{iwT_{\rm d}} = \nu^{1-\nu}e^{2\nu\ln\theta_{\rm E}}\Gamma(\nu)L_\nu(-\nu y^2) \tag{8.29}$$

where $\nu \equiv -iw/2$ and $L_n(z)$ is the Laguerre polynomial.

## 8.3 Singular isothermal sphere

The singular isothermal sphere (SIS) is the simplest and most used galaxy halo profile to fit to the lensing signal. The density profile is given by

$$\rho(r) = \frac{\sigma_{\rm v}^2}{2\pi G r^2} \tag{8.30}$$

whose surface density is characterized by their velocity dispersion $\sigma_{\rm v}$. In that case the amplification factor (eq. (8.24)) can be expressed as [173]

$$F(w,\boldsymbol{y}) = \frac{w}{2\pi i}e^{iwy^2/2}\int_0^\infty \mathrm{d}x\; xJ_0(wxy)\exp\;\; iw\;\; \frac{1}{2}x^2 - \psi(x) + \phi_m(y) \tag{8.31}$$

where $J_0$ is the Bessel function of zeroth order, $\psi(x) = x$ is the lensing potential and $\phi_m(y) = y + 1/2$ is the phase for the minimum time delay. Equation (8.31) is valid for any axially symmetric lensing object and in our case can be analytically solved [175]

$$F(w,\boldsymbol{y}) = e^{\frac{i}{2}w(y^2+2\phi_m(y))}\sum_{n=0}^\infty \frac{\Gamma\;\; 1+\frac{n}{2}}{n!}\;\; 2we^{i\frac{3\pi}{2}}\;\;^{n/2}{}_1F_1\;\; 1+\frac{n}{2},1;-\frac{i}{2}wy^2 \tag{8.32}$$

where we have Taylor-expanded the second term of the exponential into an infinite sum and used that $e^z{}_1F_1(a,b;-z) = {}_1F_1(a,b;z)$ [176].

## 8.4 Geometric optics approximation

Now suppose that the wavelength of the gravitational wave is much smaller than the Schwarzschild radius of the lens ($\lambda \ll R_{\rm s}$). In that case, we will see that lensing is strong enough to produce two distinct bright images, which can be viewed as the stationary phase points of the integral path according to Fermat's principle. This is called the stationary phase approximation or, more popularly, the geometric optics approximation. In that case, one can resolve the distinct images due to the lack of diffraction. In general, this approximation is valid when the time delay between stationary paths is much greater than the inverse frequency of the wave.

In geometric optics we obtain the amplification factor by calculating the contribution from the $j$-th image. We start by Taylor-expanding the time delay at the quadratic level[1]

$$t_{\rm d}(\boldsymbol{\theta}) \approx t_{\rm d}(\boldsymbol{\theta}_j) + \frac{1}{2}\sum_{(a,b)=1}^{2} \delta\theta_a \delta\theta_b \partial_a \partial_b t_{\rm d}(\boldsymbol{\theta}_j) \tag{8.33}$$

where the $j$-image is located at $\boldsymbol{\theta}_j$ and $\delta\boldsymbol{\theta} = (\boldsymbol{\theta} - \boldsymbol{\theta}_j)$. In the diagonalized basis the amplification factor reads

$$F \approx \frac{D_{\rm od} D_{\rm os}}{D_{\rm ds}} \frac{1}{c} \frac{f}{i} \sum_j e^{2\pi i f t_{\rm d}(\boldsymbol{\theta}_j)} \int {\rm d}\bar{\theta}\ \exp\ \pi i f (\bar{\theta}_1^2 \lambda_{1j} + \bar{\theta}_2^2 \lambda_{2j}) \frac{D_{\rm od} D_{\rm os}}{c D_{\rm ds}} \tag{8.34}$$

where $\lambda_{1,2}$ are the two eigenvalues for each image. Using that $\int_{-\infty}^{\infty} {\rm d}x\ e^{ix^2} = \sqrt{\pi} e^{i\pi/4}$ we obtain the final expression for the amplification factor.

$$F \approx \sum_j \overline{|\mu(\boldsymbol{\theta}_j)|}\ \exp\ 2\pi i f t_{\rm d}(\boldsymbol{\theta}_j) - {\rm sign}(f)\frac{n_j \pi}{2} \tag{8.35}$$

where $\mu(\boldsymbol{\theta}_j)$ is the $j$-th image magnification and $n_j = [0, 1, 2]$ when $\boldsymbol{\theta}_j$ is a minimum, saddle or maximum point of $t_{\rm d}$ respectively. For $n_j = k$ the light bundles cross $k$ caustics and the images are said to be of type I, II and III respectively.

A point mass lens forms two images whose magnification are

$$\mu_\pm = \frac{1}{2} \pm \frac{y^2 + 2}{2y\sqrt{y^2 + 4}} \tag{8.36}$$

so the amplification factor reads

$$F(w, \boldsymbol{y}) = |\mu_+|^{1/2} - i|\mu_-|^{1/2} e^{iwt_{\rm d}} \tag{8.37}$$

For a SIS, the number of images that the lens forms depend on the position of the source. If $y < 1$ the lens forms double images while only a single image is formed if

[1] This is valid when we use the stationary phase approximation since $|2\pi f \Delta t_{\rm d}| \gg 1$, where $\Delta t_{\rm d}$ is the time delay between stationary points, i.e., between the multiple images.

$y \geq 1$. Taking the limit of $w \gg 1$ the amplification factor in the geometric optics approximation is

$$F(w, \boldsymbol{y}) = \begin{cases} |\mu_+^{\mathrm{S}}|^{1/2} - i|\mu_-^{\mathrm{S}}|^{1/2} e^{iwt_{\mathrm{d}}} & y < 1 \\ |\mu_+^{\mathrm{S}}|^{1/2} & y \geq 1 \end{cases}$$

where $\mu_\pm^{\mathrm{S}} = 1/y \pm 1$ are the partial amplifications of the two images produced by a SIS. It behaves like a point mass lens for $y < 1$ in the geometric optics regime.

In fig. 8.3 we show the modulus of the amplification factor of a point mass lens for different positions of the source together with the geometric optics limit. For small values of $w$, the wavelength of the gravitational wave is much larger that the Schwarzschild radius of the lens and therefore diffraction effects are relevant. That is why the amplification is very small is that regime ($|F| \to 1$). One can also argue that the lens is so small compared to the wavelength of the gravitational wave that lensing is practically negligible. On the other hand for large values of $w$ the amplification

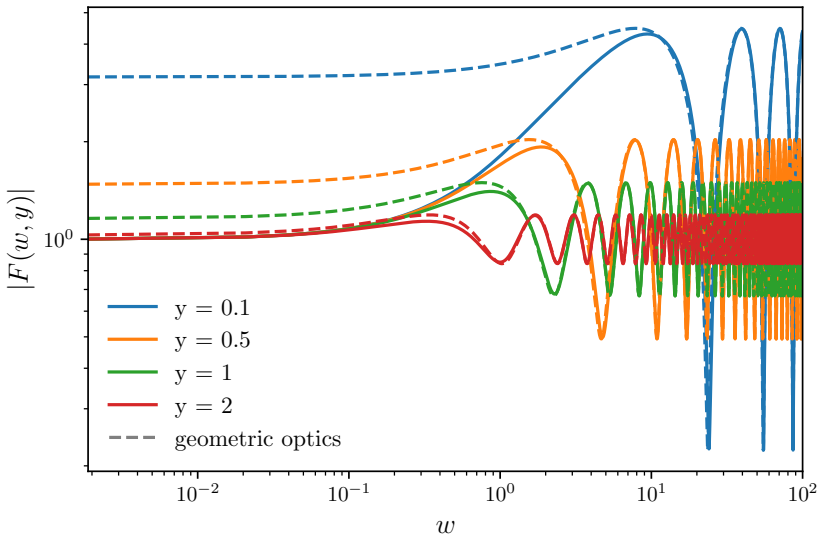


Figure 8.3: Amplification factor of a point mass lens for different values of the position of the source (solid line) and its geometric optics limit (dashed line). We can distinguish small amplifications for $w \ll 1$ and a oscillating behaviour for $w > 1$. One can also observe that for large values of the position of the source geometric optics is a good approximation regardless of the frequency of the waveform.

factor converges to the geometric optics limit

$$|F|^2 = |\mu_+| + |\mu_-| + 2|\mu_+\mu_-|^{1/2} \sin(wt_{\mathrm{d}}) \tag{8.38}$$

where $|\mu_-| = 0$ for $y \geq 1$ in the SIS. The first two terms define the total amplification while the third term represents the interference that we see in fig. 8.3 between the multiple images. From eq. (8.36) we see that the amplification decreases when $y$

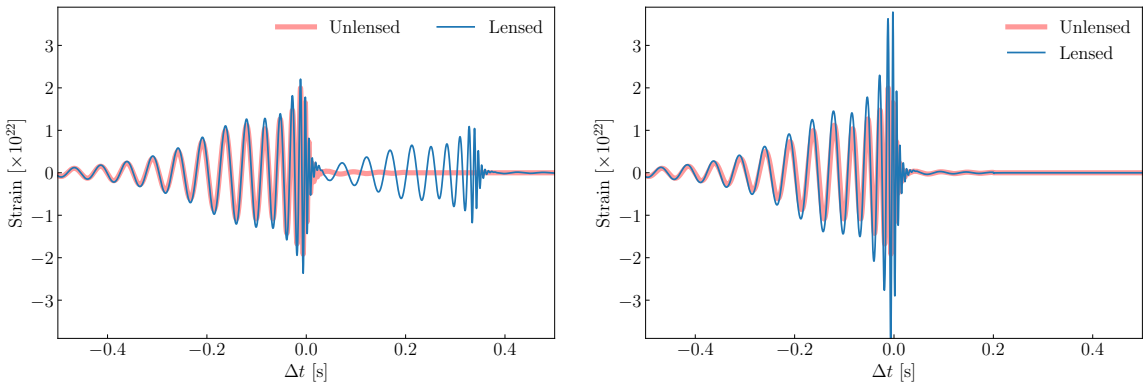


Figure 8.4: A gravitational wave from a pair of non-rotating merging black holes with masses $m_s = 30M_\odot$ and inclination $\iota = 0$ is lensed by a compact object. We set $t = 0$ as the time of arrival of the gravitational wave. The minimum frequency is 20Hz. *Left*: The mass of the lens is $M_\mathrm{L} = 10^4\ M_\odot$ and the impact parameter $b = 0.7\ \theta_\mathrm{E}$. In this case, the lens produces two distinct images. *Right*: The mass of the lens is $M_\mathrm{L} = 10^2\ M_\odot$ and the impact parameter $b = 0.3\ \theta_\mathrm{E}$. In this case, we can not distinguish between the two images and therefore, microlensing effects are relevant and leave an interference imprint in the waveform.

increases. That is why in fig. 8.3 the amplitude of the oscillation also decreases when increasing $y$. From the figure we can also anticipate that there is a critical position of the source, $y_\mathrm{c}$ from which geometric optics is a good approximation regardless of the frequency of the gravitational wave and the mass of the lens.

## 8.5 Strong lensing, microlensing and interference

As it happens with electromagnetic waves, when a gravitational wave passes by a lens with a smaller impact parameter than its Einstein radius, the lens can produce multiple images and strong lensing effects. If the detector is sensitive enough the two images appear as two independent gravitational wave sources with different amplitudes and arrival times (fig. 8.4). The waveform of the multiple images may have different phase shifts. In particular each additional caustic crossing would add a $-\pi/2$ shift [177].

Now let us imagine that a strongly lensed gravitational wave passes through a region of compact objects with masses of a few hundreds of solar masses. That is the case, for example, of a gravitational wave passing through a dark matter halo filled with primordial black holes (PBH). In that case, if the magnification due to strong lensing effects is large enough, then there is a non negligible change of microlensing. Microlensing effects leave an interference imprint in the lensed waveform. This means that one has to use a full wave-optics treatment when dealing with microlensing.

However, there can be a third scenario. Equation (8.38) shows that the geometric optics approximation allows for interference effects. Why do not we have such a regime with light? The answer is *coherence*. When the finite size of light sources and thin spectral extension is accounted for, the interference term is suppressed. However, the sources of gravitational waves are point-like and monochromatic in the spiral phase. As a result, applying this approximation and high frequencies in eq. (8.33) leave us with the extra term in eq. (8.38) of absolute coherence (interference).

Although some authors call this regime millilensing, it is not very clear in the literature. In order to have a more intuitive and well established notation, we propose to call this regime, the *absolutely coherent geometric optics*.

CHAPTER

# NINE

# DETECTING LENSING OF GRAVITATIONAL WAVES

In this section we explore the relevant scales for lensing and wave detection. In particular we investigate for which masses of the lens and impact parameters wave effects are relevant and detectable.

## 9.1 Template-based searches

We have seen in the previous section that lensing modifies the waveform of the unlensed signal through the frequency-dependent amplification factor. Is is therefore possible that we miss a signal in a gravitational wave observing run because its parameters are different from the ones we are looking for. To address this matter we set up an ensemble of templates in order to minimize the loss of a signal's signal-to-noise ratio (SNR), which is the filter that we use to analyze the matching of a lensed signal in a template search.

Let us suppose that our signal $s(t)$ is composed by a gravitational wave with amplitude $h(t)$ and a Gaussian noise $n(t)$

$$s(t) = h(t) + n(t) \tag{9.1}$$

The SNR of that signal with respect to a template $h_{\rm T}(t)$ is given by

$$\mathrm{SNR} = \frac{(s|h_{\rm T})}{\sqrt{(h_{\rm T}|h_{\rm T})}} \approx \frac{(h|h_{\rm T})}{\sqrt{(h_{\rm T}|h_{\rm T})}} \tag{9.2}$$

where we have assumed that the noise has a zero mean and we have defined the inner product of the data with the template as

$$(a|b) = 4\mathrm{Re}\left[\int_0^\infty \mathrm{d}f \frac{\tilde{a}(f)\tilde{b}^*(f)}{S_n(f)}\right] \tag{9.3}$$

where the functions are in Fourier space and $S_n(f)$ is the one-sided power spectral density. The optimal SNR is obtained when the signal matches the template $h \propto h_{\rm T}$, obtaining

$$\mathrm{SNR}_{\rm opt} = \quad \overline{(h|h)} \tag{9.4}$$

The SNR depends on the geometrical configuration of the binary, its luminosity distance and the redshifted chirp mass. It determines the detection threshold from which gravitational waves can be observed. We set this threshold for a single detector to be $\mathrm{SNR}_{\rm th} = 8$, which corresponds to the most distant coalescences that we can detect. Only sources with $\mathrm{SNR} > \mathrm{SNR}_{\rm th}$ will be detected.

For the remainder it is useful to determine how much the signal deviates from the template. We quantify this discrepancy with the parameter $\epsilon$ defined as

$$\epsilon = 1 - \frac{\mathrm{SNR}}{\mathrm{SNR}_{\rm opt}} \tag{9.5}$$

so $\epsilon \to 0$ when $h \to h_{\rm T}$.

In order to check the consistency of the lensed hypothesis on the signal template we use the $\Delta\chi^2$ test, defined as

$$\Delta\chi^2 = \chi^2_{\rm lensed} - \chi^2_{\rm unlensed}. \tag{9.6}$$

We consider that the detection of a lensed event is significant if the signal is above a $3\sigma$ interval from the unlensed model, which corresponds to $\Delta\chi^2 > 10$. The conditions for lensing detection are therefore

$$\mathrm{SNR} > \mathrm{SNR}_{\rm th}, \quad \Delta\chi^2 > X \tag{9.7}$$

with $\mathrm{SNR}_{\rm th} = 8$ and $X = 10$. $\Delta\chi^2$ can be obtained as a function of the SNR and $\epsilon$

$$\Delta\chi^2 = 2\epsilon\ \mathrm{SNR}^2 \tag{9.8}$$

from which we obtain the minimum value of $\epsilon$ for lensing detection if $\mathrm{SNR} = \mathrm{SNR}_{\rm th}$, i.e., $\epsilon_{\rm th} \simeq 0.08$.

## 9.2 Relevant scales for lensing detection

Here, we investigate the combination of masses of the lens, $M_{\rm L}$, and impact parameters, $b$, for which a lensed signal is detected. For that purpose, we use a lensed gravitational wave in the wave optics regime as our signal, $h$, and an unlensed waveform as our template, $h_{\rm T}$. In order to quantify the discrepancy between the signal and the template we show in fig. 9.1 a contour plot of $\epsilon$ as a function of the mass of the lens and the reduced impact parameter ($u \equiv b/\theta_{\rm E} \simeq y$), i.e., expressed in units of the lens' cross-sectional radius. We draw explicitly $\epsilon_{\rm th}$ (red contour line). For points that are within $\epsilon_{\rm th}$, lensing in the wave optics approximation is detectable. The source of

gravitational waves is a compact binary at $z_s = 1$ with $m_1 = m_2 = 30M_\odot$. In general, $\epsilon$ increases when decreasing $y$ since the lensing signal is very strong for small impact parameters ($F$ increases when $y$ decreases). For $M_L \lesssim 40M_\odot$ we do not detect any lensed signal independently of $y$, since $M_L$ is so small that the gravitational wave does not feel the presence of the lens. For $M_L \gtrsim 40M_\odot$, the detectability depends on the impact parameter. We call the reduced impact parameter in which $\epsilon = \epsilon_{th}$ the critical reduced impact parameter, $y_c$. For $40M_\odot \lesssim M_L \lesssim 100M_\odot$ $y_c$ increases with $M_L$. This is because $y$ decreases with $M_L$ (the Einstein radius increases) and therefore, the amplification factor increases (fig. 8.3). As a result, the SNR increases and the gravitational wave does not need to pass so close to the lens to be detectable. Finally for large masses of the lens ($M_L \gtrsim 200M_\odot$), a lensed signal is always observed as long as $y \lesssim 0.7$.

We observe that two islands appear in the contour plot of the detectability of lensing. We believe that their existence is due to the competition of the detectability of the gravitational wave, given by the SNR, and the lensing detectability, given by $\Delta\chi^2$. On the left island, which corresponds to small impact parameters and a big range of lens masses, the effect of lensing dominates. On the other hand, on the right island, which corresponds to larger impact parameters and lens masses, the signal of the gravitational wave dominates and it partially compensates the small lensing effect produced for being further away from the lens.

## 9.3 Relevant scales for wave optics detection

In sec. 8.4 we anticipated that there exist critical impact parameters in which geometric optics is a good approximation to solve for the trajectory and the arrival time of distinct gravitational wave images. Here, we explore those scales by considering a gravitational wave signal in the wave optics regime and the amplitude of a gravitational wave in the geometric optics approximation as a template. In fig. 9.2 we show again a contour plot of $\epsilon$ as a function of the reduced impact parameter and the mass of the lens. We define $\epsilon_{WO} = 10\%$ as the scale from which wave optics effects are relevant (red contour line). We call $y_{WO}$ its reduced impact parameter. From $M_L \gtrsim 30M_\odot$, $\epsilon < \epsilon_{WO}$ and the Schwarzschild radius of the lens is much bigger that the wavelength of the gravitational wave. The signal matches the template and therefore the geometric optics approximation is valid independently of $y$. On the other hand, for $M_L \lesssim 30M_\odot$, the wavelength of the gravitational wave is comparable to the Schwarzschild radius of the lens and diffraction effects become relevant. However, one can still use the geometric optics approximation in this regime if lensing occurs far enough from the lens (fig. 8.3). In particular, for $y > y_{WO} \sim 0.7$ the approximation is still valid regardless of the mass of the lens. For $1M_\odot \lesssim M_L \lesssim 30M_\odot$, $y_{WO}$ decreases when $M_L$ increases. One of the main conclusions of this section is that a gravitational wave needs to pass by a lens with a smaller impact parameter than its Einstein radius in order to detect wave effects.

We summarize the results of the previous two sections in a more general way in fig. 9.3, where we show the reduced impact parameter of the lens as a function of

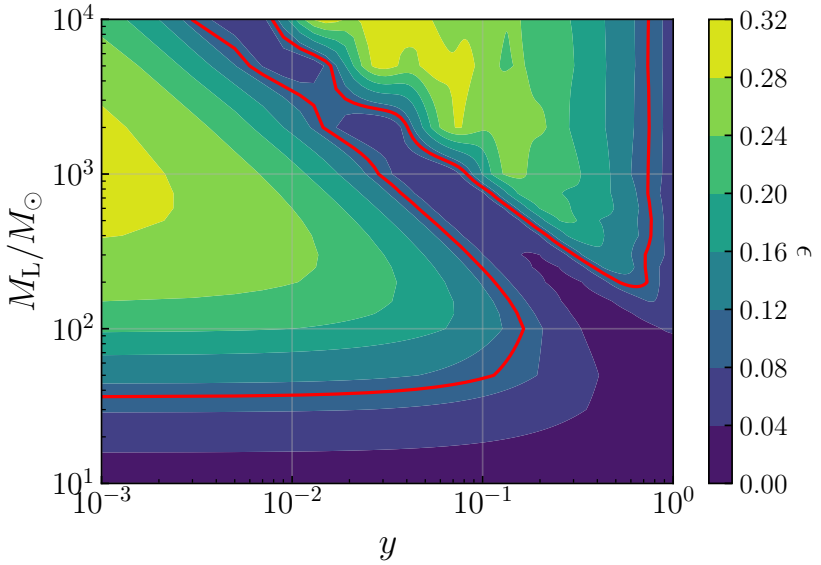


Figure 9.1: Detectability of lensing $\epsilon$ as a function of the lens mass $M_{\rm L}$ and the reduced impact parameter $y$. A gravitational wave sourced by a non-rotating compact binary at $z_{\rm s} = 1.0$ with $m_1 = m_2 = 30M_\odot$ and $q = m_1/m_2 = 1$ is lensed by a point mass lens at $z_{\rm L} = 0.2$ and mass $M_{\rm L}$. The polar and azimuthal angles of the source in the detector frame are $\theta = 0.3$ and $\phi = 0.4$ respectively. The orientation angle, i.e., the orientation of the angular momentum projected onto sky coordinates, is $\psi = 1.5$. The observed polar inclination angle is $\iota = 0$. The higher modes are also considered. We have described the signal in the wave optics regime and an unlensed template and have obtained $\epsilon$ as a function of $M_{\rm L}$ and $y$.

the ratio $\lambda/R_{\rm s}$. There is wide range ($1 \leq \lambda/R_{\rm s} \leq 250$) in which geometric optics is a valid approximation even if the wavelength of the gravitational wave is larger than the Schwarzschild radius of the lens. This is due to the fact that the relative difference between both approximations does not reach the 10% that we have imposed to consider that wave effects are relevant.

For $\lambda/R_{\rm s} \gtrsim 350$ or $y > y_{\rm c}$ we do not detect any gravitational wave lensed signal. For $\lambda/R_{\rm s} \lesssim 250$ geometric optics (GO) is a good approximation to obtain the amplification factor and the signal is detectable. For $250 \lesssim \lambda/R_{\rm s} \lesssim 350$ and $y < y_{\rm WO}$ we detect a signal that has to be treated in the wave optics (WO) regime. If $y > y_{\rm WO}$, the geometric optics approximation is valid again. The scale interval in which diffraction effects are relevant and detectable is very small and may vary. The main conclusion of this section is that one can, in practise, always use the geometric optics regime since diffraction effects are very unlikely to be observed.

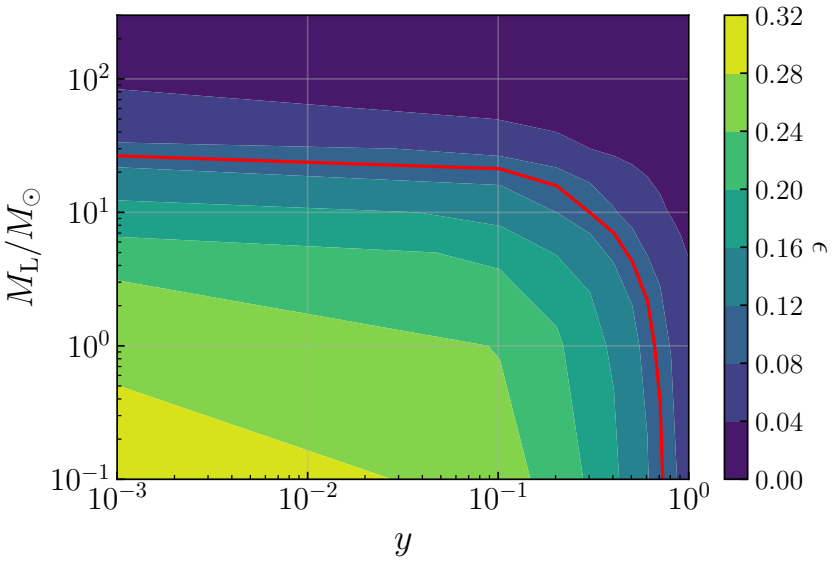


Figure 9.2: Relevance of wave-optics effects in lensing as a function of the lens mass $M_{\rm L}$ and the reduced impact parameter $y$. The gravitational wave source is the same as in fig. 9.1. We have described the signal in the geometric optics regime and a template in the wave optics approximation and have obtained $\epsilon$ as a function of $M_{\rm L}$ and $y$.

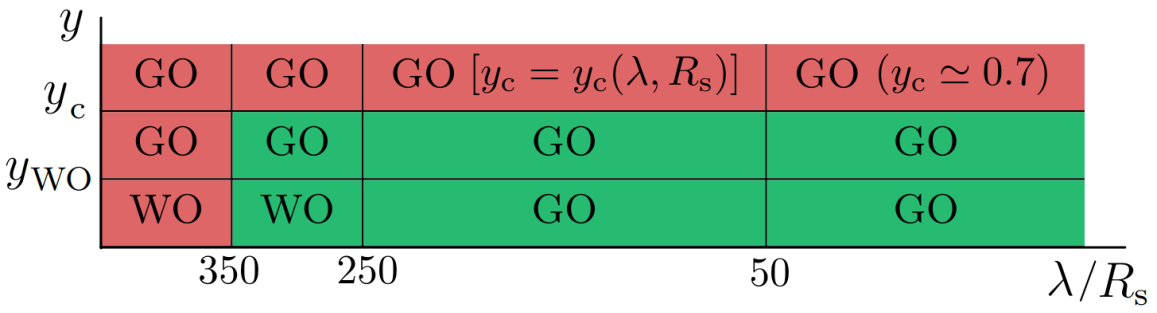


Figure 9.3: Relevant scales for lensing detection in the wave (WO) and geometric optics (GO) regime. We show in green the regions in which lensing is observed. On the other hand, lensing is not detectable in the red areas.

CHAPTER

# TEN

# THE PROBABILITY OF LENSING OF GRAVITATIONAL WAVES

In this section we compute the rate of lensed signals for three different scenarios: (a) A universe filled with compact objects, like PBHs, where microlensing effects are observed, (b) dark matter halos, in which the change of the waveform is due to strong lensing effects and (c) a universe with dark matter halos filled with compact objects, in which combined microlensing and strong lensing effects are observed.

Independently of lensing, for compact binary sources, the number of gravitational wave detections is

$$N_{\rm GW} = \int {\rm d}\mathbf{x}_{\rm s} \, \frac{\mathcal{R}_0}{1+z_{\rm s}} \frac{{\rm d}V_c}{{\rm d}z_{\rm s}} \, p(\theta_{\rm s}) \, p_{\rm det}(w) \tag{10.1}$$

where $w = {\rm SNR}_{\rm th}/{\rm SNR}(\theta_s)$ and $\theta_{\rm s} = (m_1, m_2, z_{\rm s})$ describes the set of parameters of the source that vary, $\mathcal{R}_0$ represents the local merger rate density, which depends on the source population, ${\rm d}V_c/{\rm d}z_{\rm s}$ is the differential comoving volume and $p(\theta_{\rm s})$ is the intrinsic, astrophysical distribution of source parameters. We follow the redshift distribution of sources from [178] whose expression is given by

$$p(z_{\rm s}) = \frac{(1+z_{\rm s})^{\alpha}}{1 + \frac{(1+z_{\rm s})}{1+z_{\rm p}}^{\alpha+\beta}} \tag{10.2}$$

with $\alpha = 1.9, \beta = 3.4$ and $z_{\rm p} = 2.4$ and depicted in fig. 10.1. We assume that $m_1$ follows a power-law distribution, $p(m_1) \propto m_1^{-0.4}$ and $m_2$ is uniformly distributed in $m_{\rm min} < m_2 < m_1 < m_{\rm max}$ with $m_{\rm min} = 5M_\odot$ and $m_{\rm max} = 50M_\odot$. $p_{\rm det}(w)$ determines the probability of detecting a gravitational wave signal that is above a given signal-to-noise (SNR) threshold, which we set for an Advanced LIGO detector to be ${\rm SNR}_{\rm th} = 8$. Therefore, $p_{\rm det}(w > 1) = 0$. We consider aLIGO at upgraded sensitivity (A+) [179]. This function also includes the effect of random orientations, inclinations and sky positions of the source in the SNR (see sec. 4.2 in [180]). We use an IMRPhenomD [181] waveform of a binary black hole merger generated by PYCBC[1]. For the lensing model

[1] `https://github.com/gwastro/pycbc/tree/v1.14.4`

we use the strongest-lens prescription described in Part I in which lensing is clearly dominated by the strongest lens, the one which is closest to the line of sight.

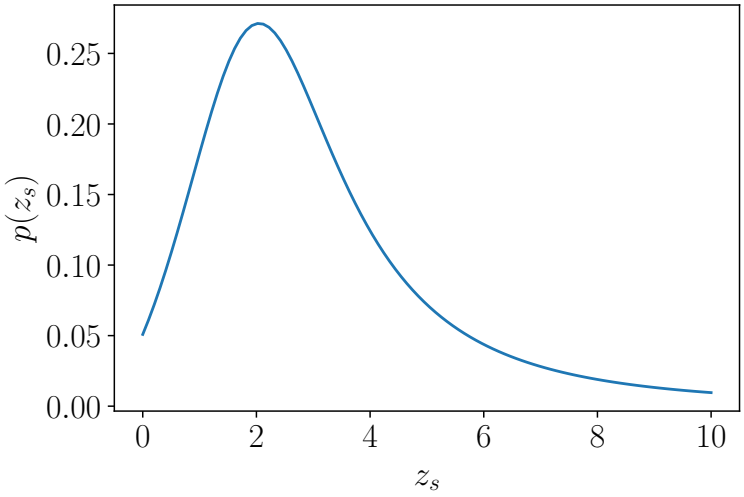


Figure 10.1: Redshift distribution of sources.

## 10.1 Microlensing

We now consider a region with density $\rho(\mathbf{x})$ filled with an spatially homogeneous and isotropic monochromatic distribution of compact objects with mean density $\rho_{\rm L}(\mathbf{x}) = \alpha\rho(\mathbf{x})$, which can be treated as point lenses. The situation is depicted in fig. 10.2. The probability of a given source being lensed is determined by the microlensing optical depth. For a given lens model, it depends on the properties of the source, $\theta_{\rm s}$, the cross section $\sigma$ and the number density of lenses $n_{\rm L} = \rho_{\rm L}/M_{\rm L}$.

$$\tau_{\rm L}(z_{\rm s}) = \frac{1}{\Omega}\int {\rm d}V_c\, n_{\rm L}(\theta_{\rm L})\sigma(\theta_{\rm s},\theta_{\rm L}) \tag{10.3}$$

where $\Omega = 4\pi$ for the full sky and $\theta_{\rm L} = (M_{\rm L}, z_L, b)$ is the set of lens parameters. We have defined the *detectability effective cross section* as

$$\sigma(\theta_{\rm s},\theta_{\rm L}) = \pi u_{\rm c}^2\theta_{\rm E}^2(z_{\rm s}, z_L) \tag{10.4}$$

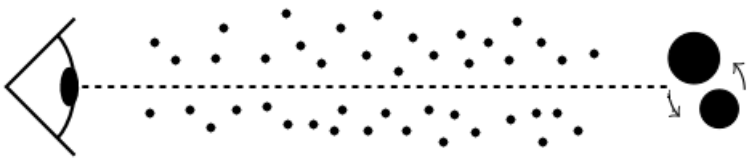

Figure 10.2: A lensed signal is observed through a universe filled with a fraction $\alpha$ of the matter density made of compact objects.

where we recall that $u_c \simeq y_c$ is the detectability threshold. We have redefined the cross section because we are interested in the probability of detecting lensing, not just the probability of a gravitational wave being lensed. Equation (10.3) reads

$$\tau_L(z_s) = \frac{2\pi\alpha}{3} \frac{G\,\Omega_{0,M}\,\rho_{crit}}{c^2} u_c^2\, D_{os}(z_s) \tag{10.5}$$

where $\Omega_{0,M}$ and $\rho_{crit}$ are the matter density today and the critical density respectively.

The observed waveform due to microlensing is given by eq. (8.23). In fig. 10.3 we show the optical depth for 3 different values of the critical reduced impact parameter. Increasing $u_c$ increases the effective cross section and hence increases the microlensing optical depth. Including the optical depth in eq. (10.1) the rate of observed

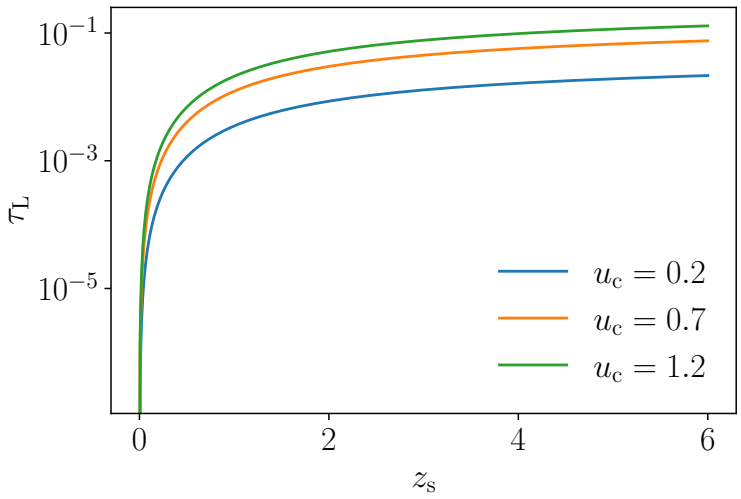


Figure 10.3: Optical depth as a function of the redshift of the source for 3 different values of the critical reduced impact parameter of the lens.

gravitational wave signals reads

$$N_{micro} = \int d\theta_s \int d\theta_L\, \tau_L(z_s)\, \frac{\mathcal{R}_0}{1+z_s} \frac{dV_c}{dz_s}\, p(\theta_s)\, p_{det,micro}(w, v) \tag{10.6}$$

where $p_{det,micro}(w, v)$, with $v = X/\Delta\chi^2$ and $X = 10$, determines the probability of detecting a lensed gravitational wave signal. Therefore, $p_{det,micro}(w, v > 1) = 0$.

## 10.2 Strong lensing

In the next scenario we consider a universe filled with an homogeneous distribution of dark matter halos, which we define as the region where the density is 200 times the critical density of the universe, $\rho_{200}$. The number density of dark matter halos, which we model using a Press–Schechter function, is $n_{halo} = \rho_{halo}/M_{halo}$, with $\rho_{halo} = \rho_{200}$. In this regime, we observe multiple images and need to account for the effect of

lensing magnification. We assume that strong lensing is identified by type II waveform distortions. This scenario is schematically represented in fig. 10.4. We choose the singular isothermal sphere (SIS) as our fiducial lens model whose lensing cross-section is determined by their velocity dispersion $\sigma_{\rm V}$, a proxy for the lens mass. Although the SIS is not a good model of dark matter halos but of the mass distribution of elliptical galaxies near their Einstein radius, it has the clear advantage of simplicity. We nonetheless think that this model is a good first approximation. The Einstein radius of a SIS is

$$\theta_{\rm E,halo} = 4\pi \left(\frac{\sigma_{\rm V}}{c}\right)^2 \frac{D_{\rm LS}}{D_{\rm S}}. \tag{10.7}$$

The probability of a gravitational wave being strongly lensed is determined by the lensing optical depth of the lens model

$$\tau_{\rm halo}(z_{\rm s}) = \frac{1}{\Omega}\int {\rm d}V_c \; n_{\rm halo}(\theta_{\rm L})\sigma_{\rm halo}(\theta_{\rm s},\theta_{\rm L}) \tag{10.8}$$

with $\sigma_{\rm halo} = \pi\theta^2_{\rm E,halo}$. In fig. 10.5 we show the optical depth for different halo masses. Increasing the halo mass, increases its velocity dispersion and hence increases the lensing cross-section. Dark matter halos induce strong gravitational lensing effects

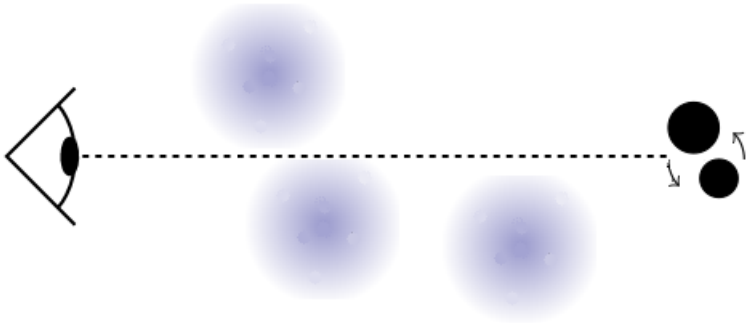

Figure 10.4: A lensed signal is observed through a universe filled with a dark matter halos. We assume a SIS profile to model the halos

so we use a waveform in the geometric optics regime without interference effects, i.e., $h_{\rm L} \sim \sqrt{\mu}\; h$. Including the magnification distribution and the lensing optical depth into the integration in eq. (10.1) we obtain the rate of strong lensing signals.

$$N_{\rm strong} = \int {\rm d}\theta_{\rm s} \int {\rm d}\mu \; \tau_{\rm halo}(z_{\rm s}) \frac{\mathcal{R}_0}{1+z_{\rm s}} \frac{{\rm d}V_c}{{\rm d}z_{\rm s}} \; p(\theta_{\rm s}) \; p(\mu) \; p_{\rm det}(\tilde{w}) \tag{10.9}$$

with $\tilde{w} = \rho_{\rm th}/\sqrt{\mu}\rho(\mathbf{x}_{\rm s})$.

## 10.3 Strong lensing with microlensing corrections

Finally we consider a homogeneous distribution of dark matter halos with radius $R$ filled with a monochromatic distribution of compact objects, such as the situation

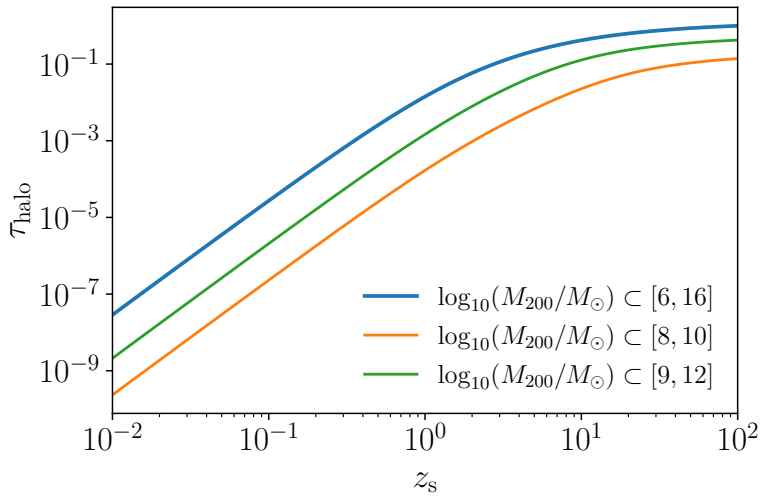


Figure 10.5: Optical depth as a function of source redshift for 3 different intervals of halo masses.

depicted in fig. 10.6. Again, we assume a SIS profile for the dark matter halos. The signal is due to strong lensing effects produced by the dark matter halos with microlensing contributions of the small lenses inside. In this case, the amplified signal produced by the halos allows us to observe the small contributions of the small lenses. For simplicity, we combine the microlensing effect of the small lenses and the strong lensing effect produced by the dark matter halos in a multiplicative way.

$$h_L(\mathbf{x}_{\rm s}, \mathbf{x}_{\rm L}, f, \mu) = \tilde{F}(f, \mu)\; h(\mathbf{x}_{\rm s}, \mathbf{x}_{\rm L}, f) \tag{10.10}$$

with

$$\tilde{F}(f, \mu) = \sqrt{\mu}\; F(f) \tag{10.11}$$

where $\sqrt{\mu}$ is the strong lensing amplification and $F(f)$, the microlensing amplification factor. This combination neglects the effect of shear, which has a direct correlation with $\mu$ and would therefore change eq. (10.11). However, there are reasons to neglect this effect because, as seen in Part I, the effect of shear is negligible in the statistics of extragalactic microlensing of light. As a result, we believe that these are all good first approximations. Furthermore, we also consider that the halos only contain compact objects whose density is given by eq. (8.30).

We model the combination of the microlensing and strong lensing effects similarly to the microlensing model only but with an extra parameter, the strong lensing magnification. In particular, the number density of compact objects and the cross section depend on that parameter. The differential optical depth in this scenario is therefore

$$\mathrm{d}\tau_{\rm L}(z_{\rm s}, z_{\rm L}, \mu) = \frac{1}{\Omega} \int \mathrm{d}V_c\; \mathrm{d}n_{\rm L}(\theta_{\rm L}, \mu)\sigma(\theta_{\rm s}, \theta_{\rm L}, \mu) \tag{10.12}$$

which represents the fraction of the sky magnified between $\mu$ and $\mu + \mathrm{d}\mu$ where the effect of microlensing is detectable. The cross section in this scenario is the detectabil-

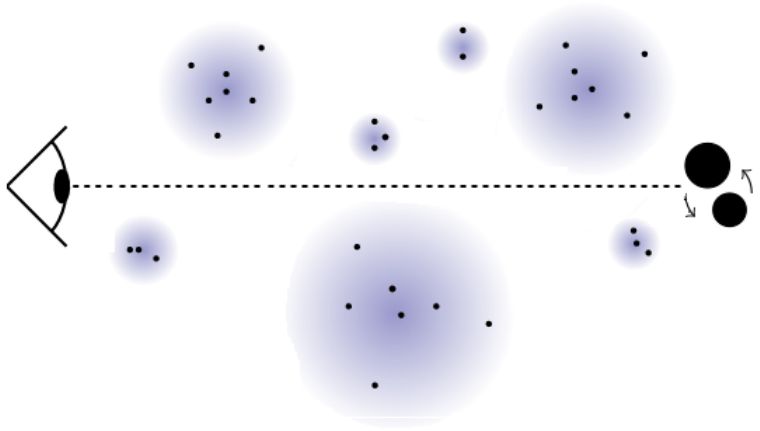

Figure 10.6: A lensed signal is observed through a universe filled with dark matter halos that contain only compact objects.

ity effective cross section of the microlensing-only case amplified by $\mu$.

$$\sigma(\theta_{\rm s}, \theta_{\rm L}, \mu) = \sqrt{\mu}\pi u_{\rm c}^2 \theta_{\rm E}^2(z_{\rm s}, z_L) \tag{10.13}$$

The number density of compact objects is given by $n_{\rm L}(\mu, \theta_{\rm L}) = \rho(\mu)/M_{\rm L}$ where we have replaced $\rho(r)$ by $\rho(\mu)$ because there is a direct correlation between the strong lensing amplification and the distance to the center of the halo. In particular, the closer to the center the lens is, the higher the amplification. The optical depth is finally obtained by marginalizing over the amplification.

$$\tau_{\rm L}(z_{\rm s}, z_{\rm L}) = \int {\rm d}\mu \; p(\mu) \frac{{\rm d}\tau_{\rm L}(z_{\rm s}, z_{\rm L}, \mu)}{{\rm d}\mu} \tag{10.14}$$

In fig. 10.7 we show the optical depth as a function of the redshift for different values of the critical impact parameter. As expected, due to the contribution of the dark matter halos, the optical depth is larger than the microlensing optical depth. As a result, we anticipate that the rate of lensed events is also higher.

Including the differential lensing optical depth into eq. (10.1), we obtain the rate of strongly lensed signals due to the dark matter halos with the microlensing corrections due to the population of compact objects that are contained in them.

$$N_{\rm strong+micro} = \int {\rm d}\theta_{\rm s} \int {\rm d}\mu \; \frac{{\rm d}\tau_{\rm L}(z_{\rm s}, z_{\rm L}, \mu)}{{\rm d}\mu} \; \frac{\mathcal{R}_0}{1+z_{\rm s}} \frac{dV_c}{dz_{\rm s}} \; p(\theta_{\rm s}) \; p_{\rm det,micro}(\tilde{w}, v) \tag{10.15}$$

Note that we have included the differential optical depth because $p_{\rm det,micro}$ depends in this case on the strong lensing amplification.

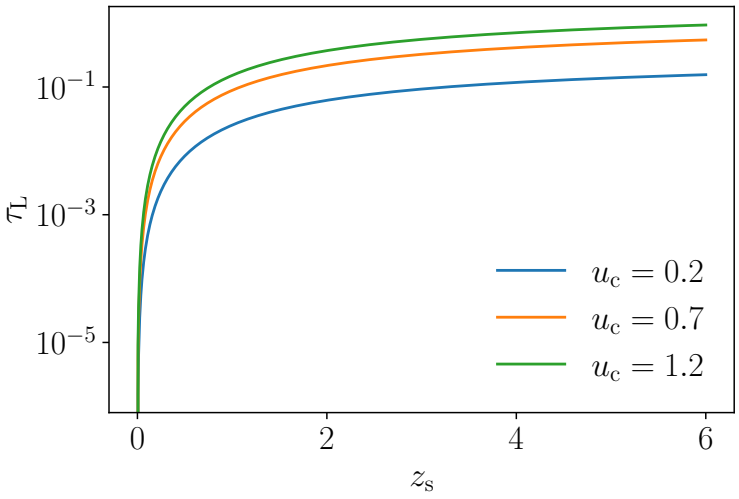


Figure 10.7: Optical depth as a function of source redshift for 3 different values of $u_c$.

CHAPTER

# ELEVEN

# FORECASTS

In this chapter we compute the predictions for the rate of lensed gravitational wave signals for the different scenarios described above. We fix the local merger rate density to $\mathcal{R}_0 = 30\ \mathrm{yr}^{-1}\ \mathrm{Gpc}^{-3}$. By solving eq. (10.1) we obtain the expected observed source merger events per year for different sensitivities.

| O3 ($\mathrm{yr}^{-1}$) | O4 ($\mathrm{yr}^{-1}$) | O5 ($\mathrm{yr}^{-1}$) | VOY ($\mathrm{yr}^{-1}$) | ET($\mathrm{yr}^{-1}$) |
|---|---|---|---|---|
| 64.2 | 193.4 | 1244.9 | 12091.5 | 43258.3 |

Table 11.1: Merger rate for the 3 observation runs of LIGO (O3, O4, O5), LIGO Voyager (VOY), and the Einstein Telescope (ET).

In fig. 11.3 we show the results for a universe filled with compact objects whose energy density constitutes a fraction $\alpha$ of the matter content. As expected, the lensing probability increases with $\alpha$ because the optical depth increases with that parameter. The more lenses in the line of sight, the more lensed events we observe. For a fixed $\alpha$ the rate reaches a maximum at $M_{\mathrm{L}} \simeq 300 M_{\odot}$. From this mass a lensed signal can be detected at higher $u_{\mathrm{c}}$ (second island of fig. 9.1). In addition we also show in the figure the evolution of the rate of microlensed events with redshift for different sensitivities and compare it with the merger rate. As expected the rate increases with the sensitivity and reaches a maximum at different redshifts, from which it starts decreasing due to the redshift distribution (fig. 10.1). The rate is not affected by the presence of higher modes in the gravitational wave. In table 11.2 we show the expected observed lensed events after integrating for all redshifts. The main conclusion is that this method could help to constrain the abundance of compact objects with the detection of lensed events. While the chance of observing such signals is small for O3 we do expect to detect them in the next observation runs, even for a low fraction of compact objects. Obviously the expected rate will increase with the subsequent upgrades of the detectors.

The evolution of observed strongly lensed events with redshift is shown in fig. 11.2. We have not consider lens masses above $\log(M_{\mathrm{halo}}/M_{\odot}) = 12$, which is the typical mass of a galaxy. The reason is that larger masses produce time delays greater than a

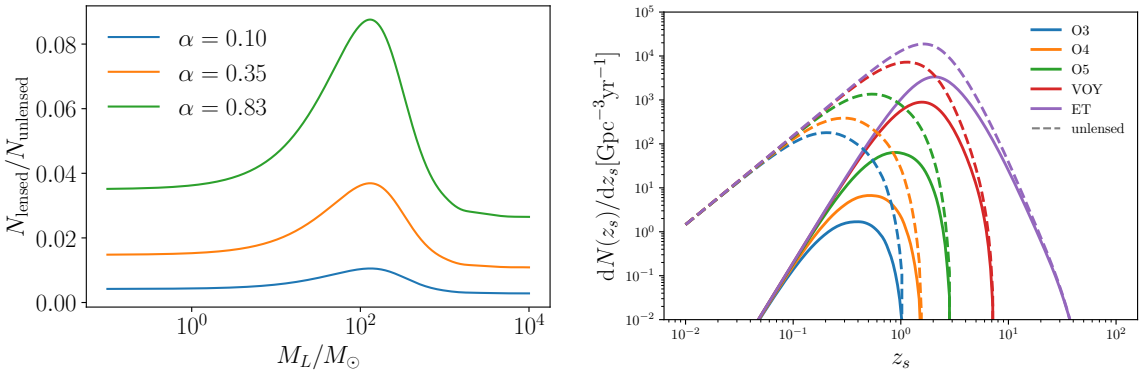


Figure 11.1: *Left*: Expected fraction of microlensed gravitational wave signals for O3: dependence in the fraction $\alpha$ of compact objects. *Right*: Evolution of observed microlensed with redshift for different sensitivities, LIGO (O3, O4, O5), Voyager (VOY) and the Einstein Telescope (ET) and its comparison with the unlensed rate. As expected the rate of lensed events is lower than the merger rate.

| $\alpha$ | O3 ($\mathrm{yr}^{-1}$) | O4 ($\mathrm{yr}^{-1}$) | O5 ($\mathrm{yr}^{-1}$) | VOY ($\mathrm{yr}^{-1}$) | ET($\mathrm{yr}^{-1}$) |
|---|---|---|---|---|---|
| 0.10 | 0.2 (0.32%) | 0.9 (0.47%) | 13.6 (1.09%) | 239.8 (1.98%) | 999.4 (2.31%) |
| 0.35 | 0.5 (0.78%) | 2.7 (1.40%) | 41.3 (3.32%) | 756.5 (6.26%) | 3285.1 (7.59%) |
| 0.83 | 0.8 (1.25%) | 4.5 (2.33%) | 71.3 (5.73%) | 1405.6 (11.63%) | 6648.4 (15.37%) |

Table 11.2: Microlensed rate for the 3 observation runs of LIGO (O3, O4, O5), Voyager (VOY) and the Einstein Telescope (ET) for different values of the fraction of compact objects, $\alpha$ with the percentage of the merger rate in brackets.

| O3 ($\mathrm{yr}^{-1}$) | O4 ($\mathrm{yr}^{-1}$) | O5 ($\mathrm{yr}^{-1}$) | VOY ($\mathrm{yr}^{-1}$) | ET($\mathrm{yr}^{-1}$) |
|---|---|---|---|---|
| 0.01 (0.02%) | 0.1 (0.05%) | 3.1 (0.24%) | 127.3 (1.05%) | 978.4 (2.26%) |

Table 11.3: Strongly lensed rate for the 3 observation runs of LIGO (O3, O4, O5), Voyager (VOY) and the Einstein Telescope (ET) with the percentage of the merger rate in brackets. In this case $6 \leq \log(M_{\rm halo}/M_\odot) \leq 12$

year (fig. 11.2), which is the observation time of the detector.

Just like the case of a universe filled with compact objects, we integrate for all the redshifts of the source and obtain the total number of strongly lensed events. The chances of observing multiple images in the waveform are low for the next observation run. However, this situation will change in the following observation runs of LIGO where we aim to observe around the 1% of the merger rate strongly lensed.

Finally, we consider the last scenario in which the compact objects are enclosed in dark matter halos. In this case, the lenses produce strong and microlensing effects combined. As we anticipated, the probability of detecting microlensing contributions in the strong lensing signal is larger than the probability of detecting only microlensing.

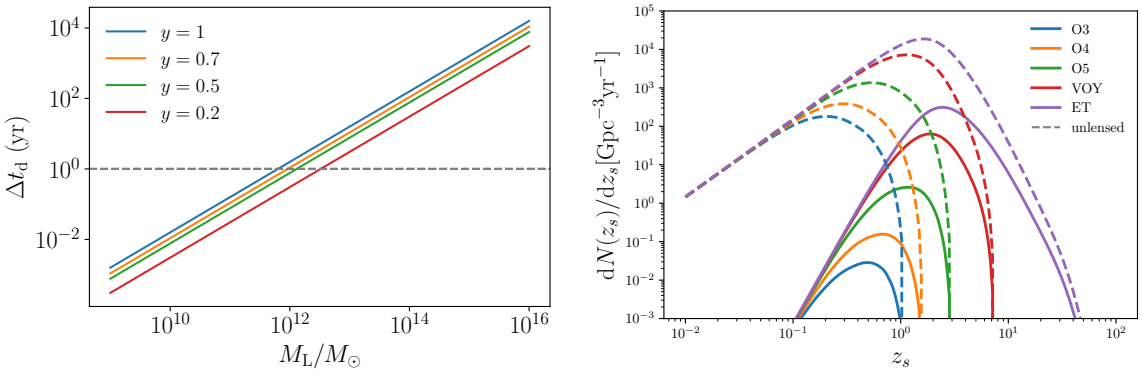


Figure 11.2: *Left*: Time delay between images as a function of the halo mass and for different values of the position of the source. Since we are only interested in the events that take place within the observation time of the detector we exclude the halo masses that produce time delays greater than a year. *Right*: Evolution of observed strongly lensed events with redshift for different sensitivities, LIGO (O3, O4, O5), Voyager (VOY) and the Einstein Telescope (ET) and its comparison with the merger rate.

| O3 ($\mathrm{yr}^{-1}$) | O4 ($\mathrm{yr}^{-1}$) | O5 ($\mathrm{yr}^{-1}$) | VOY ($\mathrm{yr}^{-1}$) | ET($\mathrm{yr}^{-1}$) |
|---|---|---|---|---|
| 0.8 (1.25%) | 4.3 (2.22%) | 65.9 (5.29%) | 1207.2 (9.98%) | 5194.3 (12.01%) |

Table 11.4: Expected rate of strong lensing detections with microlensing contributions for the 3 observation runs of LIGO (O3, O4, O5), LIGO Voyager (VOY), and the Einstein Telescope (ET) with the percentage of the merger rate in brackets.

As explained in the previous section, the magnified signal produced by the dark matter halos allows to observe the small contribution of the compact objects inside the halo, which would not be possible if they were isolated producing only microlensing effects in the waveform. However, this is only true up to a fraction of the total matter that consists of compact objects. From $\alpha \gtrsim 0.50$ the universe is sufficiently populated by compact objects that the rate of microlensing events becomes higher than the rate of strong lensing and microlensing combined.

The conclusion of this section is that ground-based detectors are likely capable of detecting lensing events of gravitational waves. Furthermore, the upcoming third-generation detectors, such as the Einstein Telescope, which will reach sensitivities of $10^4$Hz and will be able to detect the merger of low-massive black holes, will make these observations a certainty and will open up new possibilities for gravitational wave astronomy.

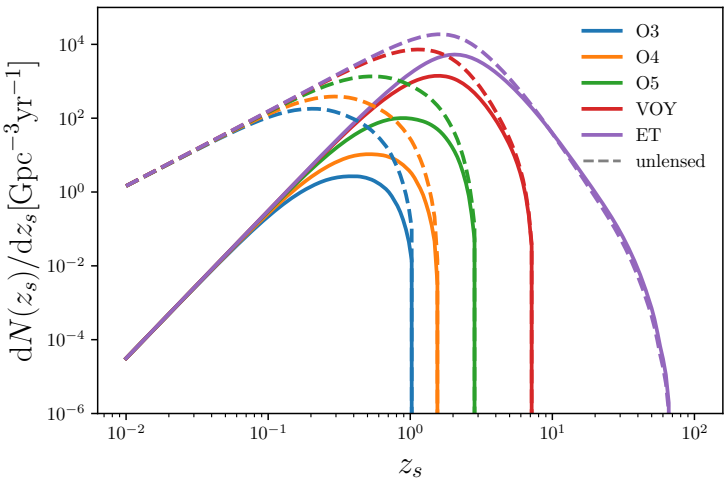


Figure 11.3: Evolution of observed lensed events with redshift for different sensitivities, LIGO (O3, O4, O5), Voyager (VOY) and the Einstein Telescope (ET) and its comparison with the merger rate.

CHAPTER

# TWELVE

# CONCLUSION

The observations of gravitational waves show that they are compatible with the predictions of general relativity. In this theory, gravitational waves, in the eikonal approximation, follow null geodesics, just like light. As a result, *gravitational waves experience the same lensing effects as light.*

However, as opposed to light, the wavelength of gravitational waves can be comparable to the size of the lens. Consequently, interference effects may arise and the geometric optics regime, which is used in electromagnetic waves, is not a good approximation in some cases. In this work, we have summarized aspects of the theory of lensing of gravitational waves and have explored the cases in which the wave optics approximation is needed. We find that for small impact parameters, i.e., if the gravitational wave passes near the lens, wave effects are relevant except for high frequencies. On the other hand, geometric optics is a good approximation for larger values of the impact parameter regardless of the frequency of the waveform. We also find that, even if the wavelength of the gravitational wave is comparable to the size of the lens and the geometric optics approximation holds, it can also present an interference pattern (absolute coherence). This regime is not present in light due to the thin spectral extension. In order to unify and have a more intuitive nomenclature, we propose to name this regime, the *absolutely coherent geometric optics.*

Furthermore, we have explored the scales in which these regimes are detectable. We have studied the dependency on the mass of the lens and the impact parameter and have found that the scales in which wave optics effects are relevant and detectable are very tiny, just for low-mass lenses and impact parameters. This implies that, in most of the cases, geometric optics is a valid approximation. We have also showed that there exist a critical impact parameter from which lensing is not detectable.

We have used those results to compute the optical depth and the rate of lensed signals for three scenarios: a universe filled with compact objects only, dark matter halos and the same halos filled with compact objects, similar to what we have done in Part I. We have redefined the cross section in order to obtain the probability of

detecting lensing, not only the probability of having lensing.

Finally we have made a forecast of the rate of microlensed events as a function of the fraction of compact objects, $\alpha$, for different detectors and show that it peaks at lens masses of $100M_{\odot}$. We have predicted that in the next observation run we should see those events regardless of $\alpha$. The predicted strongly lensed rate is very low for current observation runs but we expect to see those events in O5 and maybe in O4. We have not considered larger halo masses than $10^{12}M_{\odot}$ because they produce time delays bigger than a year, which is the observation time. Current detectors are also able to detect lensing caused by compact objects enclosed in the dark matter halos. In addition, more detections are expected with the upcoming ground detectors like the Einstein Telescope. Just like light, lensing of gravitational waves demonstrates to be a potentially powerful probe to constrain the abundance of compact objects.

# EPILOGUE

In this thesis, we have studied the gravitational lensing effect of light and gravitational waves in a clumpy universe. In Part I, we have showed that extragalactic microlensing is a powerful tool to study the clumpiness of dark matter and have derived, from first principles, a theoretical model for the amplification probability. The next step of this work consists in applying its results to real data, which will require an efficient numerical implementation of our model for the amplification probability. In Part II, we have explored the scales in which wave effects are detectable. Furthermore we have studied the different regimes in which the lensing of gravitational waves manifests itself and have proposed a new nomenclature for the interference effects that appear in the geometric optics approximation. Finally, we have computed the expected rate of lensed events in current and future detectors. The next step of this work is to use more realistic models. These include, other fiducial lens model, such as the Einasto and Navarro–Frenk–White profiles, a different coupling between strong lensing and microlensing that accounts for the effects of shear and caustic crossing events and different source distributions.

Just like the last century was the quantum revolution, this century is certainly the century of gravity. We live in an era in which theory and data are practically simultaneously performed. As mentioned in the preface, the study of the nature of dark matter is the core of modern cosmology and the theoretical understanding of the clumpy structure of the matter distribution in our universe is therefore crucial for physics. This thesis has done its bit to move in that direction. However, the best is yet to come. Future observational data will bring the next revolution in physics: the confirmation that our universe is, in fact, clumpy.

# EPÍLOGO

En esta tesis hemos estudiado el efecto de lente gravitacional de la luz y las ondas gravitacionales en un universo grumoso. En la Parte I, hemos demostrado que el efecto de microlensing extragaláctico es una herramienta poderosa para estudiar la naturaleza de la materia oscura y hemos derivado, a partir de principios básicos, un modelo teórico para la probabilidad de amplificación. El siguiente paso de este trabajo consiste en aplicar sus resultados a datos reales, lo que requerirá una implementación numérica eficiente de nuestro modelo para la probabilidad de amplificación. En la Parte II, hemos explorado las escalas en las que los efectos de onda son detectables. Además, hemos estudiado los diferentes regímenes en los que el efecto de lente gravitacional se manifiesta y hemos propuesto una nueva nomenclatura para los efectos de interferencia que aparecen en la aproximación de la óptica geométrica. Finalmente, hemos calculado la tasa esperada de eventos de ondas gravitacionales que han sido desviadas de su trayectoria debido a lentes gravitacionales en los detectores actuales y futuros. El siguiente paso de este trabajo consiste en utilizar modelos más realistas. Estos incluyen, otro modelo de lensing, como los perfiles de Einasto y Navarro-Frenk-White, un acoplamiento diferente entre los efectos de lentes gravitacionales fuertes y microlentes que explica los efectos de cizalladura y los eventos de cruce de cáusticas, y las diferentes distribuciones de fuentes.

Si el siglo pasado se produjo la revolución cuántica, este siglo es sin duda el siglo de la gravedad. Vivimos en una era en la que la teoría y el análisis de datos se realizan prácticamente a la vez. Como se mencionó en el prefacio, el estudio de la naturaleza de la materia oscura es el núcleo de la cosmología moderna y, por lo tanto, la comprensión teórica de la estructura de la distribución de la materia en nuestro universo es crucial para la física. Esta tesis ha puesto su granito de arena para avanzar en esa dirección. Sin embargo, lo mejor está por venir. Los datos observacionales futuros traerán la próxima revolución en la física: la confirmación de que nuestro universo es, de hecho, grumoso.

# Appendices

APPENDIX

# A

# WEAK-LENSING STATISTICS WITH RAYGALGROUPSIMS

This appendix is dedicated to our analysis of the statistics of weak-lensing convergence and shear from a numerical simulation. Specifically, we have used results from a dark-matter-only simulation performed with the $N$-body code RAMSES [182, 183]. The simulation has been performed with the best-fit parameters of WMAP-7 [184], a comoving length of $2625h^{-1}$ Mpc and a particle mass of $1.88 \times 10^{10} h^{-1} M_\odot$. Fully relativistic ray tracing has been performed through this simulation [96] using the MAGRATHEA library [185, 186]. Healpix maps with various lensing quantities, such as convergence, shear and magnification, are publicly available.[1] We focus here on the PDF of convergence $\bar{\kappa}_{\rm os}$ and (macro)shear $\bar{\gamma}_{\rm os}$.

## A.1 Convergence

We analysed the PDF of the weak-lensing convergence $\bar{\kappa}_{\rm os}$ obtained by ray tracing. In the redshift range $z_{\rm s} < 2$, we found that the following ansatz provides a good fit to the data,

$$p(\bar{\kappa}_{\rm os}; z_{\rm s}) = \frac{\mathrm{d}}{\mathrm{d}\bar{\kappa}_{\rm os}} \exp\left\{ - \left( \frac{\Delta\kappa(z_{\rm s})}{\bar{\kappa}_{\rm os} - \kappa_0(z_{\rm s})} \right)^{\nu(z_{\rm s})} + \left( \frac{\Delta\kappa(z_{\rm s})}{1 - \kappa_0(z_{\rm s})} \right)^{\nu(z_{\rm s})} \right\}, \tag{A.1}$$

where the parameters $\nu$, $\kappa_0$ and $\Delta\kappa$ depend on the source redshift $z_{\rm s}$. Note that eq. (A.1) is normalised to 1 for $\bar{\kappa}_{\rm os} \in [\kappa_0, 1]$ by definition; $\kappa_0(z_{\rm s}) < 0$ thus denotes the minimum convergence for sources at a redshift $z_{\rm s}$. Imposing that the convergence averages to 0 imposes the following constraint between the model parameters,

$$\kappa_0 = -\Gamma\left(\frac{\nu - 1}{\nu}\right) \Delta\kappa \,, \tag{A.2}$$

where $\Gamma$ denotes the usual Gamma function. Together with the above, we find that

$$\nu(z_{\rm s}) = 2.3\,(1 + z_{\rm s}) \tag{A.3}$$

[1] https://cosmo.obspm.fr/public-datasets/raygalgroupsims-relativistic-halo-catalogs

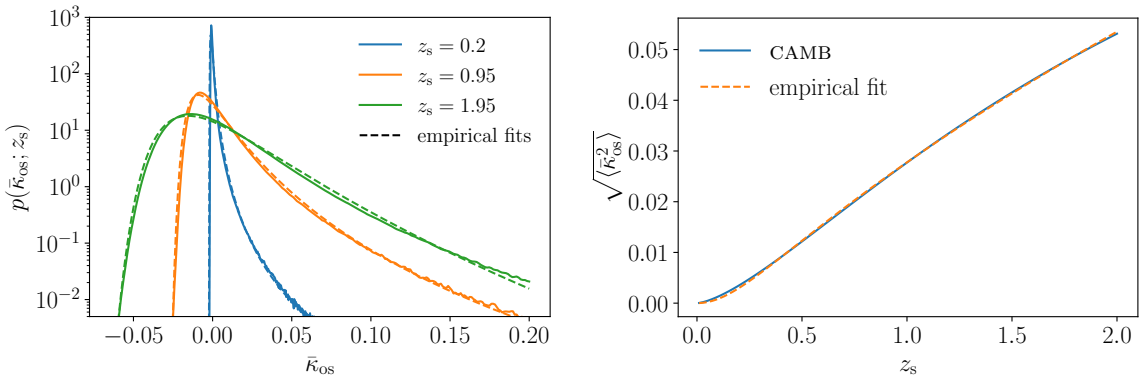


Figure A.1: Statistics of the weak-lensing convergence $\bar{\kappa}_{os}$. *Left*: comparison between the PDF of the convergence $\bar{\kappa}_{os}$ obtained from ray tracing in an $N$-body simulation (solid lines) and the ansatz of eq. (A.1) (dashed lines), with the constraint (A.2), $\nu(z_s) = 2.3(1 + z_s)$ and $\Delta\kappa$ left as a free parameter. *Right*: standard deviation of the convergence computed from CAMB with a *Planck*-2018 cosmology, compared with the empirical fit of eq. (A.6).

fits well the data as $\Delta\kappa$ is left as a free parameter. The accuracy of this empirical fit is illustrated in the left panel of fig. A.1.

As could be guessed from eq. (A.1), $\Delta\kappa$ is related to the variance of the convergence. Specifically, we have

$$\left\langle \bar{\kappa}^2_{os} \right\rangle = \Gamma\left(\frac{\nu-2}{\nu}\right) - \Gamma^2\left(\frac{\nu-1}{\nu}\right) \Delta\kappa^2 \,. \tag{A.4}$$

The variance of the convergence significantly depends on the cosmology. In the weak-lensing regime, at linear order and in Limber's approximation, it is known to read

$$\left\langle \bar{\kappa}^2_{os} \right\rangle = \int_0^\infty \frac{\ell \mathrm{d}\ell}{2\pi} P_\kappa(\ell, z_s) \,, \tag{A.5}$$

where $P_\kappa$ denotes the convergence angular power spectrum, which is directly related to the matter power spectrum [106]. Since the simulation data at our disposal used slightly outdated cosmological parameters, we thus expect the resulting $\left\langle \bar{\kappa}^2_{os} \right\rangle$ to be outdated as well. In order to circumvent this issue, we estimated $\left\langle \bar{\kappa}^2_{os} \right\rangle$ from eq. (A.5) using CAMB.[2] For a *Planck*-2018 cosmology [187], we find that the standard deviation of the convergence is well fit by

$$\sqrt{\left\langle \bar{\kappa}^2_{os} \right\rangle} = 0.0218 \ (1 + 12.6\, z)^{0.315} - 1 \,, \tag{A.6}$$

as illustrated in the right panel of fig. A.1. In practice, we substitute this expression into eq. (A.4) to determine $\Delta\kappa(z_s)$ for application in this article.

[2] `https://camb.info/`

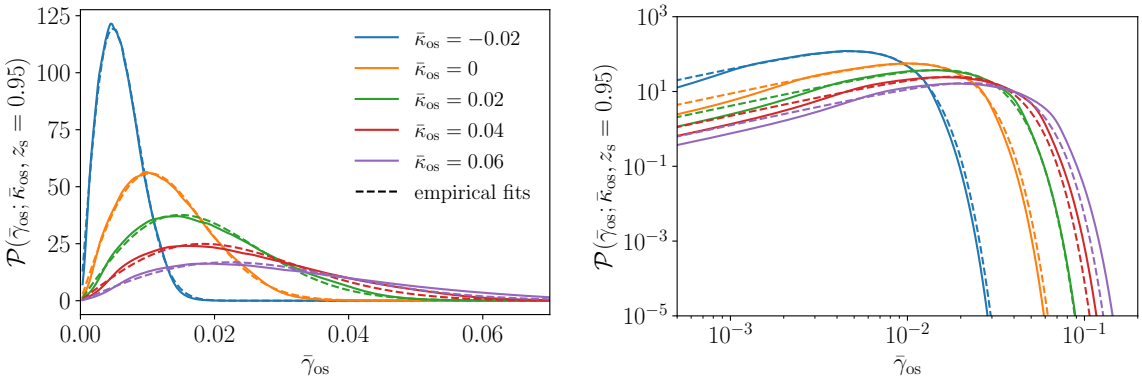


Figure A.2: Conditional PDF of the magnitude of weak-lensing shear $|\bar{\gamma}_{\rm os}|$ at fixed values of the convergence $\bar{\kappa}_{\rm os}$, for sources at $z_{\rm s} = 0.95$. The figures compare results from simulations (solid lines) with the ansatz of eq. (A.10) (dashed lines). *Left*: linear scale. *Right*: logarithmic scale.

## A.2 Macroshear

In the range of redshift relevant for the present discussion, we find that the conditional PDF for the shear at a fixed convergence, $p(\bar{\gamma}_{\rm os}; \bar{\kappa}_{\rm os}, z_{\rm s})$, is surprisingly well fit by a two-dimensional Gaussian distribution,

$$p(\bar{\gamma}_{\rm os}; \bar{\kappa}_{\rm os}, z_{\rm s})\, {\rm d}^2\bar{\gamma}_{\rm os} = \frac{1}{2\pi\sigma^2(\bar{\kappa}_{\rm os}, z_{\rm s})} \exp\ -\frac{|\bar{\gamma}_{\rm os}|^2}{2\sigma^2(\bar{\kappa}_{\rm os}, z_{\rm s})}\ {\rm d}^2\bar{\gamma}_{\rm os}\ . \tag{A.7}$$

Since the universe is statistically isotropic, there is no preferred orientation for the complex shear, and hence the conditional PDF of its magnitude takes the form

$$\mathcal{P}(|\bar{\gamma}_{\rm os}|; \bar{\kappa}_{\rm os}, z_{\rm s}) = 2\pi|\bar{\gamma}_{\rm os}|\, p(\bar{\gamma}_{\rm os}; \bar{\kappa}_{\rm os}, z_{\rm s}) \tag{A.8}$$

$$= \frac{|\bar{\gamma}_{\rm os}|}{\sigma^2(\bar{\kappa}_{\rm os}, z_{\rm s})} \exp\ -\frac{|\bar{\gamma}_{\rm os}|^2}{2\sigma^2(\bar{\kappa}_{\rm os}, z_{\rm s})} \tag{A.9}$$

$$= \frac{\rm d}{{\rm d}|\bar{\gamma}_{\rm os}|} \exp\ -\frac{|\bar{\gamma}_{\rm os}|^2}{2\sigma^2(\bar{\kappa}_{\rm os}, z_{\rm s})}\ . \tag{A.10}$$

Figure A.2 shows a comparison between the numerical data and the ansatz (A.10) for $z_{\rm s} = 0.95$; at that redshift we find the empirical expression $\sigma(\bar{\kappa}_{\rm os}, z_{\rm s} = 0.95) = 0.01 + 0.26\,\bar{\kappa}_{\rm os}$.

APPENDIX

# B

# DERIVATION OF THE MICROSHEAR DISTRIBUTION

This appendix is dedicated to the derivation of the distribution of the effective reduced microshear that was given in eq. (4.4).

## B.1 PDF of a sum of complex shears

Consider $N$ randomly distributed lenses $\ell$, each one producing a complex shear $s_\ell \in \mathbb{C}$. The total shear is the sum of all those contributions,

$$s = \sum_{\ell=1}^{N} s_\ell \ . \tag{B.1}$$

The PDF of $s$ is, therefore, the convolution product of the $N$ PDFs of the individual shears. Assuming – without loss of generality – that the $N$ lenses are indistinguishable and have identical statistical properties, we have

$$p_N(s) = (\underbrace{p_1 \star \ldots \star p_1}_{N \text{ times}})(s) \equiv p_1^{\star N}(s) \ , \tag{B.2}$$

where a $\star$ denotes a convolution product and $p_1$ is the PDF of the shear for 1 lens, accounting for the randomness of its position, mass, etc. The convolution product is better handled in Fourier space. We define here the Fourier transform in a way that acknowledges the spin-2 character of the complex shear,

$$\tilde{p}(q) \equiv \int \mathrm{d}^2 s \ \mathrm{e}^{-2\mathrm{i}\mathrm{Re}(q^* s)} \, p(s) \ , \qquad p(s) = \int \frac{\mathrm{d}^2 q}{(2\pi)^2} \ \mathrm{e}^{2\mathrm{i}\mathrm{Re}(q^* s)} \, \tilde{p}(q) \ , \tag{B.3}$$

with $q \in \mathbb{C}$ the Fourier variable dual to $s$; $^*$ denotes complex conjugation and the differential elements are $\mathrm{d}^2 q = \mathrm{d}q_1 \mathrm{d}q_2$, $\mathrm{d}^2 s = \mathrm{d}s_1 \mathrm{d}s_2$. We shall also use polar components for both $s = S\mathrm{e}^{2\mathrm{i}\varphi}$ and $q = Q\mathrm{e}^{2\mathrm{i}\psi}$, with $\varphi, \psi \in [0, \pi)$, in which case $\mathrm{d}^2 s = 2S\mathrm{d}S\mathrm{d}\varphi$ and $\mathrm{d}^2 q = 2Q\mathrm{d}Q\mathrm{d}\psi$. In Fourier space with the above convention, eq. (B.2) becomes

$$\tilde{p}_N(q) = \tilde{p}_1^N(q) \ . \tag{B.4}$$

Consider now the case where the lenses are all axisymmetric – this is valid for the application that will eventually interest us, namely point lenses. In that case the PDF of each lens only depends on $S \equiv |s|$,

$$p_1(s)\,\mathrm{d}^2 s = \mathcal{P}_1(S)\mathrm{d}S\,\frac{\mathrm{d}\varphi}{\pi} \qquad \text{with} \quad \mathcal{P}_1(S) \equiv 2\pi S\,p_1(S) \tag{B.5}$$

the PDF of the magnitude of the shear for single lens. The polar angle can be integrated out in the expression of the Fourier transform, which then only depends on $Q = |q|$,

$$\tilde{p}_1(Q) = \int_0^\pi \frac{\mathrm{d}\varphi}{\pi} \int_0^\infty \mathrm{d}S\;\mathcal{P}_1(S)\,\mathrm{e}^{-\mathrm{i}QS\cos 2(\varphi-\psi)} = \int_0^\infty \mathrm{d}S\;\mathcal{P}_1(S)\,J_0(QS)\;, \tag{B.6}$$

where $J_0$ is the zeroth order Bessel function. From the above, we notice that $\tilde{p}_1(q)$ may be also be interpreted as the expectation value of that Bessel function for a single lens,

$$\tilde{p}_1(Q) = \langle J_0(QS)\rangle_1\;, \tag{B.7}$$

where $\langle\ldots\rangle_1$ denotes the average over statistics of a single lens.

In the same manner, since $\tilde{p}_N(Q)$ does not depend on the polar angle $\psi$ of $q$, we may integrate this angle out in its inverse Fourier transform,

$$p_N(S) = \int_0^\infty \frac{Q\,\mathrm{d}Q}{2\pi} \int_0^\pi \frac{\mathrm{d}\psi}{\pi}\;\mathrm{e}^{\mathrm{i}QS\cos 2(\psi-\varphi)}\,\tilde{p}_N(Q) = \frac{1}{2\pi}\int_0^\infty \mathrm{d}Q\;Q\,J_0(QS)\,\tilde{p}_N(Q)\;. \tag{B.8}$$

The PDF of the sole magnitude $S$ of the sum all all $N$ complex shears is, therefore,

$$\mathcal{P}_N(S) = 2\pi S\,p_N(S) = \int_0^\infty \mathrm{d}Q\;QS\,J_0(QS)\,\tilde{p}_N(Q)\;. \tag{B.9}$$

## B.2 Large-$N$ limit

Now consider the setup depicted in fig. 4.1: the $N \gg 1$ lenses are distributed within a mesoscopic cone with half angle $\Theta$. Now as $\Theta$ is much larger than the typical Einstein radius of the lenses, it quite clear that $\mathcal{P}_1(S)$ must approach $\delta(S)$.[1] Since $J_0(0) = 1$, we conclude that $\tilde{p}_1(Q) = \langle J_0(QS)\rangle_1 \approx 1$. This suggests the following manipulation

$$\tilde{p}_N(Q) = \langle J_0(QS)\rangle_1^N = \langle 1 + [J_0(QS) - 1]\rangle_1^N \approx \exp\left[N\,\langle J_0(QS) - 1\rangle_1\right] \tag{B.10}$$

in the large-$N$ limit.

[1] A more technical, though heuristic, argument goes as follows. Just like the amplification PDF, the shear PDF of a single lens may be expressed as the ratio of a shear cross section with the solid angle of the cone, so that $\mathcal{P}_1(S) \propto (\pi\Theta^2)^{-1}$. Since $\Theta$ is much larger than the typical angular scale characterising a single lens, we expect $\mathcal{P}_1(S) \to 0$ for $S \neq 0$. But since $\mathcal{P}_1(S)$ is a PDF it must be normalised to 1. The only way out consists in having $\mathcal{P}_1(S \to 0)$ very large, in agreement with the intuition that it is very likely that a single lens lost in a huge domain produces a tiny shear.

## B.3 Application to the effective reduced microshear due to point lenses

The quantity of interest here is the effective reduced microshear, due to the compact objects located near the line of sight of the dominant lens at $\chi$,

$$s \equiv \frac{s_{\rm os}}{1-\kappa_{\rm os}} - \frac{s_{\rm od}}{1-\kappa_{\rm od}} - \frac{s_{\rm ds}}{1-\kappa_{\rm ds}} = \sum_{\ell=1}^{N} s_\ell \ , \qquad s_\ell \equiv \frac{4Gm_\ell}{(\underline{\beta}_\ell^*)^2}\, W(\chi_\ell), \tag{B.11}$$

with

$$W(\chi_\ell) \equiv (1+z_\ell) \times \begin{cases} \dfrac{\chi_{\rm s}-\chi_\ell}{(1-\kappa_{\rm os})\chi_\ell\chi_{\rm s}} - \dfrac{\chi_{\rm d}-\chi_\ell}{(1-\kappa_{\rm od})\chi_\ell\chi_{\rm d}} & \chi_\ell \le \chi_{\rm d} \\ \dfrac{\chi_{\rm s}-\chi_\ell}{(1-\kappa_{\rm os})\chi_\ell\chi_{\rm s}} - \dfrac{(\chi_\ell-\chi_{\rm d})(\chi_{\rm s}-\chi_\ell)}{(1-\kappa_{\rm ds})\chi_\ell^2(\chi_{\rm s}-\chi_{\rm d})} & \chi_\ell \ge \chi_{\rm d} \end{cases} \tag{B.12}$$

where $m_\ell, z_\ell, \chi_\ell$ denote the mass, redshift, comoving position of lens $\ell$, and $\underline{\beta}_\ell$ its complex unlensed angular position with respect to the line of sight; $\chi_{\rm d}, \chi_{\rm s}$ are the comoving positions of the main deflector and source.

We assume for simplicity that the lenses are uniformly distributed in comoving space, with masses independent of the positions, so that within the mesoscopic cone of fig. 4.1 we have

$$p(\chi_\ell, \beta_\ell, m_\ell)\, {\rm d}\chi_\ell {\rm d}\beta_\ell {\rm d}m_\ell = \frac{3\chi_\ell^2 {\rm d}\chi_\ell}{\chi_{\rm s}^3}\, \frac{2\beta_\ell {\rm d}\beta_\ell}{\Theta^2}\, p(m_\ell) {\rm d}m_\ell \ . \tag{B.13}$$

In the remainder of this appendix we shall drop the subscript $\ell$ to alleviate notation.[2]

In such conditions, the Fourier transform $\tilde{p}_1(Q)$ of the one-lens shear, interpreted as the expectation value of $J_0(SQ)$ following eq. (B.7) reads

$$\tilde{p}_1(Q) = \langle J_0(SQ)\rangle_1 = \int \frac{{\rm d}(\chi^3)}{\chi_{\rm s}^3}\, \frac{{\rm d}(\beta^2)}{\Theta^2}\, p(m){\rm d}m\ J_0\ \left[\frac{4Gm}{\beta^2}\, W(\chi) Q\right] - 1. \tag{B.14}$$

We may then perform the change of variable $\beta^2 \mapsto x = 4GmWQ/\beta^2$ to get

$$\langle J_0(SQ)\rangle_1 - 1 = \frac{4GQ}{\Theta^2} \int {\rm d}m\, m\, p(m) \int_0^{\chi_{\rm s}} \frac{{\rm d}(\chi^3)}{\chi_{\rm s}^3}\, W(\chi) \int_{4GmWQ/\Theta^2}^{\infty} \frac{{\rm d}x}{x^2}\, [J_0(x) - 1]. \tag{B.15}$$

In the limit where $\Theta$ is very large, the lower limit in the integral over $x$ can be set to zero, in which case the integral is known,

$$\int_0^\infty \frac{{\rm d}x}{x^2}\, [J_0(x) - 1] = -1 \ , \tag{B.16}$$

[2]This implies that *in this appendix only* $\chi \equiv \chi_\ell$ refers to the comoving position of a secondary deflector; in the main text we have instead $\chi \equiv \chi_{\rm d}$.

so that

$$\langle J_0(SQ)\rangle_1 - 1 \approx -\frac{4G\,\langle m\rangle\,Q}{\Theta^2}\int_0^{\chi_\mathrm{s}}\frac{\mathrm{d}(\chi^3)}{\chi_\mathrm{s}^3}\,W(\chi)\;. \tag{B.17}$$

The last steps of the calculation consist in (i) substituting the above in eq. (B.10) and (ii) computing the inverse Fourier transform to get $p_N(S)$. Step (i) yields

$$\tilde{p}_N(Q) = \mathrm{e}^{-f\tau Q}, \tag{B.18}$$

with the optical depth $\tau = N\,\langle\theta_\mathrm{E}^2\rangle\,/\Theta^2$ corrected by the factor

$$f \equiv \frac{\int_0^{\chi_\mathrm{s}}\frac{\mathrm{d}(\chi^3)}{\chi_\mathrm{s}^3}\,W(\chi)}{\int_0^{\chi_\mathrm{s}}\frac{\mathrm{d}(\chi^3)}{\chi_\mathrm{s}^3}\,\frac{\chi_\mathrm{s}-\chi}{a(\chi)\chi\chi_\mathrm{s}}} \tag{B.19}$$

$$= \frac{\int_0^{\chi_\mathrm{d}}\frac{\mathrm{d}\chi}{a(\chi)}\,\frac{\chi(\chi_\mathrm{s}-\chi)}{(1-\kappa_\mathrm{os})\chi_\mathrm{s}} - \frac{\chi(\chi_\mathrm{d}-\chi)}{(1-\kappa_\mathrm{od})\chi_\mathrm{d}} + \int_{\chi_\mathrm{d}}^{\chi_\mathrm{s}}\frac{\mathrm{d}\chi}{a(\chi)}\,\frac{\chi(\chi_\mathrm{s}-\chi)}{(1-\kappa_\mathrm{os})\chi_\mathrm{s}} - \frac{(\chi-\chi_\mathrm{d})(\chi_\mathrm{s}-\chi)}{(1-\kappa_\mathrm{ds})(\chi_\mathrm{s}-\chi_\mathrm{d})}}{\int_0^{\chi_\mathrm{s}}\frac{\mathrm{d}\chi}{a(\chi)}\,\frac{\chi(\chi_\mathrm{s}-\chi)}{\chi_\mathrm{s}}}. \tag{B.20}$$

Note that, in the large-$N$ limit, $\tilde{p}_N(Q)$ is independent on $N$. The last step (ii) is performed by substituting eq. (B.18) into eq. (B.9), which finally yields

$$\mathcal{P}_N(S) = \int_0^\infty \mathrm{d}Q\;QS\,J_0(QS)\mathrm{e}^{-f\tau Q} = \frac{f\tau S}{\left[(f\tau)^2+S^2\right]^{3/2}}\;. \tag{B.21}$$

# BIBLIOGRAPHY


[1] Christiaan Huygens. *Traité de la lumière: Où Sont Expliquées les Causes de ce qui Luy Arrive Dans la Reflexion & Dans la Refraction.* Leiden: Pieter van der Aa, 1690.

[2] Isaac Newton. *Opticks: A treatise of the reflections, refractions, inflexions and colours of light.* Dover Press, 1704.

[3] Thomas Young. The Bakerian Lecture: On the Theory of Light and Colours. *Philosophical Transactions of the Royal Society of London Series I*, 92:12–48, January 1802.

[4] James Clerk Maxwell. On Physical Lines of Force. *Philosophical Magazine and Journal of Science*, 1861.

[5] A. Einstein. Über einen die erzeugung und verwandlung des lichtes betreffenden heuristischen gesichtspunkt. *Annalen der Physik*, 322(6):132–148, 1905.

[6] Louis Albert de Broglie. Recherches sur la théorie des quanta.

[7] John Michell. On the Means of Discovering the Distance, Magnitude, &c. of the Fixed Stars, in Consequence of the Diminution of the Velocity of Their Light, in Case Such a Diminution Should be Found to Take Place in any of Them, and Such Other Data Should be Procured from Observations, as Would be Farther Necessary for That Purpose. *Phil. Trans. Roy. Soc. Lond.*, 74:35–57, 1784.

[8] Clifford M. Will. Henry Cavendish, Johann von Soldner, and the deflection of light. *American Journal of Physics*, 56(5):413–415, May 1988.

[9] J. Soldner. Über die Ablenkung eines Lichtstrahls von seiner geradlinigen Bewegung durch die Attraktion eines Weltkörpers, an welchem er nahe vorbeigeht. *Annalen der Physik*, 370(15):593–604, January 1921.

[10] Pierre-Simon Laplace. *Exposition du systéme du monde.* Cambridge Library Collection - Mathematics. Cambridge University Press, 2 edition, 2009.

[11] L. Peña. *La idea más feliz de mi vida. En: Albert Einstein: navegante solitario, 3a Ed.* Fondo de Cultura Económica, México, 2003.

[12] Giovanni Rodríguez, Jaime Reyes, and Erick Ortiz. El principio de equivalencia: una propuesta didáctica a partir del juguete de einstein. *Latin-American Journal of Physics Education*, 8:5, 01 2015.

[13] A. Einstein. Über das Relativitätsprinzip und die aus demselben gezogenen Folgerungen. *Jahrbuch der Radioaktivität und Elektronik*, 4:411–462, January 1908.

[14] A. Einstein. Über den Einfluß der Schwerkraft auf die Ausbreitung des Lichtes. *Annalen der Physik*, 340(10):898–908, January 1911.

[15] A. Einstein. Die Grundlage der allgemeinen Relativitätstheorie. *Annalen der Physik*, 354(7):769–822, January 1916.

[16] D. Pérez. Erwin Freundlich, el olvidado primer astrónomo de la relatividad. *Boletín radioastronómico*, 2019.

[17] Luís C. B. Crispino and Santiago Paolantonio. The first attempts to measure light deflection by the Sun. *Nature Astronomy*, 4:6–9, January 2020.

[18] Massimo Meneghetti. *A Brief History of Gravitational Lensing*, pages 3–19. Springer International Publishing, Cham, 2021.

[19] Gerard Gilmore and Gudrun Tausch-Pebody. The 1919 eclipse results that verified general relativity and their later detractors: a story re-told. *Notes and Records*, 76:155 – 180, 2020.

[20] F. W. Dyson, A. S. Eddington, and C. Davidson. A Determination of the Deflection of Light by the Sun's Gravitational Field, from Observations Made at the Total Eclipse of May 29, 1919. *Phil. Trans. Roy. Soc. Lond. A*, 220:291–333, 1920.

[21] O. Lodge. Gravitation and light. *Nature 104, 354*, 1919.

[22] O. Chwolson. Über eine mögliche Form fiktiver Doppelsterne. *Astronomische Nachrichten*, 221:329, June 1924.

[23] Albert Einstein. Lens-Like Action of a Star by the Deviation of Light in the Gravitational Field. *Science*, 84(2188):506–507, December 1936.

[24] Alexander S. Sharov and Igor D. Novikov. *Edwin Hubble, The Discoverer of the Big Bang Universe*. 1993.

[25] F. Zwicky. Nebulae as gravitational lenses. *Phys. Rev.*, 51:290, 1937.

[26] F. Zwicky. On the Masses of Nebulae and of Clusters of Nebulae. *ApJ*, 86:217, October 1937.

[27] F. Zwicky. Die Rotverschiebung von extragalaktischen Nebeln. *Helv. Phys. Acta*, 6:110–127, 1933.

[28] M. Schmidt. 3C 273 : A Star-Like Object with Large Red-Shift. *Nature*, 197(4872):1040, March 1963.

[29] Hong-Yee Chiu. Gravitational Collapse. *Physics Today*, 17(5):21, January 1964.

[30] Yu. G. Klimov. The Deflection of Light Rays in the Gravitational Fields of Galaxies. *Soviet Physics Doklady*, 8:119, August 1963.

[31] Sidney Liebes. Gravitational Lenses. *Phys. Rev.*, 133:B835–B844, 1964.

[32] S. Refsdal. The gravitational lens effect. *MNRAS*, 128:295, January 1964.

[33] Ya. B. Zel'dovich and I. D. Novikov. The Hypothesis of Cores Retarded during Expansion and the Hot Cosmological Model. *Soviet Astronomy*, 10:602, February 1967.

[34] Stephen Hawking. Gravitationally Collapsed Objects of Very Low Mass. *Monthly Notices of the Royal Astronomical Society*, 152(1):75–78, 04 1971.

[35] Bernard Carr, Florian Kuhnel, and Marit Sandstad. Primordial Black Holes as Dark Matter. *Phys. Rev. D*, 94(8):083504, 2016.

[36] P. J. E. Peebles. *Cosmology's Century: An Inside History of Our Modern Understanding of the Universe*. Princeton University Press, 2020.

[37] William H. Press and James E. Gunn. Method for Detecting a Cosmological Density of Condensed Objects. *ApJ*, 185:397–412, October 1973.

[38] D. Walsh, R. F. Carswell, and R. J. Weymann. 0957+561 A, B: twin quasistellar objects or gravitational lens? *Nature*, 279:381–384, May 1979.

[39] P. Young, J. E. Gunn, J. Kristian, J. B. Oke, and J. A. Westphal. The double quasar Q0957+561 A, B: a gravitational lens image formed by a galaxy at z=0.39. *ApJ*, 241:507–520, October 1980.

[40] K. Chang and S. Refsdal. Flux variations of QSO 0957 + 561 A, B and image splitting by stars near the light path. *Nature*, 282(5739):561–564, December 1979.

[41] P. Young. Q0957+561 : effects of random stars on the gravitational lens. *ApJ*, 244:756–767, March 1981.

[42] III Gott, J. R. Are heavy halos made of low mass stars - A gravitational lens test. *ApJ*, 243:140–146, January 1981.

[43] B. Paczynski. Gravitational Microlensing at Large Optical Depth. *ApJ*, 301:503, February 1986.

[44] R. Kayser, S. Refsdal, and R. Stabell. Astrophysical applications of gravitational micro-lensing. *A&A*, 166:36–52, September 1986.

[45] M. J. Irwin, R. L. Webster, P. C. Hewett, R. T. Corrigan, and R. I. Jedrzejewski. Photometric Variations in the Q2237+0305 System: First Detection of a Microlensing Event. *AJ*, 98:1989, December 1989.

[46] M. R. S. Hawkins. Gravitational microlensing, quasar variability and missing matter. *Nature*, 366(6452):242–245, November 1993.

[47] M. R. S. Hawkins. The signature of dark matter in quasar light curves, 1998.

[48] M. R. S. Hawkins and P. Véron. The quasar luminosity function from a variability-selected sample. *Monthly Notices of the Royal Astronomical Society*, 260(1):202–208, 01 1993.

[49] P. Schneider. Upper bounds on the cosmological density of compact objects with sub-solar masses from the variability of QSOs. *A&A*, 279:1–20, November 1993.

[50] C. Alcock et al. The MACHO project first year LMC results: The Microlensing rate and the nature of the galactic dark halo. *Astrophys. J.*, 461:84, 1996.

[51] EROS Collaboration. Limits on galactic dark matter with 5 years of eros smc data. 2002.

[52] L. Wyrzykowski, J. Skowron, S. Kozłowski, A. Udalski, M. K. Szymański, M. Kubiak, G. Pietrzyński, I. Soszyński, O. Szewczyk, K. Ulaczyk, R. Poleski, and P. Tisserand. The OGLE view of microlensing towards the Magellanic Clouds – IV. OGLE-III SMC data and final conclusions on MACHOs*. *Monthly Notices of the Royal Astronomical Society*, 416(4):2949–2961, 09 2011.

[53] M. R. S. Hawkins. A new look at microlensing limits on dark matter in the Galactic halo. *A&A*, 575:A107, March 2015.

[54] Josh Calcino, Juan García-Bellido, and Tamara M. Davis. Updating the MACHO fraction of the Milky Way dark halowith improved mass models. *MNRAS*, 479(3):2889–2905, September 2018.

[55] Gabriela Sato-Polito, Ely D. Kovetz, and Marc Kamionkowski. Constraints on the primordial curvature power spectrum from primordial black holes. *Phys. Rev. D*, 100(6):063521, September 2019.

[56] E. Mediavilla, J. A. Munoz, E. Falco, V. Motta, E. Guerras, H. Canovas, C. Jean, A. Oscoz, and A. M. Mosquera. Microlensing-Based Estimate of the Mass Fraction in Compact Objects in Lens. *Astrophys. J.*, 706:1451–1462, 2009.

[57] R. L. Webster, A. M. N. Ferguson, R. T. Corrigan, and M. J. Irwin. Interpreting the Light Curve of Q2237+0305. *AJ*, 102:1939, December 1991.

[58] G. F. Lewis and M. J. Irwin. The statistics of microlensing light curves — II. Temporal analysis. *Monthly Notices of the Royal Astronomical Society*, 283(1):225–240, 10 1996.

[59] Hans J. Witt, Shude Mao, and Paul L. Schechter. On the Universality of Microlensing in Quadruple Gravitational Lenses. *ApJ*, 443:18, April 1995.

[60] Paul L. Schechter and Joachim Wambsganss. Quasar Microlensing at High Magnification and the Role of Dark Matter: Enhanced Fluctuations and Suppressed Saddle Points. *ApJ*, 580(2):685–695, December 2002.

[61] R. Benton Metcalf and Adam Amara. Small-scale structures of dark matter and flux anomalies in quasar gravitational lenses. *Monthly Notices of the Royal Astronomical Society*, 419(4):3414–3425, 01 2012.

[62] S. H. Suyu et al. HOLISMOKES – I. Highly Optimised Lensing Investigations of Supernovae, Microlensing Objects, and Kinematics of Ellipticals and Spirals. *Astron. Astrophys.*, 644:A162, 2020.

[63] Eric V. Linder, P. Schneider, and Robert V. Wagoner. Gravitational Lensing Statistics of Amplified Supernovae. *ApJ*, 324:786, January 1988.

[64] Kevin P. Rauch. Gravitational Microlensing of High-Redshift Supernovae by Compact Objects. *ApJ*, 374:83, June 1991.

[65] R. Benton Metcalf and Joseph Silk. A Fundamental Test of the Nature of Dark Matter. *ApJL*, 519(1):L1–L4, July 1999.

[66] Uros Seljak and Daniel E. Holz. Limits on the density of compact objects from high redshift supernovae. *Astron. Astrophys.*, 351:L10, 1999.

[67] Lars Bergstrom, Martin Goliath, Ariel Goobar, and Edvard Mortsell. Lensing effects in an inhomogeneous universe. *Astron. Astrophys.*, 358:13, 2000.

[68] R. Benton Metcalf and Joseph Silk. New Constraints on Macroscopic Compact Objects as Dark Matter Candidates from Gravitational Lensing of Type Ia Supernovae. *Phys. Rev. Lett.*, 98(7):071302, February 2007.

[69] Miguel Zumalacárregui and Uros Seljak. Limits on stellar-mass compact objects as dark matter from gravitational lensing of type Ia supernovae. *Phys. Rev. Lett.*, 121(14):141101, 2018.

[70] Jakob Jonsson, Tomas Dahlen, Ariel Goobar, Christofer Gunnarsson, Edvard Mortsell, and Kyoungsoo Lee. Lensing magnification of supernovae in the GOODS-fields. *Astrophys. J.*, 639:991–998, 2006.

[71] Suhail Dhawan, Ariel Goobar, and Edvard Mörtsell. The effect of inhomogeneities on dark energy constraints. *JCAP*, 07:024, 2018.

[72] Kelly et al. Extreme magnification of a star at redshift 1.5 by a galaxy-cluster lens, 2017.

[73] Welch et al. A highly magnified star at redshift 6.2. *Nature*, 603:815–818, 03 2022.

[74] B. P. Abbott et al. Observation of Gravitational Waves from a Binary Black Hole Merger. *Phys. Rev. Lett.*, 116(6):061102, 2016.

[75] J. A. Peacock. Gravitational lenses and cosmological evolution. *Monthly Notices of the Royal Astronomical Society*, 199(4):987–1006, 08 1982.

[76] E. L. Turner, J. P. Ostriker, and III Gott, J. R. The statistics of gravitational lenses : the distributions of image angular separations and lens redshifts. *ApJ*, 284:1–22, September 1984.

[77] C. C. Dyer. Image separation statistics for multiply imaged quasars. *ApJ*, 287:26–32, December 1984.

[78] P. Schneider and A. Weiss. A gravitational lens origin for AGN-variability ? Consequences of micro- lensing. *A&A*, 171:49–65, January 1987.

[79] Carolin Seitz and Peter Schneider. Variability of microlensing light curves I. Autocorrelation method and the calculation of the correlated deflection probability. *A&A*, 288:1–18, August 1994.

[80] R. Nityananda and J. P. Ostriker. Gravitational lensing by stars in a galaxy halo - Theory of combined weak and strong scattering. *Journal of Astrophysics and Astronomy*, 5:235–250, September 1984.

[81] Roger Blandford and Ramesh Narayan. Fermat's Principle, Caustics, and the Classification of Gravitational Lens Images. *ApJ*, 310:568, November 1986.

[82] Man Hoi Lee and David N. Spergel. An Analytical Approach to Gravitational Lensing by an Ensemble of Axisymmetric Lenses. *ApJ*, 357:23, July 1990.

[83] Shude Mao. Gravitational Microlensing by a Single Star plus External Shear. *ApJ*, 389:63, April 1992.

[84] Lev Kofman, Nick Kaiser, Man Hoi Lee, and Arif Babul. Statistics of Gravitational Microlensing Magnification. I. Two-dimensional Lens Distribution. *ApJ*, 489(2):508–521, November 1997.

[85] Man Hoi Lee, Arif Babul, Lev Kofman, and Nick Kaiser. Statistics of Gravitational Microlensing Magnification. II. Three-dimensional Lens Distribution. *ApJ*, 489(2):522–542, November 1997.

[86] Joachim Wambsganss. Probability Distributions for the Magnification of Quasars due to Microlensing. *ApJ*, 386:19, February 1992.

[87] Geraint F. Lewis and Mike J. Irwin. The statistics of microlensing light curves - I. Amplification probability distributions. *MNRAS*, 276(1):103–114, September 1995.

[88] Peter Schneider, Jürgen Ehlers, and Emilio E. Falco. *Gravitational Lenses*. Springer Berlin, Heidelberg, 1992.

[89] Pierre Fleury and Juan García-Bellido. On simple analytic models of microlensing amplification statistics. *Phys. Dark Univ.*, 29:100567, 2020.

[90] J. A. Peacock. Flux conservation and random gravitational lensing. *MNRAS*, 223:113–128, November 1986.

[91] Steven Weinberg. Apparent Luminosities in a Locally Inhomogeneous Universe. 5 1976.

[92] T. W. B. Kibble and R. Lieu. Average Magnification Effect of Clumping of Matter. *ApJ*, 632:718–726, October 2005.

[93] O. Wucknitz. From planes to spheres: about gravitational lens magnifications. *MNRAS*, 386(1):230–244, May 2008.

[94] Michel-Andrès Breton and Pierre Fleury. Theoretical and numerical perspectives on cosmic distance averages. *A&A*, 655:A54, November 2021.

[95] Ya. B. Zel'dovich. Observations in a Universe Homogeneous in the Mean. *Sov. Astron. Lett.*, 8:13, August 1964.

[96] Michel-Andrès Breton, Yann Rasera, Atsushi Taruya, Osmin Lacombe, and Shohei Saga. Imprints of relativistic effects on the asymmetry of the halo cross-correlation function: from linear to non-linear scales. *Mon. Not. Roy. Astron. Soc.*, 483(2):2671–2696, 2019.

[97] A. Conley, J. Guy, M. Sullivan, N. Regnault, P. Astier, C. Balland, S. Basa, R. G. Carlberg, D. Fouchez, D. Hardin, I. M. Hook, D. A. Howell, R. Pain, N. Palanque-Delabrouille, K. M. Perrett, C. J. Pritchet, J. Rich, V. Ruhlmann-Kleider, D. Balam, S. Baumont, R. S. Ellis, S. Fabbro, H. K. Fakhouri, N. Fourmanoit, S. González-Gaitán, M. L. Graham, M. J. Hudson, E. Hsiao, T. Kronborg, C. Lidman, A. M. Mourao, J. D. Neill, S. Perlmutter, P. Ripoche, N. Suzuki, and E. S. Walker. Supernova Constraints and Systematic Uncertainties from the First Three Years of the Supernova Legacy Survey. *ApJS*, 192(1):1, January 2011.

[98] Pierre Fleury, Julien Larena, and Jean-Philippe Uzan. Gravitational lenses in arbitrary space-times. *Class. Quant. Grav.*, 38(8):085002, 2021.

[99] Israel Kovner. The Thick Gravitational Lens: A Lens Composed of Many Elements at Different Distances. *ApJ*, 316:52, May 1987.

[100] Stella Seitz and Peter Schneider. Some remarks on multiple deflection gravitational lensing. *A&A*, 287:349–360, July 1994.

[101] Rennan Bar-Kana. Effect of Large-Scale Structure on Multiply Imaged Sources. *ApJ*, 468:17, September 1996.

[102] Peter Schneider. The Cosmological lens equation and the equivalent single plane gravitational lens. *Mon. Not. Roy. Astron. Soc.*, 292:673, 1997.

[103] Curtis McCully, Charles R. Keeton, Kenneth C. Wong, and Ann I. Zabludoff. A New Hybrid Framework to Efficiently Model Lines of Sight to Gravitational Lenses. *Mon. Not. Roy. Astron. Soc.*, 443(4):3631–3642, 2014.

[104] Simon Birrer, Cyril Welschen, Adam Amara, and Alexandre Refregier. Line-of-sight effects in strong lensing: Putting theory into practice. *JCAP*, 1704(04):049, 2017.

[105] Pierre Fleury, Julien Larena, and Jean-Philippe Uzan. Line-of-sight effects in strong gravitational lensing. *JCAP*, 08:024, 2021.

[106] Matthias Bartelmann and Peter Schneider. Weak gravitational lensing. *Phys. Rept.*, 340:291–472, 2001.

[107] Pierre Fleury. *Light propagation in inhomogeneous and anisotropic cosmologies*. PhD thesis, Paris U., VI, IAP, 2015.

[108] Pierre Fleury, Julien Larena, and Jean-Philippe Uzan. Cosmic convergence and shear with extended sources. *Phys. Rev. D*, 99(2):023525, 2019.

[109] Lev Kofman, Nick Kaiser, Man Hoi Lee, and Arif Babul. Statistics of gravitational microlensing magnification. I. two-dimensional lens distribution. *Astrophys. J.*, 485:508–521, 1997.

[110] S. Chandrasekhar. Stochastic Problems in Physics and Astronomy. *Reviews of Modern Physics*, 15(1):1–89, January 1943.

[111] P. Schneider. Apparent number density enhancement of quasars near foreground galaxies due to gravitational lensing. I - Amplification cross sections. II - The amplification probability density distribution and results. *A&A*, 179(1-2):71–92, June 1987.

[112] C. R. Keeton, C. S. Kochanek, and U. Seljak. Shear and Ellipticity in Gravitational Lenses. *ApJ*, 482(2):604–620, June 1997.

[113] Kimmo Kainulainen and Valerio Marra. Accurate Modeling of Weak Lensing with the sGL Method. *Phys. Rev.*, D83:023009, 2011.

[114] Kimmo Kainulainen and Valerio Marra. A new stochastic approach to cumulative weak lensing. *Phys. Rev.*, D80:123020, 2009.

[115] K. P. Rauch. Gravitational Microlensing of High-Redshift Supernovae by Compact Objects: Erratum. *ApJ*, 383:466, December 1991.

[116] Hans J. Witt and Shude Mao. Can Lensed Stars Be Regarded as Pointlike for Microlensing by MACHOs? *ApJ*, 430:505, August 1994.

[117] A. Esteban-Gutiérrez, E. Mediavilla, J. Jiménez-Vicente, N. Agües-Paszkowsky, J. A. Muñoz, and S. Heydenreich. Limiting the Abundance of LIGO/Virgo Black Holes with Microlensing Observations of Quasars of Finite Size. *Astrophys. J. Lett.*, 929(1):L17, 2022.

[118] M. R. S. Hawkins. New evidence for a cosmological distribution of stellar mass primordial black holes. *Mon. Not. Roy. Astron. Soc.*, 512:5706–5714, 2022.

[119] Juan García-Bellido, Sébastien Clesse, and Pierre Fleury. Primordial black holes survive SN lensing constraints. *Phys. Dark Univ.*, 20:95–100, 2018.

[120] Jorge Cervantes-Cota, Salvador Galindo-Uribarri, and George Smoot. A Brief History of Gravitational Waves. *Universe*, 2(3):22, September 2016.

[121] James Clerk Maxwell. A Dynamical Theory of the Electromagnetic Field. *Philosophical Transactions of the Royal Society of London Series I*, 155:459–512, January 1865.

[122] Oliver Heaviside. A gravitational and electromagnetic analogy. *Electromagnetic Theory*, vol.1:455–466 Appendix B, 1893.

[123] Henri Poincaré. Sur la dynamique de l'électron. *Rendiconti del Circolo matematico di Palermo*, 21:129–176, January 1906.

[124] Hermann Weyl. *Space - Time - Matter*. 1922.

[125] A. Einstein and N. Rosen. On Gravitational Waves. *Journal of The Franklin Institute*, 223:43–54, January 1937.

[126] F. A. E. Pirani. On the physical significance of the Riemann tensor. *Acta Physica Polonica*, 15:389–405, January 1956.

[127] P. Bergmann. *The riddle of gravitation.* 1969.

[128] Giles Hammond, Stefan Hild, and Matthew Pitkin. Advanced technologies for future laser-interferometric gravitational wave detectors. *Journal of Modern Optics*, 61, 02 2014.

[129] J. Weber. Observation of the Thermal Fluctuations of a Gravitational-Wave Detector. 17(24):1228–1230, December 1966.

[130] A K Chaudhuri. Gravitational Wave for a pedestrian. *arXiv e-prints*, page arXiv:1605.00761, May 2016.

[131] Imène Belahcene. *Searching for gravitational waves produced by cosmic strings in LIGO-Virgo data*. PhD thesis, 10 2019.

[132] J. Weber. Anisotropy and Polarization in the Gravitational-Radiation Experiments. 25(3):180–184, July 1970.

[133] J. M. Weisberg and J. H. Taylor. The Relativistic Binary Pulsar B1913+16: Thirty Years of Observations and Analysis. In Fred A. Rasio and Ingrid H. Stairs, editors, *Binary Radio Pulsars*, volume 328 of *Astronomical Society of the Pacific Conference Series*, page 25, July 2005.

[134] J. H. Taylor, L. A. Fowler, and P. M. McCulloch. Measurements of general relativistic effects in the binary pulsar PSR1913 + 16. *Nature*, 277(5696):437–440, February 1979.

[135] M. E. Gertsenshteĭn and V. I. Pustovoĭt. On the Detection of Low-Frequency Gravitational Waves. *Soviet Journal of Experimental and Theoretical Physics*, 16:433, January 1963.

[136] *Topics in Theoretical and Experimental Gravitation Physics*, volume 27 of *NATO Advanced Study Institute (ASI) Series B*, January 1977.

[137] *Progress with the Garching (West Germany) 30 meter prototype for a gravitational wave detector*, August 1985.

[138] J. Hough, B. J. Meers, G. P. Newton, N. A. Robertson, H. Ward, Bernard F. Schutz, and R. W. P. Drever. A BRITISH LONG BASELINE GRAVITATIONAL WAVE OBSERVATORY. DESIGN STUDY REPORT. 5 1986.

[139] K. Maischberger, A. Rudiger, R. Schilling, L. Schnupp, D. Shoemaker, and W. Winkler. PROPOSAL FOR THE CONSTRUCTION OF A LARGE LASER INTERFEROMETER FOR THE MEASUREMENT OF GRAVITATIONAL RADIATION. (IN GERMAN). 1985.

[140] Ch. J. Bordé. Méthodes optiques de détection des ondes gravitationnelles - Préface. *Annales de Physique*, 10(3):R1–R2, January 1985.

[141] Rainer Weiss. Republication of: Electromagnetically coupled broadband gravitational antenna. *Gen. Rel. Grav.*, 54(11):153, 2022.

[142] B. P. Abbott et al. GW170817: Observation of Gravitational Waves from a Binary Neutron Star Inspiral. *Phys. Rev. Lett.*, 119(16):161101, 2017.

[143] B. P. Abbott et al. GWTC-1: A Gravitational-Wave Transient Catalog of Compact Binary Mergers Observed by LIGO and Virgo during the First and Second Observing Runs. *Phys. Rev. X*, 9(3):031040, 2019.

[144] B. P. Abbott et al. GW190425: Observation of a Compact Binary Coalescence with Total Mass $\sim 3.4 M_{\odot}$. *Astrophys. J. Lett.*, 892(1):L3, 2020.

[145] R. Abbott et al. GW190412: Observation of a Binary-Black-Hole Coalescence with Asymmetric Masses. *Phys. Rev. D*, 102(4):043015, 2020.

[146] R. Abbott et al. GW190814: Gravitational Waves from the Coalescence of a 23 Solar Mass Black Hole with a 2.6 Solar Mass Compact Object. *Astrophys. J. Lett.*, 896(2):L44, 2020.

[147] T. Akutsu et al. KAGRA: 2.5 Generation Interferometric Gravitational Wave Detector. *Nature Astron.*, 3(1):35–40, 2019.

[148] B. P. Abbott et al. Prospects for observing and localizing gravitational-wave transients with Advanced LIGO, Advanced Virgo and KAGRA. *Living Rev. Rel.*, 21(1):3, 2018.

[149] J. K. Lawrence. Focusing of gravitational radiation by interior gravitational fields. *Nuovo Cimento B Serie*, 6B:225–235, January 1971.

[150] Hans C. Ohanian. On the Focusing of Gravitational Radiation. *International Journal of Theoretical Physics*, 9(6):425–437, June 1974.

[151] S. Deguchi and W. D. Watson. Diffraction in Gravitational Lensing for Compact Objects of Low Mass. *ApJ*, 307:30, August 1986.

[152] Norihito Matsunaga and Kazuhiro Yamamoto. The finite source size effect and wave optics in gravitational lensing. *JCAP*, 2006(1):023, January 2006.

[153] Yasusada Nambu. Wave Optics and Image Formation in Gravitational Lensing. *International Journal of Astronomy and Astrophysics*, 3(1):1–7, January 2013.

[154] R. J. Bontz and M. P. Haugan. A Diffraction Limit on the Gravitational Lens Effect. , 78(1):199–210, August 1981.

[155] Takahiro T. Nakamura. Gravitational lensing of gravitational waves from inspiraling binaries by a point mass lens. *Phys. Rev. Lett.*, 80:1138–1141, Feb 1998.

[156] Pierre Christian, Salvatore Vitale, and Abraham Loeb. Detecting stellar lensing of gravitational waves with ground-based observatories. *Phys. Rev. D*, 98:103022, Nov 2018.

[157] Giovanni Tambalo, Miguel Zumalacárregui, Liang Dai, and Mark Ho-Yeuk Cheung. Lensing of gravitational waves: efficient wave-optics methods and validation with symmetric lenses. 10 2022.

[158] Tom Broadhurst, Jose M. Diego, and III Smoot, George F. Twin LIGO/Virgo Detections of a Viable Gravitationally-Lensed Black Hole Merger. *arXiv e-prints*, page arXiv:1901.03190, January 2019.

[159] Connor McIsaac, David Keitel, Thomas Collett, Ian Harry, Simone Mozzon, Oliver Edy, and David Bacon. Search for strongly lensed counterpart images of binary black hole mergers in the first two LIGO observing runs. *Phys. Rev. D*, 102(8):084031, 2020.

[160] Alvin K. Y. Li, Rico K. L. Lo, Surabhi Sachdev, C. L. Chan, E. T. Lin, Tjonnie G. F. Li, and Alan J. Weinstein. Finding diamonds in the rough: Targeted Sub-threshold Search for Strongly-lensed Gravitational-wave Events. 4 2019.

[161] Mark H. Y. Cheung, Joseph Gais, Otto A. Hannuksela, and Tjonnie G. F. Li. Stellar-mass microlensing of gravitational waves. *MNRAS*, 503(3):3326–3336, May 2021.

[162] J. M. Diego, O. A. Hannuksela, P. L. Kelly, T. Broadhurst, K. Kim, T. G. F. Li, G. F. Smoot, and G. Pagano. Observational signatures of microlensing in gravitational waves at LIGO/Virgo frequencies. *Astron. Astrophys.*, 627:A130, 2019.

[163] Anuj Mishra, Ashish Kumar Meena, Anupreeta More, Sukanta Bose, and Jasjeet Singh Bagla. Gravitational lensing of gravitational waves: effect of microlens population in lensing galaxies. *MNRAS*, 508(4):4869–4886, December 2021.

[164] Eungwang Seo, Otto A. Hannuksela, and Tjonnie G. F. Li. Strong lensing: A magnifying glass to detect gravitational-wave microlensing. In *17th International Conference on Topics in Astroparticle and Underground Physics*, 10 2021.

[165] Anna Liu, Isaac C. F. Wong, Samson H. W. Leong, Anupreeta More, Otto A. Hannuksela, and Tjonnie G. F. Li. Exploring the hidden Universe: A novel phenomenological approach for recovering arbitrary gravitational-wave millilensing configurations. 2 2023.

[166] Jose M. Diego. Constraining the abundance of primordial black holes with gravitational lensing of gravitational waves at LIGO frequencies. *Phys. Rev. D*, 101(12):123512, 2020.

[167] Jie-Shuang Wang, Antonio Herrera-Martín, and Yi-Ming Hu. Lensing by primordial black holes: constraints from gravitational wave observations. 8 2021.

[168] Juan Urrutia and Ville Vaskonen. Lensing of gravitational waves as a probe of compact dark matter. *Mon. Not. Roy. Astron. Soc.*, 509(1):1358–1365, 2021.

[169] S. Basak, A. Ganguly, K. Haris, S. Kapadia, A. K. Mehta, and P. Ajith. Constraints on Compact Dark Matter from Gravitational Wave Microlensing. *Astrophys. J.*, 926(2):L28, 2022.

[170] N. Straumann. *General Relativity and Relativistic Astrophysics*. 1984.

[171] Charles Dalang, Pierre Fleury, and Lucas Lombriser. Horndeski gravity and standard sirens. *Phys. Rev. D*, 102(4):044036, 2020.

[172] Irwin I. Shapiro. Fourth Test of General Relativity. *Phys. Rev. Lett.*, 13:789–791, 1964.

[173] Ryuichi Takahashi and Takashi Nakamura. Wave effects in gravitational lensing of gravitational waves from chirping binaries. *Astrophys. J.*, 595:1039–1051, 2003.

[174] Jose María Ezquiaga, Wayne Hu, and Macarena Lagos. Apparent Superluminality of Lensed Gravitational Waves. *Phys. Rev. D*, 102(2):023531, 2020.

[175] Mick Wright and Martin Hendry. Gravelamps: Gravitational Wave Lensing Mass Profile Model Selection. *ApJ*, 935(2):68, August 2022.

[176] Milton Abramowitz and Irene A. Stegun, editors. *Handbook of Mathematical Functions with Formulas, Graphs, and Mathematical Tables*. U.S. Government Printing Office, Washington, DC, USA, tenth printing edition, 1972.

[177] Liang Dai, Barak Zackay, Tejaswi Venumadhav, Javier Roulet, and Matias Zaldarriaga. Search for Lensed Gravitational Waves Including Morse Phase Information: An Intriguing Candidate in O2. *arXiv e-prints*, page arXiv:2007.12709, July 2020.

[178] Thomas Callister, Maya Fishbach, Daniel Holz, and Will Farr. Shouts and Murmurs: Combining Individual Gravitational-Wave Sources with the Stochastic Background to Measure the History of Binary Black Hole Mergers. *Astrophys. J. Lett.*, 896(2):L32, 2020.

[179] The LIGO Scientific collaboration. Gravitational wave astronomy with LIGO and similar detectors in the next decade. *arXiv e-prints*, page arXiv:1904.03187, April 2019.

[180] Hsin-Yu Chen, Daniel E. Holz, John Miller, Matthew Evans, Salvatore Vitale, and Jolien Creighton. Distance measures in gravitational-wave astrophysics and cosmology. *Class. Quant. Grav.*, 38(5):055010, 2021.

[181] Sascha Husa, Sebastian Khan, Mark Hannam, Michael Pürrer, Frank Ohme, Xisco Jiménez Forteza, and Alejandro Bohé. Frequency-domain gravitational waves from nonprecessing black-hole binaries. I. New numerical waveforms and anatomy of the signal. *Phys. Rev. D*, 93(4):044006, 2016.

[182] R. Teyssier. Cosmological hydrodynamics with adaptive mesh refinement. A new high resolution code called RAMSES. *AAP*, 385:337–364, April 2002.

[183] T. Guillet and R. Teyssier. A simple multigrid scheme for solving the Poisson equation with arbitrary domain boundaries. *Journal of Computational Physics*, 230:4756–4771, June 2011.

[184] E. Komatsu, K. M. Smith, J. Dunkley, C. L. Bennett, B. Gold, G. Hinshaw, N. Jarosik, D. Larson, M. R. Nolta, L. Page, D. N. Spergel, M. Halpern, R. S. Hill, A. Kogut, M. Limon, S. S. Meyer, N. Odegard, G. S. Tucker, J. L. Weiland, E. Wollack, and E. L. Wright. Seven-year Wilkinson Microwave Anisotropy Probe (WMAP) Observations: Cosmological Interpretation. *ApJs*, 192:18, February 2011.

[185] Vincent Reverdy. *Propagation de la lumière dans un Univers structuré et nouvelles approches numériques en cosmologie*. PhD thesis, Laboratoire Univers et Théories, 2014. `https://github.com/vreverdy/magrathea-pathfinder/blob/master/vreverdy_phd_manuscript.pdf`.

[186] Michel-Andrès Breton. *Constructing observables in cosmology : towards new probes of the dark sector*. PhD thesis, Laboratoire Univers et Théories, 2018.

[187] N. Aghanim et al. Planck 2018 results. VI. Cosmological parameters. *Astron. Astrophys.*, 641:A6, 2020. [Erratum: Astron.Astrophys. 652, C4 (2021)].